# Confined dynamics, side-chain crystallization and long term behavior of nanophase separated poly(3-alkyl thiophenes)

**Dissertation**

zur Erlangung des akademischen Grades

*Doktor der Naturwissenschaften (Dr. rer. nat.)*

vorgelegt am:

Institut für Physik

der Naturwissenschaftlichen Fakultät II - Chemie, Physik und Mathematik

der Martin-Luther-Universität Halle-Wittenberg

von

**Shireesh Pankaj**

geboren am 20. Januar 1982 in Jaipur (Indien)

Halle (Saale), Januar 2011

Gutachter:

1. _____ PD Dr. Mario Beiner _____

2. _____ Prof. Dr. Roland Weidisch _____

3. _____ Prof. Dr. Andreas Schönhals _____

Öffentliche Verteidigung:   26. Mai 2011

*Dedicated to my wife Neha*
*and*
*my parents for their endless love, support and sacrifice.*

# Contents

# Chapter 1

# Introduction

Glasses are ubiquitous materials which are disordered solids frozen in the amorphous state with no molecular long-range order like liquids but mechanically behaving like solids. [1] Glasses have numerous applications ranging from classical window applications to engineering plastics, optoelectronics, food preservation and packaging, pharmaceuticals stabilization etc. Nature also harness the glass formation processes in biomolecules like proteins. Glass formation occurs in polymers as well as in organic molecules, inorganic molecules, salts, colloidal suspensions, metal alloys etc. Usually glasses are formed, if crystallization is prevented, by cooling the viscous materials rapidly to reach to a viscosity of approximately $10^{13}$ Poise. The temperature where this viscosity is reached and the glass forming liquid freezes in is called glass temperature $T_g$. The rates required depends upon the complexity of molecules. Glass formation in case of small molecules which can crystallize easily requires very high quenching rates, while polymers form glasses already at moderate cooling rates due to the complexity of their molecular architecture. Other methods for glass formation do exist such as vapor deposition, in-situ liquid polymerization reaction, solvent evaporation, solid state diffusion, sol-gel process, electrochemical deposition etc. [2, 3] Many phenomenological models exists in the literature describing this thermal glass transition at $T_g$ as well as the slow dynamics in the viscous glass-forming material before freezing in called $\alpha$ relaxation or dynamic glass transition. Examples are free-volume approach [4,5], thermodynamic models [6], Adam and Gibbs approach [7], mode coupling theory [8], coupling model [9] etc. Unfortunately, none of these models describes fully the phenomenology and molecular background of the glass transition phenomenon. In this context, Anderson [10] in 1995 quoted that "The deepest and most interesting unsolved problem in solid state theory is probably the theory of the nature of glass and the glass transition". The situation has not been changed seriously since that time.

A recent topic which is of interest for many researchers in the light of increasing applications of nanomaterials [11, 12] is the softening behavior of the glasses under confinement. [13] Typical peculiarities of the glass transition under confinement are shifts in the glass temperature as well as broadening or smearing out of the glass transition interval. Such peculiarities in the softening behavior of host-guest systems [14–17] such as o-terphenyl in nanoporous host systems or self-assembled polymers [18, 19] are either explained by the changes in the packing density within the confinement, interfacial effects or finite size effects (dimensions of the confinement) [20]. Thin films which are understood to be a 1-D confinement are also discussed in this light considering free standing polymer films or supported by substrates. [21–23] No serious consensus is derived yet regarding the reasons for the observed changes in softening behavior and $\alpha$ dynamics under confinement as it is usually hard to get the densities of the confined systems which might be slightly different from that of bulk-like materials.

Self assembled polymers are an important class of materials where softening processes under confinement are expected. In classical block copolymers with domain sizes >100Å [24], confinement effects on the dynamics are less relevant while pronounced effects seem to appear in nanostructured side chain polymers where main and side chain entities demix on length scales less than 50Å. [18, 25] Comb-like polymers containing long alkyl groups are widely used and have been also proposed as building blocks of self-assembled model systems with well defined structures on the nanoscale having fascinating properties. [26, 27] The aggregation of alkyl groups to small alkyl nanodomains with typical dimensions in the range of 10-30Å seems to be a general phenomenon appearing in various polymers containing long methylene sequences. [25, 28–33] Aggregation occurs not only in case of crystalline methylene sequences but interestingly also for alkyl groups in the amorphous state. This has been shown in particular for comb-like polymers with not too long alkyl groups where side chain crystallization is normally depressed due to frustration effects introduced by the main chains. A separation of main and side chain parts occurs commonly in polymer series with $C = 4 - 12$ alkyl carbons per side chain attached to main chains with variable microstructure and softening behavior. [18] This phenomenon has been called nanophase separation [25, 32] and the dynamics in the alkyl nanodomains is shown to vary strongly with the size of confinement. [18, 25]

A prominent example for functional side chain polymers are alkylated polythiophenes belonging to the class of conjugated polymers which are environmentally and thermally stable. Poly(3-alkyl thiophenes) are an interesting class of materials due to their favorable elec-

tronic, optoelectronic, thermochromic and solvatochromic properties. [34–43]. They have a wide range of applications in electrical conductors, non-linear optical devices, polymer LEDs, sensors, batteries, solar cells, electrodes, nanoelectronics as well as in transistors and many more. [34] Alkyl groups are attached here in order to improve the processibility of the materials. Specialty in case of P3ATs is that the thiophene rings can either crystallize (regio-regular) or remain amorphous (regio-random) depending on the head-to-tail arrangement of their monomeric units along the main chains. Regio-regular poly(3-alkyl thiophenes) are privileged in this respect compared to their regio-random counterparts as their thiophene rings are able to pack on a crystalline lattice. This improves the planarity of the thiophene rings along the main chain and the overlap of their $\pi$ orbitals which are central requirements for efficient charge transport. [44,45] Hence regio-regular systems are used for a large number of applications over regio-random systems. There are still open questions in the discussion about the crystalline state of regio-regular P3ATs which depends on many factors like molecular weight, sample preparation and annealing procedure. In particular, the packing of the side chains in P3ATs is not finally understood. There is still no consensus to what extent the alkyl groups are amorphous or crystalline, in which way they can pack and to what extent changes in side chain packing do influence overall structure and macroscopic properties. [36, 38, 46, 47]

Crystallization of the alkyl groups in comb-like polymers often occurs for side chains containing more than $10 - 12$ alkyl carbons. [48, 49] The crystallizable $CH_2$ units are usually packed on a hexagonal lattice. [49, 50] It can be assumed that side chain crystallization starts in already existing alkyl nanodomains far away from the main chains acting normally as frustrating element. [51] Side chain crystallization is accompanied by an increase of the 'Scherrer coherence length' of the nanophase-separated structure, i.e. it leads to well ordered lamellar morphology on the mesoscale caused by stacked main and side chain layers. Transitions from hexagonal to orthorhombic packing of the $CH_2$ units within the alkyl nanodomains have been reported in the recent literature for polymers with extremely long alkyl groups in the side chain forming most likely thicker crystalline layers in the alkyl nanodomains. [52, 53] Physical aging phenomena i.e. the structural relaxation of the non-equilibrium glassy states towards the equilibrium state of the amorphous nano-structured system is also an interesting point of consideration which is not addressed in literature to the best of our knowledge.

Aim of this thesis is to study the interrelations between structure and dynamics in poly(3-alkyl thiophenes) which are important for optimizing the properties of the devices made from such materials. The scientific questions will be addressed and discussed in more detail

in chapter 3.

# Chapter 2

# Basic concepts

This chapter is dedicated to the fundamentals of *Glass transition and glassy state* and classical approaches and theories which have been developed to describe the phenomenon. Factors affecting the glass transition, in particular changes due to confinement as well as physical aging will be discussed.

## 2.1 Glass transition and dynamic heterogeneities

Considering a liquid like material, when cooled its viscosity increases tremendously connected with a slowing down of molecular motions which causes structural rearrangements. Below a certain temperature $T_g$, these molecular motions freeze-in and the material cannot reach its equilibrium state in the time scale of the experiment due to very high viscosities (of the order of $10^{13}$ poise). This non-equilibrium vitrified state of the liquid is termed *glassy state* and the temperature interval in which the deviation from the equilibrium liquid like state to non-equilibrium glassy state transition occurs is coined as *thermal glass transition*. [20, 54–58]

The thermal glass transition can be visualized using volume (from classical dilatometric measurements), or enthalpy curves (from conventional thermal analysis methods like differential scanning calorimetry) *vs* temperature as shown in Figure 2.1. At high temperature, an isotropic liquid like state or the equilibrium state exists. On cooling down the liquid at a specific rate (also sufficient to suppress the crystallization process in case of crystallizable systems) volume decreases first linearly resulting in lower mobility but deviates then clearly from the extrapolated equilibrium line due to glassification below $T_g$. For conventional rates ($\approx$ 10K/min), the characteristic time of the relaxation process at the glass transition tem-
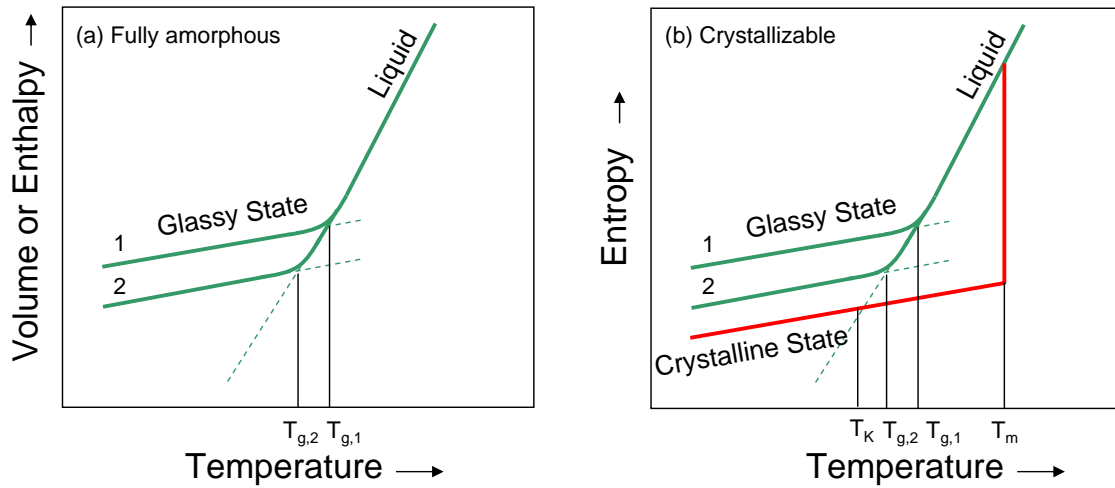
**Figure 2.1:** (a) Volume V or enthalpy H and (b) entropy S $vs$ temperature under isobaric conditions. $T_m$ represents the melting point. $T_{g,1}$ and $T_{g,2}$ are the glasses produced at the cooling rates of $Q_1$ and $Q_2$, where $Q_2 < Q_1$. $T_K$ is the Kauzmann temperature.

perature is approximately 100s. As the changes are continuous and rate dependent, it is not a true phase transition phenomenon. On cooling at a relatively slower rate, liquid is given longer time to achieve the desired structural arrangements resulting in lowering of the glass transition temperature. However, lowering of glass transition is of the order of few Kelvin per decade resulting in non-equilibrium state which is unavoidable. Note that the temperature-dependent changes of volume in glassy and as well as in crystalline state are quite similar. [59]

The characteristic features of thermal glass transition phenomenon are: (a) A sudden but continuous change in enthalpy leading to a step in heat capacity ($Cp = dH/dT$) $vs$ temperature plots. (b) Viscosity is of the order of $10^{13}$ poise (c) Non-linear thermal expansion ($\alpha = V^{-1}(dV/dT)$) as well as cooling rate dependent thermal expansion behavior around the glass transition temperature.(d) Occurance of the metastable glassy state below $T_g$ having excess free energy resulting in continuous equilibration process below the glass transition temperature (see section 2.3). This equilibration process involves a densification process and reduces the excess free energy, enthalpy and entropy. Driving force is the tendency of the system to achieve thermodynamically equilibrated liquid state. In cases where the material is crystallizable (Figure 2.1b), the entropy of the equilibrium liquid would be at some temperature ($T_K$) equal to the entropy of the crystalline phases. A further reduction of temperature would then result in $S_{liquid} < S_{Crystalline}$ which is unphysical. This situation is referred to as Kauzmann paradox. [1, 56, 60–62] Since $T_K$ is unaccessible and only determined based on

extrapolations, it is still a vital point of discussion whether or not $T_K$ is of main importance for understanding the glass transition phenomenon.

In an undisturbed equilibrium liquid above $T_g$, thermal fluctuations exists without any external perturbations. The intensity of these thermal fluctuations can be measured using a linear response measurements like dielectric spectroscopy, dynamic mechanical analysis etc. The susceptibilities obtained in the linear response measurement is related to the correlation function (in time domain) or by the spectral density (frequency domain) of thermal fluctuations according to Fluctuation-Dissipation-Theorem [63, 64] which is discussed in detail in section 4.1.2.

Slow fluctuations responsible for the time or temperature dependent softening behavior of glass forming materials in the equilibrium state under isothermal conditions is known as dynamic glass transition or $\alpha$ process. In a linear response measurement, the characteristic times of the fluctuations responsible for the $\alpha$ relaxation can be determined under isothermal conditions (see section 4.1.2). [65]

Typical features of a dynamic glass transition are non exponentiality as well as non-Arrhenius like dependency of the average relaxation time. Non-exponential time dependencies of susceptibilities like shear compliance $J(t)$, dielectric permitivity $\epsilon(t)$ etc. in linear response experiments are commonly observed. The behavior can be often approximated by the Kohlrausch-Williams-Watts (KWW) function

$$\phi(t) = \exp[-(\int_0^t \frac{dt}{\tau})^{\beta_{KWW}}] \tag{2.1}$$

where $\phi(t)$, $\tau$ and $\beta_{KWW}$ being relaxation function, relaxation time and Kohlrausch exponent respectively. Values of $\beta_{KWW}$ lie between 0 and 1. For a single Debye relaxator, value of $\beta_{KWW}$ equals 1 indicating the single exponential function. Whether $\beta_{KWW} < 1$ values observed for conventional $\alpha$ relaxation is a consequence of a superposition of many spatially distributed Debye relaxators or due to intrinsic broadening of all relaxing entities is still controversially debated. [66, 67] Non-exponential behavior can be explained assuming the existence of dynamic heterogeneities. [65]

The temperature dependence of the average relaxation frequency ($\omega_\alpha$) or relaxation time ($\tau_\alpha$) of the $\alpha$ relaxation which are related by $\omega_\alpha \tau_\alpha = 1$ is sketched in Arrhenius plot or relaxation map ($log\omega$ $vs.$ $1000/T$) as shown in Figure 2.2 as obtained from linear response
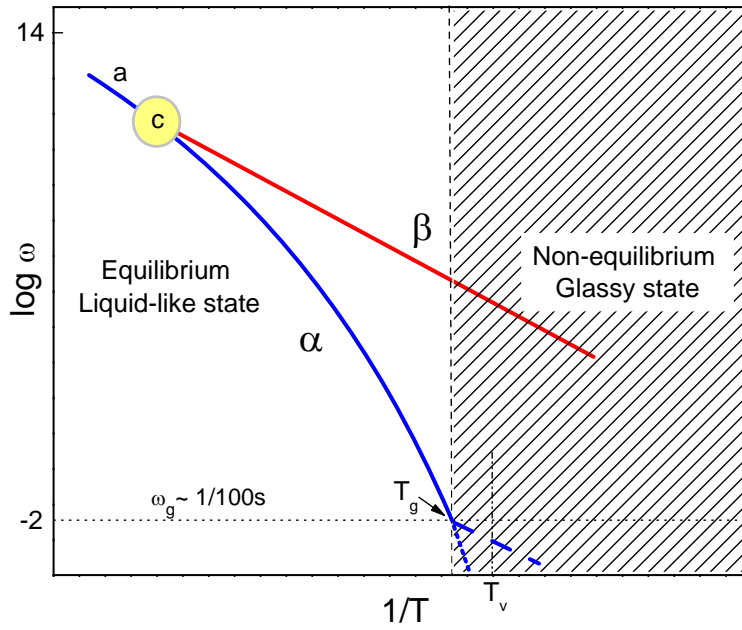
**Figure 2.2:** Arrhenius plot $log\omega$ $vs$ $1/T$ depicting dynamic glass transition process ($\alpha$), local dynamics ($\beta$), crossover region ($c$) where temperature dependence of $\alpha$ and $\beta$ approach eachother and high temperature process ($a$). $T_v$ corresponds to the Vogel temperature.

measurements. Typical is the non-Arrhenius like temperature dependence of dynamic glass transitions $\alpha$ as described above $T_g$ by Vogel-Fulcher-Tammann-Hesse (VFTH) equation. [65]

$$\log(\omega_\alpha) = \log(\omega_0) - (B/(T - T_v)) \tag{2.2}$$

where $\omega_0$, B and $T_v$ represent limiting frequency, curvature and Vogel temperature respectively. This is an extremely strong temperature dependence as compared to that of simply activated more local, non-cooperative motions seen in glasses as Johari-Goldstein relaxation processes ($\beta$ - relaxations) being intrinsic to the glassy state [68]. These relaxation processes have an Arrhenius like temperature dependency of the relaxation frequency expressed as

$$\log(\omega_\beta) = \log(\omega_0) - (E_A/RT) \tag{2.3}$$

with $E_A$ being the activation energy and R being the gas constant. Pressure plays an important role as it determines the position of the $\alpha$ trace in the relaxation map while $\beta$ process are only weakly pressure dependent.

**Phenomenological glass transition models**

The softening process and glass transition phenomena are studied over the several decades. Although many details are still not finally understood, it is accepted that (a) Free-volume model and (b) Thermodynamic based models taking the configurational entropy into consideration are able to describe important aspects.

(a) *Free-volume model* : According to this concept, the free volume ($V_f$) or the unoccupied volume under isothermal conditions controls the mobility of the molecules. Basic assumptions behind this theory are that (i) free volume is continuously redistributed without any expense of local free energy for this redistribution and (ii) molecular mobility is realized by movement of atoms or molecules into voids of approximately equal or greater than that of molecular dimensions. Motions of molecules lead to redistribution of free volume. [4, 5] Temperature dependency of free volume is connected according to Doolittle with the viscosity by [69, 70]

$$\eta = A \exp[b(V - V_f)/V_f] \tag{2.4}$$

where $V_f$ is the net available volume or free volume and $V_0 = V - V_f$ is the limiting volume of the liquid or Van der Waals volume of the molecules at 0K. With the decrease in temperature, contraction occurs and the packing density increases resulting in a reduced free volume and molecular mobility. At the glass transition, these translational diffusive motions freeze. Only localized relaxational motions are seen as Johari-Goldstein $\beta$ process [68] are preserved in the glassy state together with vibrational motions of the molecules which also show up in crystalline systems. The free volume approach has been used to explain strong temperature dependent changes in the $\alpha$ relaxation frequencies in equilibrium liquids based on the Williams-Landel-Ferry relation (WLF) [55]

$$\log(\frac{\omega_\alpha}{\omega_0}) = -\frac{(B/2.303)(T - T_0)}{(f_0/\alpha_f) + (T - T_0)} \tag{2.5}$$

where $f_0$ is the fractional free volume ( $V_f/V_0$) at the reference temperature $T_0$ and $\alpha_f$ is the thermal expansion coefficient. WLF equation is mathematically equivalent to the VFTH like equation as shown in equation 2.2.

(b) *Thermodynamic based models*: First thermodynamic approach to describe the glass tran-

sition starting from the configurational entropy ($S_c$) was proposed by Gibbs-DiMarzio [6]. $S_c$ has been defined in this model as the number of possible arrangements of the molecules on the lattice. Applying such a lattice model to polymers and assuming that the configurational entropy is a function of hole energy of the unoccupied sites, volume fraction of the holes and energy differences between local chain conformations a thermodynamic model was formulated. Upon cooling the system, densification takes place resulting in decrease of the volume fraction of the holes. This results in a decrease of the configurational entropy of the system and each polymer chain. Gibbs-DiMarzio proposed that the reduced configurational degree of freedom is responsible for the decrease in the viscosity of liquids during cooling. At the Kauzmann temperature, the number of possible arrangements for a chain on the lattice reduces to one indicating configurational entropy to become zero, resulting in a second order phase transition what is in some sense consistent with the paradoxical prediction by Kauzmann that $S_c \rightarrow 0$ at the Kauzmann temperature $T_K > 0K$.

Adapting the Gibbs-Marzio approach to explain the glass transition phenomenon, Adam and Gibbs [7] proposed the concept of cooperatively rearranging regions (CRRs). A CRR was defined as a subsystem which, upon a sufficient thermal fluctuation, can rearrange into another configuration independently of its environment. CRRs are also defined by the statistical independence of their thermal fluctuations related to the glass transition. [65] The concept assumes that a certain number of molecules z in a CRR is responsible for cooperative rearrangements. The CRR concept specifies the idea of the molecular cooperativity. Central message of the Adam-Gibbs paper is that the temperature dependence of the $\alpha$ relaxation in glass forming liquids can be explained essentially in terms of the temperature dependence of the size of CRRs. CRR size is predicted to decrease with increasing temperature. Central equation of the Adam-Gibbs paper is

$$\bar{W}(T) = \bar{A}\exp(-C/TS_c) \tag{2.6}$$

where $\bar{W}(T)$ is the transition probability which is inversely proportional to the relaxation time $\tau_\alpha$, and $C = \Delta\mu s_c^*/k$ is a constant defined by the potential energy required for the cooperative rearrangement $\Delta\mu$ and the limiting value for the configurational entropy $s_c^*$ corresponding to a minimum CRR size. k is the Boltzmann constant. This equation allows, making a few assumptions, to predict the temperature dependence of the CRR size but it does not allow to calculate CRR sizes or the number of cooperatively rearranging particles in CRR.

Quantitative predictions for the CRR sizes are made by the fluctuation approach proposed by Donth. [71] In this approach, the concept of CRRs was adapted and used the Fluctuation-Dissipation Theorem (FDT) [63] to estimate the number of cooperatively rearranging particles in a CRR, $N_\alpha$, and the volume of the CRR, $V_\alpha$. Assuming that the CRR is the representative subsystem related to cooperative $\alpha$ motion [65], calorimetric data have been used to calculate CRR sizes according to this model. The idea is to identify the fluctuations seen as $\alpha$ process in linear response experiments directly with a CRR. CRRs are assumed to be an intrinsic feature of glass forming liquids above $T_g$ leading to a spatio-temporal density pattern. The CRR is representative subsystem of this pattern and its size is temperature dependent. Central prediction of the fluctuation approach is that the number of cooperatively rearranging particles per CRR (or cooperativity) $N_\alpha$ can be calculated from

$$N_\alpha = \frac{R T_\alpha^2 \Delta(1/C_v)}{M_o \delta T^2} \tag{2.7}$$

where $R$, $T_\alpha$ and $\delta T$ correspond to gas constant, $\alpha$ relaxation temperature and temperature fluctuation estimated based on the width of the $\alpha$ relaxation in dynamic heat capacity data $C_p^*(\omega, T)$ respectively. $\Delta(1/C_v) = (1/C_{v,glass}) - (1/C_{v,liquid}) \approx \Delta(1/C_p) = (1/C_{p,glass}) - (1/C_{p,liquid})$ is the calorimetric $\alpha$ relaxation strength. $M_o$ is the molar mass of the particle.

Knowing the average density $\rho$, the CRR volume $V_\alpha$ can be calculated accordingly by

$$V_\alpha = \xi^3 = \frac{k_B T^2 \Delta(1/C_v)}{\rho \delta T^2} \tag{2.8}$$

Typical values for the characteristic length $\xi_\alpha$ are reported to be in the range of 7-22Å corresponding to $N_\alpha$ values in the range of 35-290 for six different glass forming liquids at $T_g$. [71] CRR sizes for different polymers has been estimated based on differential scanning calorimetry [72] and heat capacity spectroscopy [73,74] data. The results are consistent with the CRRs having sizes $\xi_\alpha$ in the range of 10-30Å and containing 10-300 particles.

Based on dynamic calorimetry measurements in a wide frequency temperature range, temperature dependent $N_\alpha(T)$ values have been calculated for selected polymers. It has been predicted that $[N_\alpha^{1/2} \propto (1-x)/x]$ with $x = (T - T_v)/(T_c - T_v)$ approximates the data between Vogel temperature $T_v$ and $\alpha\beta$ crossover $T_c$ as well. [75] This temperature dependence is different from that predicted by approaches based on configurational entropy $S_c(T)$ where proportionalities $[N_\alpha \propto T/(T - T_K)]$ [76] or $[N_\alpha \propto 1/(T - T_K)]$ [77] have been predicted

depending on the assumptions. Common for all approaches is that cooperativity and CRR size increase with decreasing temperature.

An alternative approach to calculate $\xi_\alpha$ and $N_\alpha$ based on enthalpic fluctuations has been proposed by other authors [78, 79]

$$N_\alpha = \frac{RT_\alpha^2}{\Delta C_v M_o \delta T^2} \tag{2.9}$$

with $\Delta C_v = C_{v,liquid} - C_{v,glass}$ being an alternative measure for the calorimetric $\alpha$ relaxation strength. It has been shown, however, that CRR sizes calculated based on this approach for glass forming liquids confined in nanoporous host systems gives too large $\xi_\alpha$ values while the $\xi_\alpha$ values calculated based on equation 2.7 are in agreement with the confinement size. [80]

## 2.2   Glass transitions under constraints

In this section, the effect of constraints on the glass transition is discussed. Rationalizing the situation, three main factors affecting the glass transition have been discussed in the literature: (i) true geometrical confinement (ii) density changes due to confinement and (iii) interfacial effects. In particular, the question whether or not and at which length scale true confinement effects exist seems to be of major importance for the discussion about the nature of the dynamic glass transitions $\alpha$. Deviations of the $\alpha$ dynamics in nanoscopic compartments are usually interpreted as an argument for the existence of CRRs in glass forming materials. According to the 'hindered glass transition' picture changes in the $\alpha$ dynamics should appear as soon as the CRR size approaches the domain size. [20, 65] The findings for glass-forming materials under constraints are extensively reviewed by Alcoutlabi and McKenna [81] and Alba-Simionesco. [82] A short overview of the results concerning the three main effects is given below.

*True geometrical confinement*: Geometrical confinement effects on $T_g$ and the $\alpha$ dynamics are often studied on small molecules [83–85] and low molecular weight polymeric systems [86–89] in controlled porous glasses (CPGs) as nanoporous host systems. Arndt et al [84] reported 8-15K shifts for confined salol in CPGs with mean pore diameter in the range 25Å to 75Å based on DSC and dielectric spectroscopy measurements. For propyleneglycol and glycerol the $T_g$ shifts are of the order of 4K in 25Å nanoporous Gelsil glasses as host. [83] Schönhals et al [86, 87, 89] studied PDMS and PMPS in CPGs (25Å -200Å) and found faster molecular dynamics in the pores as compared to bulk. Recently for polycyanurate in CPGs

having a mean pore diameter of 115Å, 60K depression in $T_g$ was observed. [88] Otherwise, studies by Kremer et al on liquids in zeolites showed no change in the $\alpha$ dynamics down to less than 10Å. [90] This shows how complicated it is to find common aspects. Note that all these results are obtained in surface treated host systems since strong surface interaction is known to influence the results. Nevertheless, the pore sizes where deviations from the bulk behavior start to appear are quite different reaching from less than 10Å to several 100Å in different studies.

Another class of materials where the influence of confinement on the softening behavior has been extensively studied are thin films where depression in $T_g$ is also reported. Keddie et al [23] observed a depression in the glass transition of upto 25K for the thin films of polystyrene on silicon substrates with the decreasing thickness of the films to around 100Å. Pioneering work on free standing films using ellipsometry as well as the Brillouin light scattering (BLS) by Forrest et al showed a decrease in the glass transition starting at 700Å thick films and reaching 70K for films which are 200Å thick. Depression in the $T_g$ appears to be stronger in free standing films. [21, 91, 92] Their interpretations were based on the spatial confinement as the estimated mass densities of all thin films was similar at room temperature and also similar to that of bulk. [92] In contrast to that, Kremer et al [93, 94] recently reported based on dielectric spectroscopy experiments that no depression in $T_g$ is seen for films with thickness down to about 48Å. Moreover, it has been shown that sample preparation, methodical aspects, molecular weights etc. can influence the experimental results significantly. [21, 95] This shows clearly that the findings are still controversially debated. [94, 96–98] The situation is hard to judge since surface interaction and sample preparation are obviously of major importance. The sizes where deviations from the bulk behavior start to appear in thin films is again varying a lot. Values between $\approx$20Å and several 100Å have been reported by many groups.

*Density changes due to confinement*: Variation of the glass transition on the density has been widely studied based on host-guest systems. Main conclusion pushed by different groups is that the density of the confined liquid is not same as that of the bulk. Due to density changes, a shift in the glass transition temperature is observed. [99] A pioneering work in this field is by McKenna [14] where nanoporous host guest systems (o-terphenyl and benzyl alcohol in controlled porous glass) are studied and $T_g$ reduction is reported which is of the order of 18K for 40Å pores. Broadening of the glass transitions are simultaneously observed. Shifts in the $T_g$ has been discussed in light of density effects and finite size effects. [81] Parallely, density measurements on toluene in MCM-41 and SBA-15 host systems with pore diameters

in the range of 24 - 87Å showed a decrease in average density in the pores as compared to the bulk toluene using neutron scattering accounting for the decrease in $T_g$. [17,100] Similar findings are also reported for small molecular liquids like o-terphenyl in CPGs where reduced densities of the confined o-terphenyl is estimated. [101] Density changes in case of thin films have been rejected as a reason for shifts in $T_g$. [92] The discussion about the influence of thin film preparation, annealing etc. however is vital [95] showing that the details are far from being clear.

*Interfacial Effects*: Over the years, many experiments have been performed on different host-guest systems showing that the liquids near the pore walls exhibit higher $T_g$ while material away from the pore walls to the core has a reduced $T_g$ as compared to bulk like liquid. [15–17, 88, 102–104] In other words, from the pore walls to the core, an increase in the molecular mobility is observed. Two phase models explaining these effects have been predicted. [84, 105] Richert et al [106] showed that by confining 3-methyl pentane in porous glass with 75Å diameter, interfacial effects dominates and an increase in the $T_g$ is observed. For thin films, reduced mobility at the interfaces of the substrate and increased mobility at free surfaces have been reported and discussed in connection with changes of the local $T_g$. [22, 107]

Attempting to rationalize the findings one can conclude that all three above mentioned factors affect the glass transition in the confinement. To explain the results solely on the basis of one factor is often impossible as contributions from other factors cannot be ruled out. This makes it complicated to draw final conclusions about the existence of CRRs and dynamic heterogeneities based on the experimental results which are published for host-guest systems and thin polymer films. An answer to this question, is however, very important for the progress in understanding the softening behavior of glass forming materials in general. Excellent model systems to come to new insights might be self assembled side chain polymers where very small alkyl nanodomains with typical dimensions in the range 10-30Å are formed. [18,19,25,29,33,108,109] It has been shown for poly(n-alkyl acrylates) and poly(n-alkyl methacrylates) that the cooperative $\alpha_{PE}$ dynamics of the $CH_2$ units within the alkyl nanodomains depends systematically on the domain size. [18,25] A decrease in the relaxation temperature $T_{\alpha_{PE}}$ and fragility $m_{\alpha_{PE}}$ have been reported with decreasing domain size. This has been interpreted as indication for the existence of CRRs according to the hindered glass transition picture. [20,65] The effects of density, interfacial constraints and non-equilibrium have, however, not been considered for this class of comb-like polymers. This is a starting point for detailed experiments on P3ATs with different regio-regularity and side chain length

in this work and will be discussed in detail later in this thesis.

## 2.3  Physical aging and its effects on the dynamics

Physical aging is a structural relaxation process in the non-equilibrium glassy state below $T_g$ towards the equilibrium liquid state. This process incorporates significant changes in practically all physical quantities like volume, enthalpy, entropy etc. and influences mechanical properties like modulus, damping or creep and stress relaxation rates. In last decades, this phenomenon is extensively studied and reviewed by many authors. [59, 110–114]
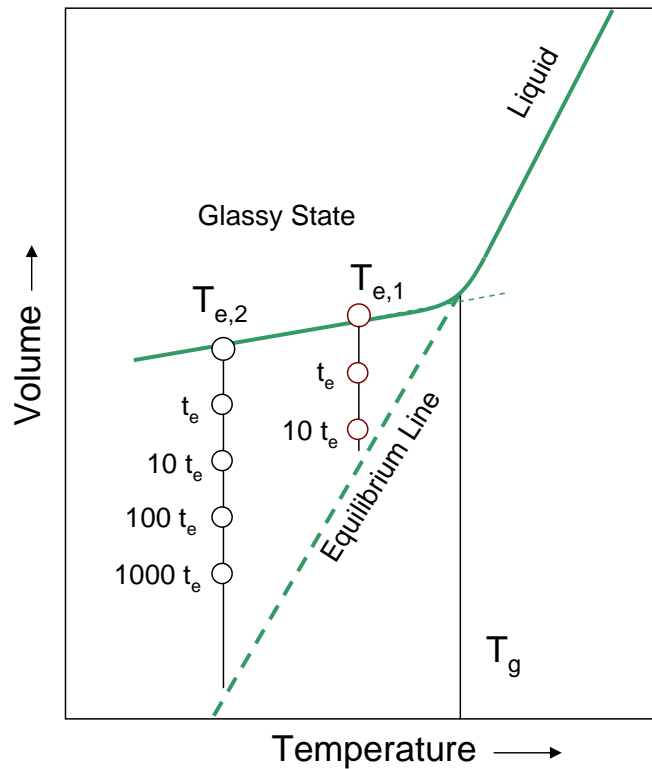


**Figure 2.3:** Schematic volume $vs$ temperature plot showing the effects of isothermal physical aging under isobaric conditions. $T_e$ and $t_e$ are the annealing temperatures and times respectively.

A classical method to study physical aging is to investigate tiny changes in volume or density during isothermal annealing for long times below $T_g$. Physical aging effects could be visualized in a volume vs. temperature plot as shown in figure 2.3. Consider a sample which is cooled at a rate $Q$ and falls out of the equilibrium at temperature $T_g$ where it becomes glassy. If the sample is then annealed below $T_g$, at an annealing temperature $T_e$ for a certain

time $t_e$, volume will decrease to reach its equilibrium value. Enthalpy and entropy will also follow similar trends. Due to densification, new metastable states are formed as long as the equilibrium density is not reached.
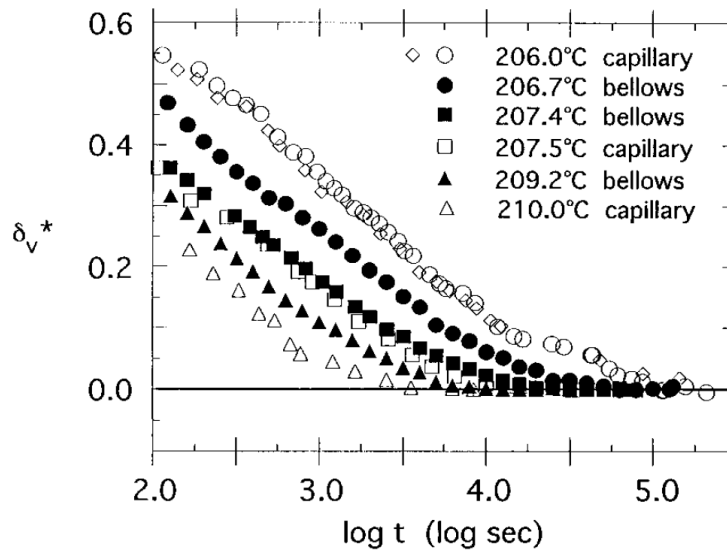


**Figure 2.4:** Normalized volume as a function of aging time for different temperatures $T_e$ after the quenches from $210^{\circ}$C to different aging temperatures as given in the legend for polyetherimide ($T_g$=207.5°C). Taken from [115]

Experimentally, many authors have studied physical aging in amorphous polymeric glasses using volume dilatometry. [59, 111, 115, 116] Data from isothermal physical aging experiments on polyetherimide are shown as an example in Figure 2.4. [115] Normalized volume ($\delta_v^* = [(v_t - v_\infty)/(v_o - v_\infty)]$, where $v(t)$ is the time dependent specific volume, $v_o$ the initial specific volume at the aging temperature and $v_\infty$ is the specific volume at equilibrium), decreases linearly with $log t_e$ until the equilibrium is approached for long annealing times and $\delta_v^*$ becomes nearly zero. The densification is faster below $T_g$ since the mobility of the glass is higher at that temperatures. Equilibration should finalize on time scales which are proportional to the equilibrium $\alpha$ relaxation time $\tau_\alpha$ at $T_e$. Otherwise, the driving force $V_{glass} - V_{liquid}$ in Figure 2.3 is larger far below $T_g$ and the total changes due to physical aging are more pronounced. Many more complicated aging experiments are performed and different models have been proposed to understand the linear range where $\delta_v^* \propto log t_e$. A final molecular understanding is still missing like in case of glass transition. Details will not be discussed here since density is not measured for our samples and quantitative analysis of aging effects can not be done for the nanophase separated side chain polymers studied in this

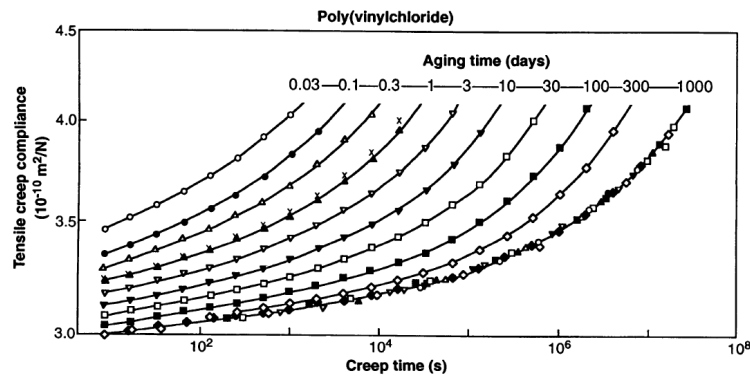work. Readers are referred to the literature. [110, 111]



**Figure 2.5:** Tensile creep compliance $vs$ creep time for polyvinyl chloride (PVC) ($T_g = 80^\circ C$). Samples were quenched from $90^\circ$C to $20^\circ$C and aged at $20^\circ$C for .03 to 1000 days. After 1000 days sample was re-quenched to $20^\circ$C and measured after 1 day of annealing at $20^\circ$C. Taken from [59, 114]

Apart from dilatometry, linear response techniques can also be used to detect physical aging since the $\alpha$ relaxation is strongly influenced by non-equilibrium below $T_g$. In particular, physical aging significantly changes the mechanical properties. This can be systematically studied by linear response methods like creep etc. (see section 4.1.2) This approach was pioneered by Struik. [59] Struik measured the creep compliance for isothermally aged samples after different annealing times from 0.03 days to 1000 days. Representative results for polyvinyl chloride are presented in Figure 2.5 showing small-strain creep compliance $vs$ creep time after different aging times $t_e$. It is clearly seen that creep curves with the increasing annealing time at $T_e = 20^\circ$C shifts systematically to longer creep times without significant change of the curve shape. This equilibration process continues even after extremely long annealing times of 3 years. This can be explained on the basis of a decrease in the free volume ($V_f$) as well as configurational entropy ($S_c$) resulting in longer $\alpha$ relaxation times. Obviously, the shape of the creep curve (non-exponential behavior) and Kohlrausch parameter $\beta_{KWW}$ remains similar for all the aging times and hence an empirical formula has been proposed to quantify changes due to physical aging in relaxation curves which is

$$log\tau = log\tau_o + \mu log t_e \qquad (2.10)$$

where $\tau$ is the average relaxation time after the isothermal annealing step, $t_e$ is the isothermal annealing time, $\tau_0$ is the average relaxation time before annealing and $\mu$ is the Struik factor

describing the shift. It can be seen in Figure 2.5 that if master curve is constructed according to this empirical equation all the curve collapse on the curve after 1000 days of aging. However, it should be noted that $\mu$ is system specific and varies in the range $0.8 \leq \mu \leq 1$. Note that, reversibility of the physical aging phenomenon is also shown in Figure 2.5. The aged PVC sample was reheated to $90^{\circ}C$ above $T_g$ and annealed at room temperature for 1 day. Crossed points is the creep compliance obtained afterwards which is in good agreement with the initially obtained result after 1 day of physical aging.

Note that localized motions seen as Johari-Goldstein $\beta$ relaxation in glasses are only weakly influenced by physical aging. Reduction of the $\beta$ intensity and small frequency shifts have been reported. [117]
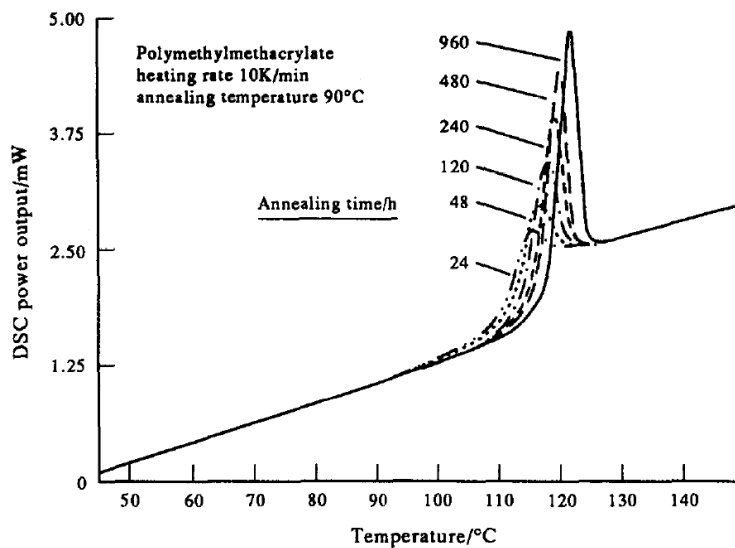


**Figure 2.6:** DSC heating scans for polymethylmethacrylate ($T_g \approx 105°C$) performed after annealing at $T_e = 90^{\circ}C$ for different annealing times indicated. The heating rate is 10K/min. Taken from [111]

Another large number of physical aging experiments often called structural relaxation experiments have been performed using calorimetry. Aim is to follow up the decrease of enthalpy and entropy as the system tends to achieve equilibrium during physical aging below $T_g$. Such effects could be probed by conventional differential scanning calorimetry. The decrease of enthalpy during annealing at $T_e$ has to recover and shows up as an endotherm following the glass transition step in subsequent DSC heating scans, often stated as structural relaxation or enthalpy relaxation peak. Figure 2.6 data for polymethylmethacrylate as a typical example. [111] Heating scan following the annealing at $T_e = 90^{\circ}C$ for varied annealing times are

presented. With the increase in the annealing time, the enthalpy or structural relaxation peak appears and the area of the peak increases linearly on the logarithmic time scales. There is a whole class of models like Tool-Narayanaswamy-Moynihan model, KAHR model etc. developed to describe non-equilibrium phenomena below $T_g$ as well as heating and cooling curves near the thermal glass transition where equilibrium $\alpha$ fluctuations freeze-in. Such models are reviewed in references [110, 111, 113] but have not been applied to the DSC measurements performed in this work on nanophase-separated side chain polymers. Main target of the DSC measurements in this work is usually to detect the crystalline fractions in our sample. In some cases, isothermal annealing experiments below $T_g$ are performed. But also then crystallization and structural relaxation effects are superimposed and it is impossible to apply these models to quantify structural relaxation effects.

To summarize, amorphous solids are not in thermodynamic equilibrium below the glass transition temperature and have larger volume, enthalpy and entropy than the equilibrium liquid state. During annealing at a certain temperature in the glassy state, the non-equilibrium glass having excess thermodynamic quantities drives towards the equilibrium liquid state reducing these thermodynamic quantities. Far below $T_g$, the equilibration time is large while close to $T_g$ equilibration time is short and measurable. Thermal fluctuations or mobility in the glassy state are non zero below $T_g$ and drive the reduction of free volume and configurational entropy.

## 2.4   Side chain crystallization

From a thermodynamic point of view, the crystalline state is stable below the bulk melting temperature $T_m$ since the crystals have lower Gibbs free energy $G$ than the liquid state as shown in Figure 2.7a. However, crystallization appears below $T_m$ since significant supercooling $\Delta T = T_m - T_c$ is usually necessary to form stable nuclei by homogeneous nucleation and growth of the crystallites. Prerequisites for the polymer crystallization is the formation of the stable nuclei and the growth. Stable nuclei are formed after crossing a certain energy barrier which is required to form the nuclei of the critical size. After formation of the nuclei, the crystal growth takes place spontaneously driven by the decrease in the free energy $\Delta G = G_{liq} - G_{crys}$. Growth rate u has an optimum between glass transition temperature ($T_g$) of the polymer and the equilibrium melting temperature ($T_m$) (Figure 2.7b) as at low temperature near the glass transition the segmental mobility is low which hinders the growth while at high temperatures near the melting point equal probability of attachment
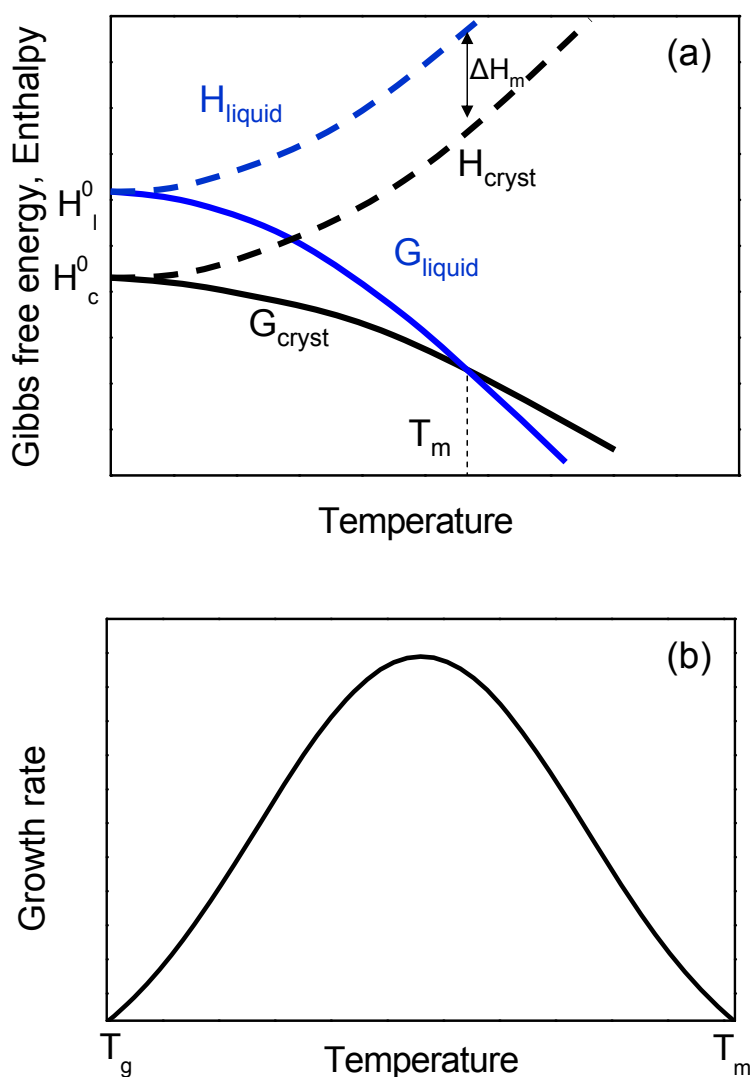
**Figure 2.7:** (a) Gibbs free energy (G) and enthalpy (H) vs. temperature for crystallizable solid under isobaric conditions. (b) Growth rate vs. temperature for crystallizable solid.

and detachment of chain segments occurs since the energetical gain due to crystallization is minimized. [118–120] Polymer crystals usually occur in $\approx 100$Å thick folded lamellae which are stapled together separated by the amorphous regions. In case of crystallizable main chain polymers, the crystalline lamellae form usually a spherulitic superstructure.

Many approaches in the literature exist describing polymer crystallization in polyethylene and related main chain polymers [118, 121, 122] but less is done to model and understand polymers with crystallizable side chains. Side-chain polymers having long alkyl groups [29, 33, 53, 109] are an interesting class and application relevant crystallizable materials. One

example where systematic studies using DSC, x-ray scattering and relaxation spectroscopy methods have been performed in order to understand side chain crystallization are atactic poly (n-alkyl methacrylates). [49, 51, 53]
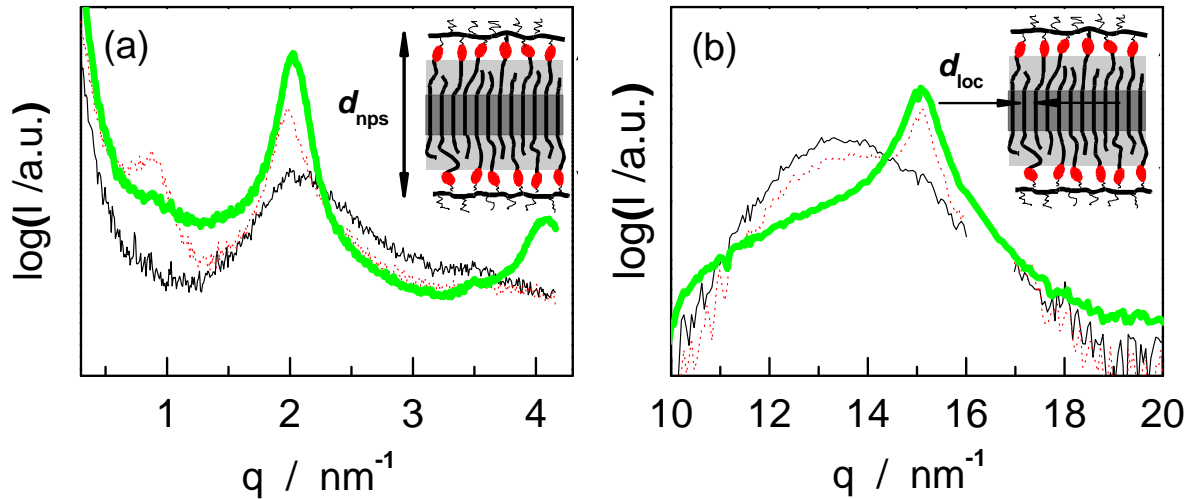


**Figure 2.8:** X-ray scattering results on poly(n-octadecyl methacrylate). (a) Intermediate range and (b) wide angle x-ray scattering for amorphous side chains (thin lines) and semi-crystalline side chains (dotted and thick lines). Adapted from [51]

In particular, poly(n-octadecyl methacrylate) [PODMA] with C=18 methylene units per side chains is well investigated. The main feature in the scattering data for molten PODMA is the appearance of pre-peak in the intermediate range (Figure 2.8a) indicating nanophase separation of main and side chain parts. This broad amorphous peak at around $q = 2nm^{-1}$ sharpens up and shifts to lower $q$ values upon side chain crystallization indicating formation of an all trans configuration of methylene units in turn increasing main chain to main chain distances. This is accompanied by appearance of higher order peaks and a sharp peak on the top of the amorphous halo in WAXS data (Figure 2.8b) corresponding to a distance $d_{loc}$ of about 4.6Å between alkyl stems packed on a hexagonal lattice. A sharp melting peak around $40°C$ appears in DSC scans showing melting of crystals in the alkyl nanodomains. Detailed isothermal crystallization measurements on PODMA show an abrupt increase in degree of crystallinity $D_c$ without significant change in melting temperature $T_m$ for short times interpreted as primary crystallization step. This step is followed by a secondary crystallization step which is characterized by a linear increase of $D_c$ with logarithmic crystallization time. This effect is accompanied by a linear increase in $T_m$ indicating thickening of crystalline lamellae in accordance to the Gibbs-Thomson equation ($T_m \propto 1/thickness$). A hypothetical picture is proposed assuming that alkyl groups are basically interdigitated and that

crystallization appears away from the main chains in the middle of the alkyl nanodomains. The picture predicts that crystallization appears starting from a nanophase separated melt. Homogeneous nuclei can form easily since the alkyl groups are highly extended far away from the backbone. Primary crystallization is related to lateral growth of thin lamellae followed by crystal thickening during secondary crystallization. For side chains to crystallize, alkyl groups has to overcome frustration introduced by the immobile main chains. This works only if the side chains are long enough. Thus, side chain crystallization appears often only in systems with more than 10-12 carbon per side chains. In a way, crystalline states are stabilized in side chain polymers containing alkyl groups which are hard to detect in bulk polyethylene. [51] Hexagonally packed alkyl stems are found instead of orthorhombic packing which is typical for polyethylene.

There is an interesting analogy to the multistage model by Strobl G. [118,123,124] predicting the situation at the growth front of polyethylene crystal.
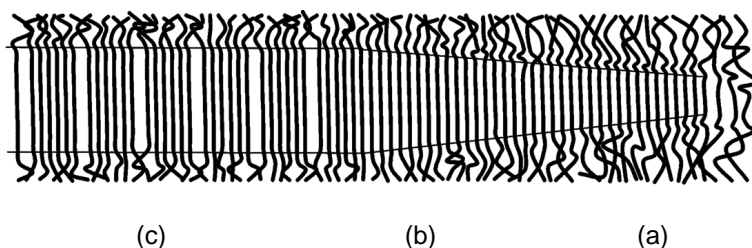


(c)                              (b)                              (a)

**Figure 2.9:** Multistage model for polymer crystallization with three different zones.(a) growing mesomorphic layer, (b) Solidification by core crystallization and (c) stabilization by surface ordering. Adapted from [118, 125]

This model predicts that the crystallization process in polymers like polyethylene occurs via a metastable mesophase. Early stages of crystallization are characterized by mesophase which is differently packed as compared to the final crystal. Mesophase is the transient state which is composed of stretched sequences between crystal face and melt in a liquid like cylindrical packing which are stabilized by epitaxial forces. Volume fraction of the mesophase is quite small as compared to the final crystal. Describing the process, the straightened chain sequences attach to the boundary face of the mesomorphic layer, thickening the mesomorphic layer with time. On reaching certain critical thickness the layer part solidifies by structural transition resulting in formation of planar crystal blocks which in turn merge to form homogeneous lamellar crystallite as shown in Figure 2.9. [123, 124] For bulk polyethylene, it is reported that nucleation occurs in hexagonal metastable phase which transforms into more

stable orthorhombic phase. [126, 127] Still a lot of questions are open about the mesophase and the physical background of this phenomenon.

On comparing the pictures shown in Figure 2.9 and inset Figure 2.8, situation seems to be quite similar at the growth front of crystallization process and within the nanophase separated side chain domains of the size of 10-20Å. A common feature in both cases is occurance of hexagonally packed methylene sequences. Recently, for eicosylated polyethyleneimine with C=20, polymorphism within alkyl nanodomains and a transition from metastable hexagonally packed phase to orthorhombic phase has been reported. [128] Considering these findings, confined side chain crystallization in alkyl nanodomains can be an effective tool to study early stages of crystallization. [129]

# Chapter 3

# Aim of this work

Two series of regio-random and regio-regular poly(3-alkyl thiophene-2,5diyl) with different side chain lengths will be used in this thesis work as model systems to study:

• *Nanophase separation effects* in side chain polymers, i.e. demixing of main and side chains on length scales of about 10-30Å as reported for other side chain polymers containing alkyl groups and considered as general phenomenon in such polymers with comb-like architecture.

• *Confined dynamics in self assembled alkyl nanodomains* surrounded by disordered or crystalline thiophene rings, being an experimental approach to contribute to the discussion about cooperatively rearranging regions (CRRs) and the nature of glass transition.

• *Hindered side chain crystallization* in alkyl nanodomains and the influence of domain size and main chain packing on degree of crystallinity, crystallization kinetics and crystal lattice (polymorphism) of the methylene units.

• *Long term effects* in nanophase separated P3ATs driven by side chain crystallization and physical aging-like densification processes below $T_g$.

# Chapter 4

# Methods and materials

In this chapter, the main methods and samples used in this work are described.

## 4.1 Methods

### 4.1.1 Differential Scanning Calorimetry

Change in the physical state of a material is accompanied by liberation or absorption of heat considering phase transitions or changes in total heat capacity considering glass transitions. In a particular physical state, the heat capacity of a material changes only slightly with temperature, while alters significantly at a change of state. Calorimeters are designed to determine phase transitions like crystallization, melting and glass transitions. Differential scanning calorimetry is one favorable method providing qualitative and quantitative information about heat capacity or enthalpy. [61, 119]

Basic principle of differential scanning calorimetry (DSC) is the measurement of the difference in the heat flow rate to the sample and to a reference sample being normally an empty pan on application of a controlled temperature program in form of temperature ramps. DSC instruments are classified into two main types on basis of their functioning: (a) Heat Flux DSC where the temperature difference between sample and reference $(T_S - T_R)$ is proportional to the heat flow rate difference $(\phi_S - \phi_R)$ containing the information about the calorimetric response of the sample; and (b) Power Compensation DSC where the difference in the temperature between the sample and the reference is controlled in such a way that this temperature difference is always close to null by supplying additional electrical power. The additional power difference $(P_S - P_R)$ is then proportional to the heat flow rate $(\phi_S - \phi_R)$. In this work, a power compensated DSC is used which is described in more detail below:
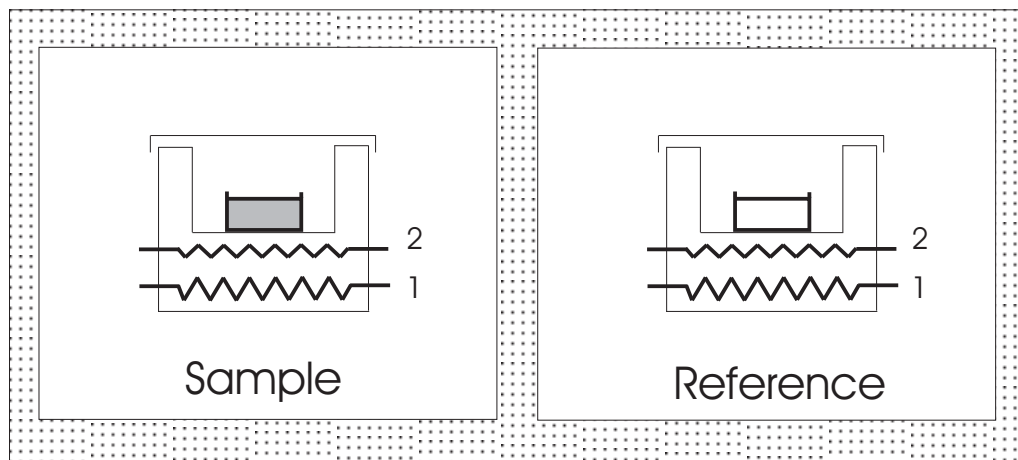
*Power compensated DSC*



**Figure 4.1:** Schematic representation of a power compensation differential scanning calorimeter consisting of two identical micro furnaces containing (1) heater and (2) temperature sensor. The block surrounding both microfurnaces is kept at a constant temperature T.

Mode of operation for the power compensation DSC is isoperibolic as the temperature of the surroundings remains constant which is maintained by isolation jacket. The measuring system consists of two identical micro-furnaces with platinum temperature sensors (2) and heaters (1) inside a small metallic block. Since the two furnaces have separate heaters, both can follow a given time-temperature program. In case of ideal symmetry between two measuring systems, same heating power is required by them to maintain the same temperature. Small instrumental asymmetrics, the heat capacity of the sample as well as exothermic or endothermic processes in the sample disturb the symmetry between the furnaces. Additional power is supplied to the sample or reference furnace to maintain the temperature difference to null. The measured signal is the compensation power supplied to achieve null temperature difference between the two furnaces and is proportional to the heat flux consumed or produced by the sample. [61] Quantity which is finally achieved is heat flow rate ($\Delta\phi = \phi_S - \phi_R$) (mW or mJ/s) as a function of temperature. Further to calculate the heat capacity (J/gK) of the sample as a function of temperature, baseline corrections have to be performed i.e. heat flow rate from empty pan measurements are subtracted from the sample measurements and the obtained heat flow rate has to be divided by the scan rate ($dT/dt$) and mass of the sample m.

$$C_p = \Delta\phi_m/(dT/dt)m \tag{4.1}$$

*Temperature modulated differential scanning calorimetry*

While simple heating or cooling programs are applied in case of classical DSC, basic working principle of temperature modulated DSC (TMDSC) is that the sample is heated or cooled at a constant underlying rate simultaneously superimposed by a sinusoidal time-temperature modulation. The heat flow rate obtained in these measurements can be separated into two parts i.e. the total heat flow and the periodic part of the heat flow. The latter consists of (i) reversible part i.e. in phase with the time derivative of temperature program and (ii) a part which is out of phase compared to $dT/dt$. TMDSC is a linear response method i.e. temperature perturbations during dynamic oscillations are sufficiently small and the underlying heating or cooling rate is small enough to be neglected in the analysis of a single period. The total heat flow gives $C_p$ corresponding to a conventional DSC scan and the periodic part yields dynamic heat capacity $C_p^*=C_p'-iC_p''$ which is a compliance like quantity in the sense of linear response. The real part $C_p'$ does not include any irreversible changes while the imaginary part $C_p''$ which is 90° out of phase represents entropy production over one perturbation cycle. Corresponding to a step in $C_p'$ a peak in $C_p''$ appears. Advantages of TMDSC over the conventional DSC is that the dynamic glass transitions can be separated from irreversible processes like crystallization, melting, relaxation enthalpy, decompositions, reactions etc. [130] Analysis for TMDSC data has been done as described by Weyer et al. [131]
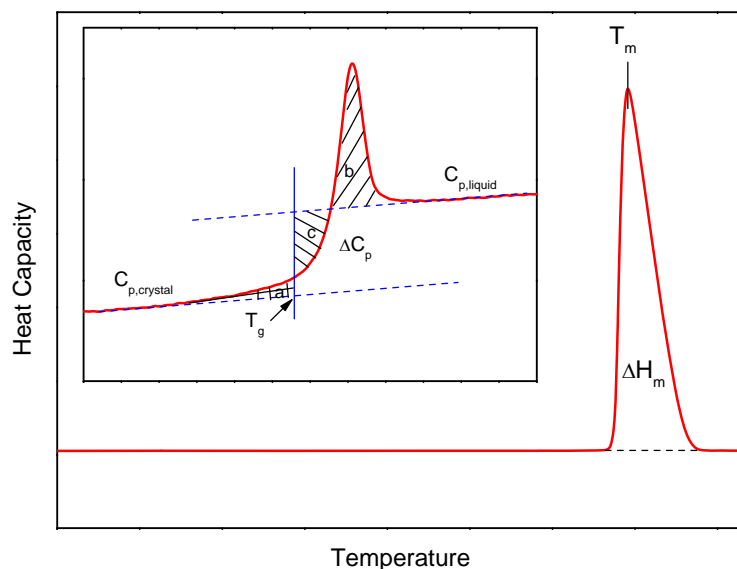
*DSC data evaluation*



**Figure 4.2:** DSC data analysis for melting peak. Inset shows the analysis of the glass transition.

Exothermic or endothermic peaks in DSC scans corresponding to crystallization or melting respectively are analyzed in the following ways (Figure 4.2).

(i) *Enthalpy of melting ($\Delta H_m$)* is calculated based on the area under the the endothermic peak using a base line connecting the liquid like state to crystalline state.

(ii) *Melting temperature ($T_m$)* is the peak maximum point of the endothermic peak.

Thermal glass transitions are connected with a step in the heat capacity ($C_p$) as shown in inset of Figure 4.2.

(i) *Glass transition temperatures ($T_g$)* can be determined from the equal area construction where $T_g$ is defined by the equivalence of the areas c=a+b as shown in Figure 4.2. Alternatively, half step $T_g$s can be used which is defined as temperature where the measured $C_p$(T) corresponds to $(C_{liquid} + C_{glass})$/2 as taken from the linear extrapolation.

(ii) *Glass step height $\Delta C_p$* is defined as difference between the extrapolated $C_p$ values of liquid and glass at $T_g$.

***Instruments used.*** DSC measurements are performed on Perkin Elmer DSC7 and Perkin Elmer Pyris Diamond instruments. Samples with a mass of about 5mg were encapsulated in hermetically sealed 30$\mu$l and 10$\mu$l open pans.

## 4.1.2 Dynamic Mechanical Analysis

Dynamic mechanical analysis (DMA) is the technique of applying stress or strain and further analyze the response to obtain phase angle and deformation data for viscoelastic polymeric systems. This technique belongs to the class of linear response technique whose basis is by the fluctuation-dissipation-theorem (FDT) introduced by Nyquist in 1928. [63]

***Working Principle.*** If a small periodic sinusoidal strain is applied as perturbation to a viscoelastic system, the response is a sinusoidal stress but will be out of phase with strain as shown in figure 4.3. Sinusoidal strain perturbation $\epsilon$ and stress response $\sigma$ will have same angular frequency $\omega$ which can be mathematically expressed as

$$Program : \epsilon = \epsilon_0 sin(\omega t) \tag{4.2}$$

$$Response : \sigma = \sigma_0 sin(\omega t + \delta) \tag{4.3}$$

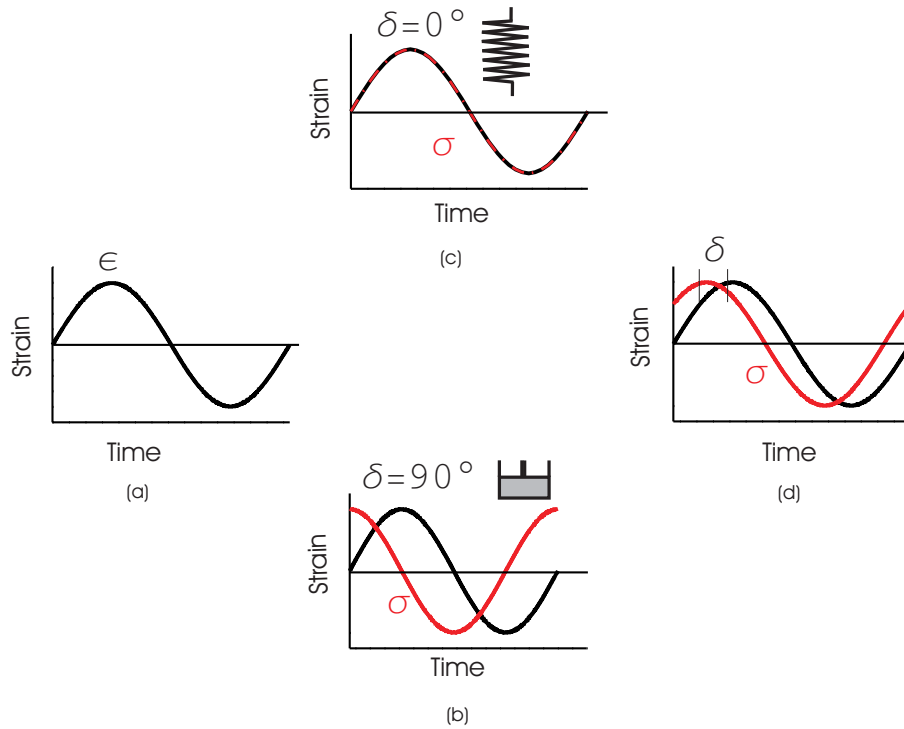**Figure 4.3:** (a) Sinusoidal strain applied to the samples (black). Response to sinusoidal stress (red) for perfectly viscous system (b), for elastic system (c) and for a polymeric system where it lies in between these two extremes (d). Adapted from [132].

Expanding the equation for the response one gets

$$\sigma = \epsilon_0 G' sin\omega t + \epsilon_0 G'' cos\omega t \tag{4.4}$$

where $G' = \frac{\sigma_0}{\epsilon_0} cos\delta$ and $G'' = \frac{\sigma_0}{\epsilon_0} sin\delta$. In complex notation, storage modulus $G'$ and loss modulus $G''$ can be combined to a dynamic modulus $G^*$ which can be written as

$$G^*(\omega) = G' + iG'' \tag{4.5}$$

The storage modulus $G'$ is related to the energy stored by the system, or the elastic part of the response and the loss part $G''$ which is related to the dissipation of energy by the system, i.e. part of the mechanical energy converted to heat, or the viscous part of the response which is $(\pi/2)$ out of phase with the applied strain. Alternatively, one can express the experimental observations in the form of a dynamic compliance $J^*(\omega) = 1/G^*(\omega) = J' - iJ''$ with $J'$ being the storage part and $J''$ being loss part.

***Linear response and Fluctuation Dissipation Theorem (FDT).*** As long as the perturbations are sufficiently small, dynamic modulus $G^*(\omega)$ and compliance $J^*(\omega)$ are not dependent on the amplitude of the perturbation. This defines the linear response regime. In the linear response case, two small overlapping perturbations lead to a linear superposition of their individual responses following Boltzmann's superposition principle.

Central advantage of susceptibilities taken from linear response experiments like $G^*(\omega)$ and $J^*(\omega)$ from DMA, is that these quantities are connected with equilibrium fluctuations in the undisturbed system. In the time domain, the FDT is describing the connection between relaxation time-dependent modulus $G(\tau)$ and compliance $J(\tau)$ and the corresponding correlation functions $\sigma^2(\tau)$ and $\epsilon^2(\tau)$ respectively. [65] It can be written as

$$\epsilon^2(\tau) = -kT(J(\tau) - J_e) \tag{4.6}$$

$$\sigma^2(\tau) = kT(G(\tau) - G_e) \tag{4.7}$$

where k is the Boltzmann constant and $G_e$ and $J_e$ are equilibrium modulus and equilibrium compliance respectively. The corresponding relations in the frequency domain are

$$\epsilon^2(\omega) = -kT\left(\frac{J''(\omega)}{\pi\omega}\right) \tag{4.8}$$

$$\sigma^2(\omega) = kT\left(\frac{G''(\omega)}{\pi\omega}\right) \tag{4.9}$$

where $\epsilon^2(\omega)$ and $\sigma^2(\omega)$ are the spectral densities characterizing the strain and stress fluctuations at frequency $\omega$. $\epsilon^2(\omega)$ and $\sigma^2(\omega)$ are related via a Fourier transform with $\epsilon^2(\tau)$ and $\sigma^2(\tau)$.

***Mechanistic models and spectra.*** Mechanical properties of viscoelastic materials can be modeled with simple spring and dashpot models where spring represents the elastic component and dashpot represents the viscous part. Relaxation is modeled in this simplified framework by the Maxwell element with spring and dashpot connected in series. For a single Maxwell element, one gets

$$G(t) = G_0 exp(-t/\tau) \tag{4.10}$$

$$\tau = \frac{\eta_0}{G_0} \tag{4.11}$$

where $G_0$ is the modulus of the spring and $\eta_0$ is the viscosity of the dashpot. A series of such

Maxwell elements gives the relaxation spectrum defined by

$$G(t) = G_e + \int_{-\infty}^{\infty} Hexp(\frac{-t}{\tau})dln\tau \tag{4.12}$$

where $G_e$ is added to allow discrete contribution to the spectrum at $\tau = \infty$ for viscoelastic solids and for viscoelastic liquids it is 0. $H(\tau)$ is the relaxation time spectra and $H \cdot dln\tau$ gives contribution of debye relaxators having relaxation times between $ln\tau$ and $ln\tau + dln\tau$. Similarly, to model the compliances $J(t)$, a series of Kelvin-Voit elements can be used where in a single entity spring and dashpot are connected in parallel, mathematically expressed as

$$J(t) = J_g + \int_{-\infty}^{\infty} L[1 - exp(\frac{-t}{\tau})]dln\tau + \frac{t}{\eta_0} \tag{4.13}$$

where $L(\tau)$ is the retardation time spectrum, $J_g$ is added to allow for the possibility of a discrete contribution at $\tau = 0$ and $\frac{t}{\eta_0}$ is the flow contribution. [55, 133] Related equations can be derived for the frequency domain accordingly. For Maxwell element, one gets Debye function

$$G^*(\omega) = G_e + \Delta G\frac{i\omega\tau}{1 + i\omega\tau} = G_e + \Delta G[\frac{(\omega^2\tau^2 + i\omega\tau)}{(1 + \omega^2\tau^2)}] \tag{4.14}$$

where $\Delta G$ is the step height across the dispersion zone or sometimes called as relaxation strength. The relaxation spectrum is given as

$$G'(\omega) = G_e + \int_{-\infty}^{\infty} [\frac{H\omega^2\tau^2}{(1 + \omega^2\tau^2)}]dln\tau \tag{4.15}$$

$$G''(\omega) = \int_{-\infty}^{\infty} [\frac{H\omega\tau}{(1 + \omega^2\tau^2)}]dln\tau \tag{4.16}$$

***Instruments used***. Anton Paar MCR501 and Rheometrics RDAII are used for the measurements. The dynamic shear modulus $G^* = G' + iG''$ was measured with a using a control strain of 0.1% being well in the linear range as confirmed by strain sweeps. Stripes having dimensions of about 18 x 4 x 1 mm$^3$ are used if the storage modulus $G'$ is $> 10^6$Pa, while parallel plates having a diameter of 8 mm and 1mm thick samples are used if $G'$ is $< 10^6$Pa. Regio-random samples were pressed in a hot press at 100°C and regio-regular were pressed above the melting point and immediately mounted in the instruments at room temperature. Changes in the sample dimensions due to densification are not corrected.

### 4.1.3  X-ray Scattering

X-ray scattering is the main method used to obtain the structural information about the samples in this work. X-rays have a relatively short wavelengths $10^{-2}$ to $10^{2}$Å with high energies of about 100eV to 100KeV of electromagnetic radiation. X-rays used for structural analysis have usually wavelength in the range 0.5 to 2.5Å. For polymers, mainly $CuK\alpha$ radiation is used having wavelength of 1.5418Å. Diffraction pattern depend on the structure of the investigated samples, wavelength of the x-rays and the scattering geometry expressed as scattering angle $\theta$. If the wavelength is comparable or smaller than the lattice constants, we find the scattered photons in directions different from the incident beam direction. Primary scattering is due to an interaction of x-ray photon with electrons in the sample. Hence, an electron density contrast is required to detect a certain structure. Photons scattered by different atoms can interfere with each other which results in a structure dependent intensity distribution of the radiation scattered in different directions.
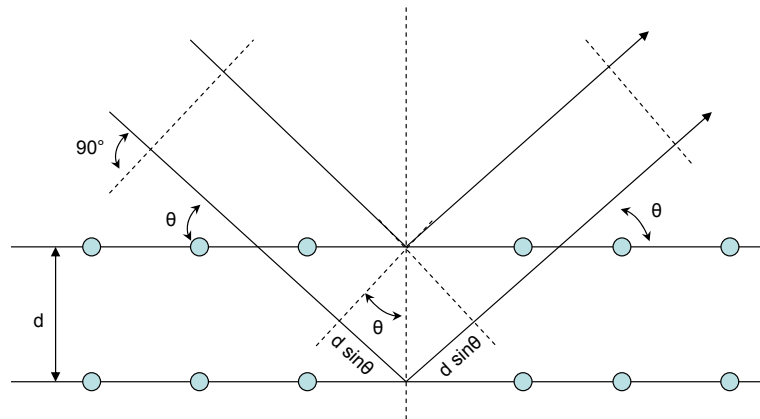


**Figure 4.4:** Description of Bragg's Law where d is the spacing of parallel atomic planes.

Basis for the x-ray diffraction methods was laid by W.L. Bragg. Considering a set of lattice planes which are distance $d$ apart and an incident beam lying in the plane of the paper (Figure 4.4). If the angle between the lattice plane and incident beam as well as scattered beam being $\theta$ and the path difference for the beams scattered from atoms lying in the adjacent planes is $2dsin\theta$; Bragg's law states that scattered beams by different crystal planes in a stack characterized by the inter-planar distance $d$ will interfere constructively, i.e. will be in-phase if the path difference is a integral number of wavelengths.

$$2dsin\theta = n\lambda \tag{4.17}$$

Note that, this situation only holds when $\lambda \leq 2d$. [134] If $\theta$ is small ($\theta \leq 5°$; Small angle x-ray scattering, SAXS), mesoscopic spacings $d$ are accessible (1nm to 100nm) while in case of large scattering angles $\theta > 5°$; Wide angle x-ray scattering, WAXS) smaller inter planar distances $d$ are detected (Å range).
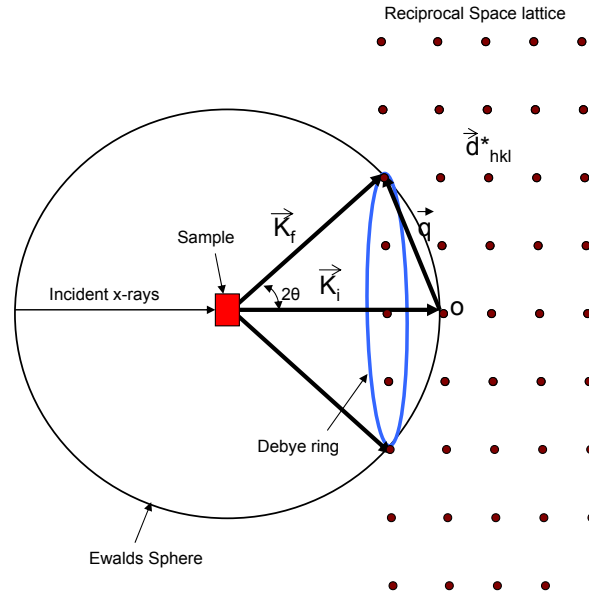


**Figure 4.5:** Ewald's sphere and reciprocal lattice.

Generalizing the situation, one has to consider the Ewald's sphere and vectors as shown in Figure 4.5. Here, sample is illuminated by incident beam of monochromatic x-rays with the wavelength $\lambda$ having a certain intensity $I_0$. $\vec{K}_i$ and $\vec{K}_f$ are the wave vectors describing the incident and scattered beams respectively. Scattering vectors $\vec{q}$ can be expressed as

$$\vec{q} = \vec{K}_f - \vec{K}_i \tag{4.18}$$

where $|\vec{K}_i| = |\vec{K}_f| = 2\pi/\lambda$ assuming elastic scattering. [118] Scattering vector $\vec{q}$ is also related to the scattering angle $\theta$ according to

$$|\vec{q}| = (4\pi/\lambda)sin\theta \tag{4.19}$$

Accordingly Bragg's law can be also written as $d = 2\pi/|\vec{q}|$. More sophisticated situation in the general case is sketched in Figure 4.5. Here, the vectorial character of $\vec{q}$ and the directions of the lattice planes in 3D space have to be considered. This requires a generalized description of the 3D periodic lattice.

***Reciprocal lattice and Ewald's Sphere***: A crystal lattice in the real space can defined based on a unit cell having unit cell vectors as $\vec{a}$, $\vec{b}$ and $\vec{c}$. Each edge of the unit cell gives then the next lattice point and this continues in all directions periodically. In the reciprocal space, the lattice is given by the reciprocal space vectors $\vec{a}^*$, $\vec{b}^*$ and $\vec{c}^*$. Points in reciprocal space do also repeat at periodic intervals defining the reciprocal lattice, which is the Fourier transform of the real space lattice. The relationship between the reciprocal lattice vectors and unit cell vectors in real space is given by

$$\vec{a}^* = \frac{1}{V_u}(\vec{b} \times \vec{c}) \tag{4.20}$$

$$\vec{b}^* = \frac{1}{V_u}(\vec{c} \times \vec{a}) \tag{4.21}$$

$$\vec{c}^* = \frac{1}{V_u}(\vec{a} \times \vec{b}) \tag{4.22}$$

where $V_u$ is the volume of the unit cell expressed as

$$V_u = \vec{a}(\vec{b} \times \vec{c}) = \vec{b}(\vec{c} \times \vec{a}) = \vec{c}(\vec{a} \times \vec{b}) \tag{4.23}$$

Any vector in reciprocal lattice represents one set of lattice planes in real space and can be expressed as

$$\vec{d}^*_{hkl} = h\vec{a}^* + k\vec{b}^* + l\vec{c}^* \tag{4.24}$$

where (hkl) are the Miller indices describing one set of planes. Important characteristics of the reciprocal lattice is that $\vec{d}^*_{hkl}$ is normal to the crystallographic planes whose Miller indices are (hkl) and $|\vec{d}^*_{hkl}|$ is reciprocal of interlamellar spacings $d_{hkl}$ between neighbored (hkl) lattice planes. [135, 136]

The generalized version of Bragg's law (equation 4.17) for the 3D case is the Laue condition

$$\frac{\vec{q}}{2\pi} = \vec{d}^*_{hkl} \tag{4.25}$$

Under this condition constructive interference will occur in the general case. This condition can be visualized constructing Ewald's sphere which is an imaginary sphere with the radius of $(2\pi/\lambda)$ drawn passing through the origin O of the reciprocal lattice (Figure 4.5). The crystal (sample) lies in the center of the sphere and beam enters from the left. Rotation of the crystals also rotates the corresponding reciprocal lattice . During the rotation, reciprocal

lattice points touch the sphere. This is the position where the Laue condition is satisfied and diffraction will be observed due to equivalence of scattering vector $\vec{q}$ and reciprocal space vector $\vec{d}^*_{hkl}$.

Considering one characteristic set of lattice planes represented by the Miller indices (hkl), the scattered beams will only produce a reflection, if $\vec{d}^*_{hkl}$ lies on the Ewald's sphere. In case of a powder or a polycrystalline sample with random orientation of small crystallites, the direction where (hkl) planes can constructively interfere lie on an annulus ring which is known as Debye ring as shown in Figure 4.5. Debye rings could also be defined as intersection of reciprocal lattice sphere for a certain set of lattice planes given by one $\vec{d}^*_{hkl}$ vector with the Ewald's sphere. For an isotropic sample, complete rings are obtained while in case of anisotropic samples, only spots are seen instead of the annular rings since many orientations of $\vec{d}^*_{hkl}$ do not occur.

***Instrument used.*** In this work, small angle instrument assembled by JJ X-rays based on a 2D detector (Bruker HI star) and a Rigaku rotating anode with focusing optics is used. It is fitted with a Linkam hot stage temperature controller for temperature dependent measurements. The measurements were performed under vacuum using CuK$\alpha$ radiation with a wavelength $\lambda = 1.54$Å. The instrument was calibrated using silver behenate as reference material. Wide angle x-ray scattering measurements were performed on SIEMENS D5000 powder diffractometer with germanium monochromator using CuK$\alpha$ radiation. Height calibration was performed considering the first order diffraction peak obtained from the measurements on the 2D detector. The samples were pressed significantly above $T_g$ and melting temperature $T_m$ under hot press to form isotropic samples. As received samples are also isotropic in nature.

## 4.2   Materials

In this section, the microstructure of regio-regular and regio-random poly(3-alkyl thiophenes-2,5-diyl) is discussed along with the brief description about the synthesis routes. Crystallographic models for regio-regular systems as reported in the literature are discussed. The two sample series used in this work are characterized.

### 4.2.1   Regio-regular and regio-random poly(3-alkyl thiophenes)

Polythiophenes belong to the class of conjugated polymers which are often used materials in organic electronics due to high conductivity as well as temperature stability. [137] Major

disadvantage of polythiophenes is lack of processibility which is overcome by adding n-alkyl groups to the thiophene rings. Poly(3-alkyl thiophenes) [P3AT] are soluble in common solvents as well as processable. [34] Poly(3-alkyl thiophenes) can be classified based on their microstructure, in particular according to the head to tail arrangement of the thiophene rings along the backbone, as (a) regio-regular P3ATs having a very high HT-HT content and (b) regio-random P3ATs where all linkages HT-HT, HT-HH, TT-HT and TT-HH as shown in figure 4.6 appears with the same probability. Different regioregularities occur due to the fact that monomeric units are not symmetric and attachment via 2 (head) and 5 (tail) positions results in different situations. Differences regarding the HT arrangement have far reaching consequences for the properties of P3ATs. The thiophene rings of regio-regular P3ATs can crystallize which is not the case in regio-random P3ATs. Hence, efficient charge transport is realized in regio-regular P3ATs due to packing of thiophene rings on a well defined crystal lattice supporting planarity and $\pi$-$\pi$ orbital overlap which is disturbed in regio-random samples.



Head-to-Tail-Head-to-Tail
Sequence (HT-HT)

Tail-to-Tail-Head-to-Tail
Sequence (TT-HT)

Head-to-Tail-Head-to-Head
Sequence (HT-HH)

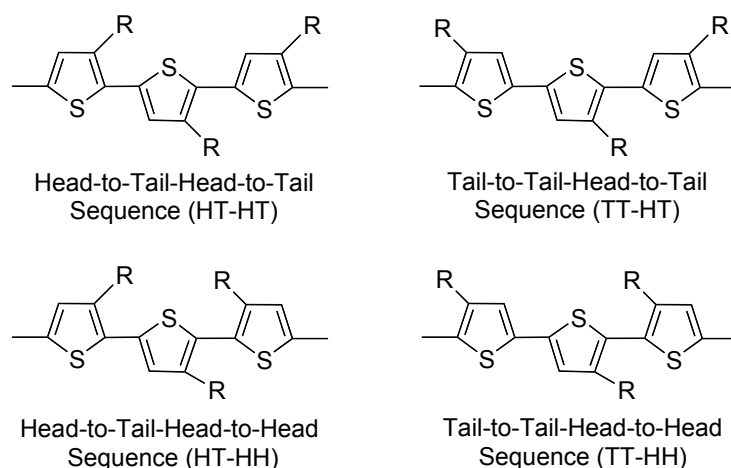Tail-to-Tail-Head-to-Head
Sequence (TT-HH)

**Figure 4.6:** Schematic representation of possible head-tail arrangements in poly(3-alkyl Thiophenes).

### 4.2.2   Synthesis of poly(3-alkyl thiophenes)

Poly(3-alkyl thiophenes) was first synthesized by Elsenbaumer in 1980s via metal catalyzed cross-coupling polymerization. P3ATs were synthesized by treating 2,5 diiodo 3-alkyl thiophenes with Mg using THF as solvent and $Ni(dppp)Cl_2$ as a catalyst. Molecular weights of polymers synthesized by this method was in the range 3-8kg/mol with a polydispersity index of 2. [138, 139] Another method of polymerization is based on oxidative polymerization with $FeCl_3$ in chloroform as a solvent. Molecular weights obtained are in the range

11-80kg/mol with a polydispersity index lying in the range 4-10. [140] In both the methods the regio-regularity achieved are of the order of 65%, as there is no regio-chemical control in the reaction.

Two polymerization methods giving high HT-HT contents are (a) McCullough method and (b) Rieke method as described.

(a) *McCullough Method*: 2-bromo-5-(bromomagnesio)-3-alkyl thiophenes are polymerized using $Ni(dppp)Cl_2$ yielding 98-100% HT-HT couplings. Molecular weights produced by this method lies in the range 20-40kg/mol with a polydispersity index of about 1.4. [34, 141]

(b) *Rieke Method*: 2,5-dibromo-3-alkylthiophenes are polymerized using Rieke zinc in presence of the catalyst $Ni(dppe)Cl_2$ to get regio-regular HT-HT coupling while presence of $Pd(PPh_3)_4$ yields regio-random P3ATs. Molecular weights obtained by this method is around 30kg/mol with a polydispersity index of 1.4. This method gives regio-regular samples containing >97%(HT-HT) and controlled regio-random samples with (HT-HT):(HT-HH):(TT-HT):(TT-HH) ratio of 1:1:1:1. [142]

**Table 4.1:** Physical characterization of P3ATs.

| Label | $M_n{}^{\dagger}$ (kg/mol) | $M_w/M_n{}^{\dagger}$ | $M_n{}^{\ddagger}$ (kg/mol) | $M_w/M_n{}^{\ddagger}$ |
|-------|------|------|------|------|
| P3BT | 13.21 | 2.47 | 11.20 | 1.71 |
| P3HT | 31.5 | 2.64 | 12.35 | 2.10 |
| P3OT | 19.3 | 2.99 | 24.3 | 1.62 |
| P3DT | 24.8 | 2.48 | 92.2 | 1.76 |
| P3DDT | 33.1 | 2.32 | 27.3 | 2.16 |

$^{\dagger}$ Regio-random P3ATs ; $^{\ddagger}$ Regio-regular P3ATs.

Samples used in this work are two series of regio-regular and regio-random poly(3-alkyl thiophenes-2,5-diyl) with different number of methylene units $C$ per side chains. Poly(3-butyl thiophene) [$C = 4$, P3BT]; poly(3-hexyl thiophene) [$C = 6$, P3HT]; poly(3-octyl thiophene) [$C = 8$, P3OT]; poly(3-decyl thiophene) [$C = 10$, P3DT] and poly(3-dodecyl thiophene) [$C = 12$, P3DDT] samples were purchased from Rieke Metals Inc. Synthesis of these samples were done on the basis of the Rieke method as described above. For regio-random P3ATs, four triads (HT-HT):(HT-HH):(TT-HT):(TT-HH) have equal probabilities (1:1:1:1) as determined by NMR and for regio-regular samples, (HT-HT) content is $\approx 97\%$. Molecular weights and polydispersities as obtained from gel permeation chromatography

measurements against polystyrene standards with THF as solvent are listed in Table 4.1. Note that this method gives usually too large molecular weights [143] since the microstructures of polystyrene and P3ATs are quite different. It is also shown by Yue et al. [144] using dynamic light scattering that extensive aggregation occurs in regio-regular samples. This might also contribute to the errors in determining the accurate molecular weights.

### 4.2.3   Morphology of regio-regular poly(3-alkyl thiophenes)

Brückner et al [145] analyzed neutral polythiophenes with Rietveld whole-fitting method. They have predicted the two dimensional structure orthogonal to the chain axis with pgg symmetry. This Herring bone-like structure is shown in Figure 4.7 and is predicted assuming co planarity of the thiophene rings. The unit cell parameters calculated are a= 7.79Å and b=5.53Å. Assuming an orthorhombic cell, unit cell vector in 'z' direction was calculated to be c=7.753Å. Based on density considerations, the number of thiophene rings per unit cell is 4.
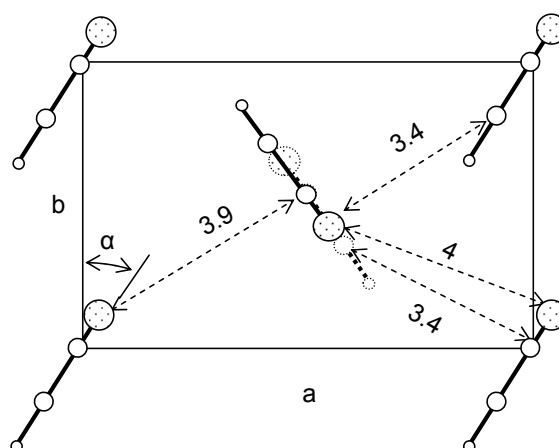


**Figure 4.7:** The two dimensional structure of polythiophene assuming rectangular geometry. Adapted from [145].

Attaching alkyl side chains to the thiophene rings increases solubility as well as fusibility while the main conducting $\pi$ conjugated regions also exists. However, this substitution process leads to strong structural changes and results in a different structure of the unit cells. [38] Kawai et al studied the complete series of regio-regular P3ATs focussing in particular on the structural changes due to an increase of the length of the side chains. Primitive orthorhombic unit cell was predicted for the complete series and a generalized scheme of packing of

P3ATs are reported as shown in Figure 4.8. [146] In this scheme, unit cell vector $a$ corre-
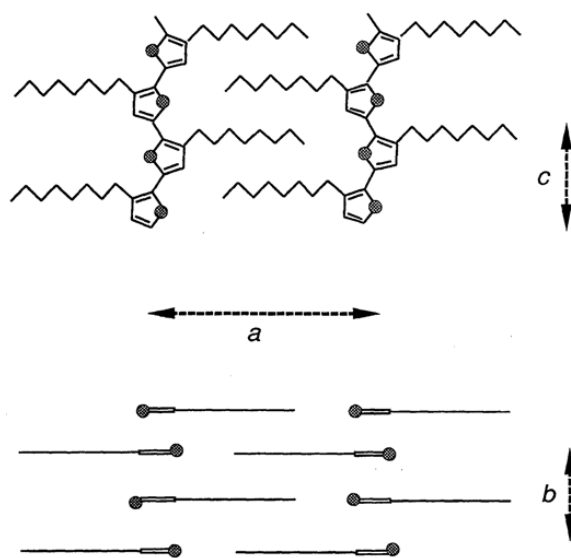


**Figure 4.8:** Crystal structure of P3ATs as proposed in Ref. [146]

sponds to inter main chain distances $(h00)$, $b$ corresponds to interlayer $\pi - \pi$ stacking $(0k0)$ and $c$ corresponds to inter side chain distances $(00l)$. All P3ATs exhibit stacked lamellar morphology which allows $\pi - \pi$ orbital overlap. There exists continuous alternating regions of side chain and main chain domains with a correlation lengths of about 250Å. [147] Typical dimensions of the unit cell are a= 12.7Å (for C=4) to 26.43Å (for C=12), b $\approx$ 7.5Å and c $\approx$ 7.77Å. [38, 146] As the unit cell vectors $b$ and $c$ are quite similar, a composite peak occurs with the dominance of (0k0) reflections. [148] It has also been reported that not all the thiophene units pack on the crystalline lattice. [149–153] Liquid crystallinity of the main chains in regio-regular P3DDT member has also been discussed. [154]

The state of the side chains in regio-regular P3ATs is controversially debated since this interesting class of materials has been discovered. Many groups have investigated the packing of the side chains in regio-regular P3ATs using surface methods like STM and SEM [149, 155], X-ray diffraction [36, 38, 47, 156–158], calorimetry [155, 158] etc. For lower members, situations ranging from fully amorphous to completely crystalline alkyl groups are considered. [46]

It is also often discussed whether the alkyl side chains are interdigitated or non-interdigitated, tilted or non-tilted, extended or disordered. Mainly four cases are reported in the litera-
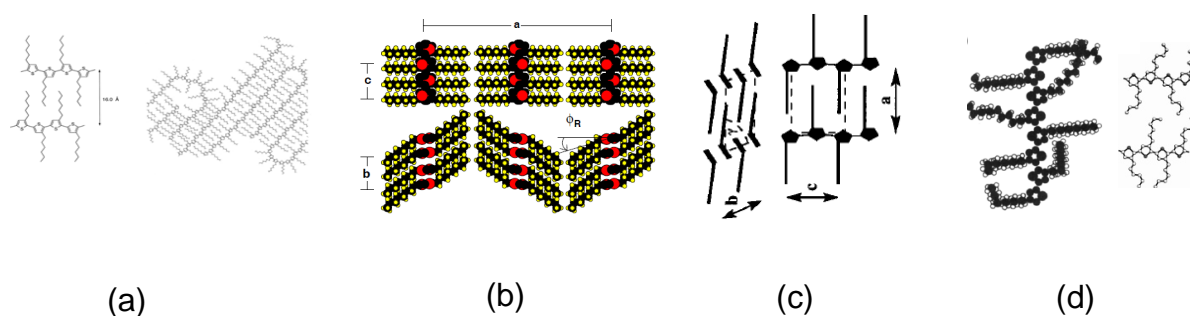
**Figure 4.9:** Structural models for regio-regular P3ATs considering different side chain packings i.e. (a) Interdigitated non-tilted side chains [149] (b) non-interdigitated tilted side chains [156] (c) Interdigitated tilted side chains [36] (d) liquid like disordered side chains. [147, 157]

ture as shown in Figure 4.9. Based on the results of surface methods interdigitated non-tilted side chains [149] were predicted (Figure 4.9a), while crystalline non-interdigitated tilted side chains were discussed based on scattering data by several groups (Figure 4.9b). [36, 152, 156, 158, 159] Non-interdigtated tilted side chain packings are discussed with models based on equating the areal density of polyethylene crystals with the areal density of alkyl side chains. [152] Transformations from interdigitated-tilted side chains (Figure 4.9c) to non-interdigitated tilted side chains are also reported. [36] Calorimetric measurements on regio-regular systems show two endothermal peaks. The main peak at high temperatures (between $150°$ and $250°C$) is commonly related to main chain melting while an additional peak which occurs sometimes around $60°C$ has been usually interpreted as melting of side chains. [154, 155] The appearance of disordered side chains (Figure 4.9d) has been also concluded based on broad peaks in the WAXS range indicating liquid -like packing of the side chains [38] and by areal density calculations. [157] Recent studies on a series of highly regio-regular statistical P3AT copolymers composed of 3-butyl thiophene and 3-octyl thiophene monomers with different side chain length show a smooth change of inter main chain distances ($d_{100}$) corresponding to $a$ in Figure 4.8 with composition which also indicates amorphicity of the side chains. [160] The large variety of discussed models shows that the state of the side chains is controversially debated and situations from fully amorphous to completely crystalline are considered. New results clarifying the situation are obviously required.

# Chapter 5

# Morphology and characterization

In this chapter, results of the basic characterization of two series of regio-regular [rreg] and regio-random [rran] P3ATs by differential scanning calorimetry (DSC), intermediate and wide angle x-ray scattering (WAXS) are presented.

## 5.1   Thermal analysis

**Differential Scanning Calorimetry**

DSC measurements performed on Perkin Elmer DSC7 instruments are shown in this section. Samples with a mass of about 5mg were encapsulated in hermetically sealed $30\mu l$ pans under the controlled nitrogen atmosphere. Before the heating scans, the samples have been differently treated to remove the thermal history as described.

***Regio-random poly(3-alkyl thiophenes)***. DSC heating scans for regio-random P3ATs, performed after removing the thermal history of as received samples by annealing at 150°C for 5 minutes are presented in Figure 5.1. Heating scans (+20K/min) show that a thermal glass transition occurs for all samples indicated by a prominent step in $C_p(T)$. Glass temperature $T_g$, obtained from an equal area construction, decreases with increasing side chain length $C$. The $T_g$ shift is approximately 10K per additional CH$_2$ unit in the side chain (Table 5.1). For the P3DDT sample with $C = 12$ alkyl carbons per side chain, the glass temperature is hard to estimate based on the heating scans since additional contributions occur slightly above $T_g$. There are two small peaks in $C_p(T)$ for this sample which are reproducible even after quenching. This is a first indication for a small fraction of crystalline material in this sample containing long alkyl groups. No melting endotherms are present at higher temperatures ($> 75°C$) for all members of this series showing the amorphicity of the thiophene
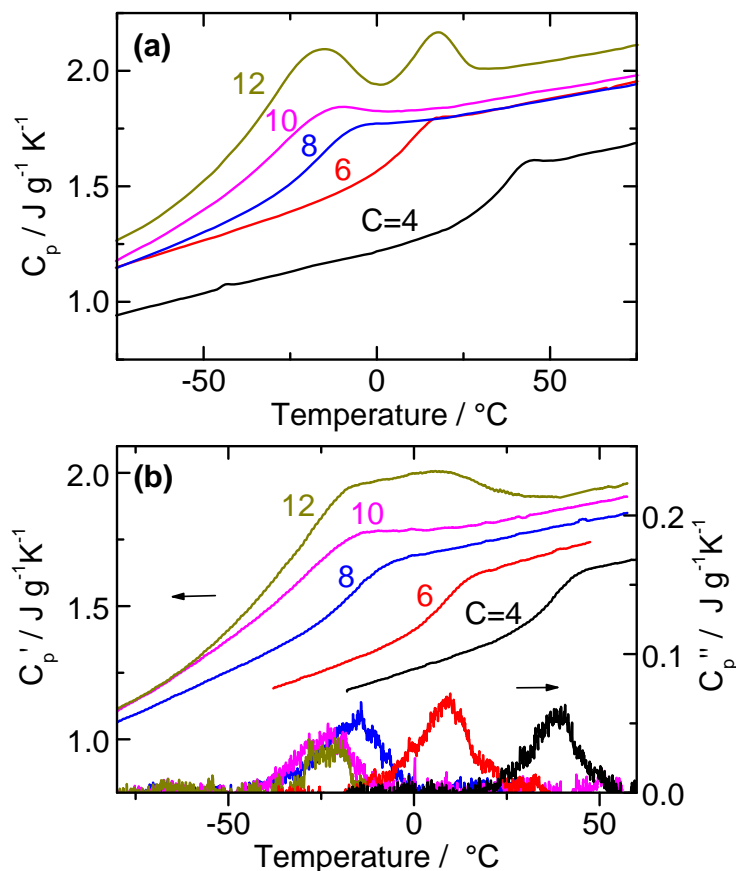
backbones.



**Figure 5.1:** (a) DSC heating scans (d$T$/d$t$= +20K/min) and (b) TMDSC data ($t_p = 60$s, underlying scan rate d$T$/d$t$= +4K/min) for a series of regio-random P3ATs. The labels indicate the $C$ number.

The TMDSC results presented in Figure 5.1b show real and imaginary parts of the dynamic heat capacity $C_p^*(T) = C_p' - iC_p''$ for regio-random P3ATs. In the real part, a step is seen while in the imaginary part correspondingly a peak is observed. Dynamic glass temperatures $T_\alpha$ are determined by fitting the peaks in the imaginary part, which indicate the $\alpha$ relaxation process, using a Gaussian function (Table 5.1). For all the samples, the dynamic glass transition shifts to lower temperatures with the increasing side chain lengths and tends to saturate for higher members which is due to the internal plasticization phenomenon as discussed by Heijboer. [161] The peaks in $C_p''(T)$ for P3DT and P3DDT seems to be asymmetrical, probably due to superposition of an $\alpha$ peak corresponding to the glass transition of the thiophene backbones with weak contributions originating from a polyethylene-like glass transition ($\alpha_{PE}$) related to the side chains motions as observed in shear data (section 6.1) and in other side chain polymers. [162] Additional features at temperatures above the $\alpha$ relaxation step are seen in

the real parts $C_p'$ for P3DT ($C = 10$) and P3DDT ($C = 12$). This shows that the peaks in the DSC scans are not simply overshoots resulting from non-equilibrium effects in glass-forming materials, as in TMDSC such contributions should not be seen. Interestingly, the results indicate that there are two weak melting peaks in P3DDT which include reversible contributions detectable by TMDSC. Such reversible contributions in the melting region of polymers are regularly reported.
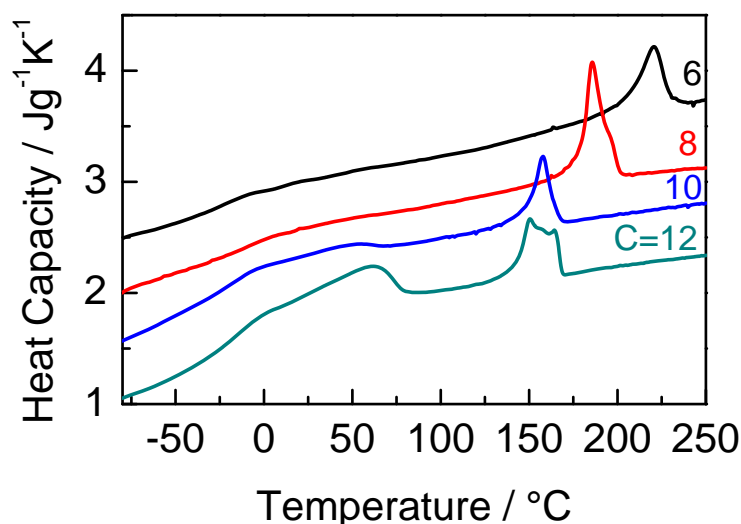


**Figure 5.2:** DSC heating scans (d$T$/d$t$= +20K/min) for a series of regio-regular P3ATs. The labels indicate the $C$ number. Curves are vertically shifted by 0.5J/gK for the sake of clarity.

***Regio-regular poly(3-alkyl thiophenes)***. DSC heating scans for regio-regular P3ATs, performed after removing the thermal history of as received samples by annealing above the melting point for 5 minutes are presented in Figure 5.2. Heating scans (+20K/min) show in all the cases a prominent melting endotherm in the range from $125°C - 225°C$ in $c_p(T)$ curves (Table 5.1). This is indicating the melting of crystalline thiophene main chains. The melting temperature decreases with increasing side chain lengths in accordance with literature results. $\Delta H_m$ values lies in the range from 9-17 J/g. However, it is hard to predict the degree of crystallinity due to unavailability of serious information about the heat of melting of 100% crystalline thiophene units. Note that the melting peak for regio-regular P3DDT shows an internal structure. This may indicate the existence of different polymorphic states as discussed later in chapter 7. As all regio-regular samples are semicrystalline, it is very difficult to analyse the broad step like feature indicating the glass transition of the amorphous fraction at low temperatures of about $-25°C$. The position of the glass transition seems to be similar to that of regio-random samples. For P3DT and P3DDT sample, a bump like fea-

**Table 5.1:** Sample characterization for regio-random P3ATs

| Label | $C$ | $T_g$(DSC) $^oC$ | $T_\alpha$(TMDSC) $^oC$ | $d_{nps}$ Å |
|-------|-----|---------|-----------|-------|
| rran P3BT | 4 | 34 | 36 | - |
| rran P3HT | 6 | 4 | 9 | 16 |
| rran P3OT | 8 | -22 | -15 | 20 |
| rran P3DT | 10 | -33±3 | -29 | 21 |
| rran P3DDT | 12 | - | -31 | 24 |

ture appears at around $60°C$ like observed in their regio-random counterparts which is most likely due to the melting of small fraction of side chain crystals as discussed in section 9.3.

## 5.2  Structural analysis

X-ray scattering measurements were performed on rotating anode for the intermediate $q$ range ($0.2$ Å$^{-1} \leq q \leq 0.6$ Å$^{-1}$) and wide angle x-ray range ($0.21$ Å$^{-1} \leq q \leq 1.8$ Å$^{-1}$) using SIEMENS D5000 powder diffractometer. As-received samples were molten and quenched in all cases and subsequently measured at room temperature. In some cases, as-received samples are measured for comparison.
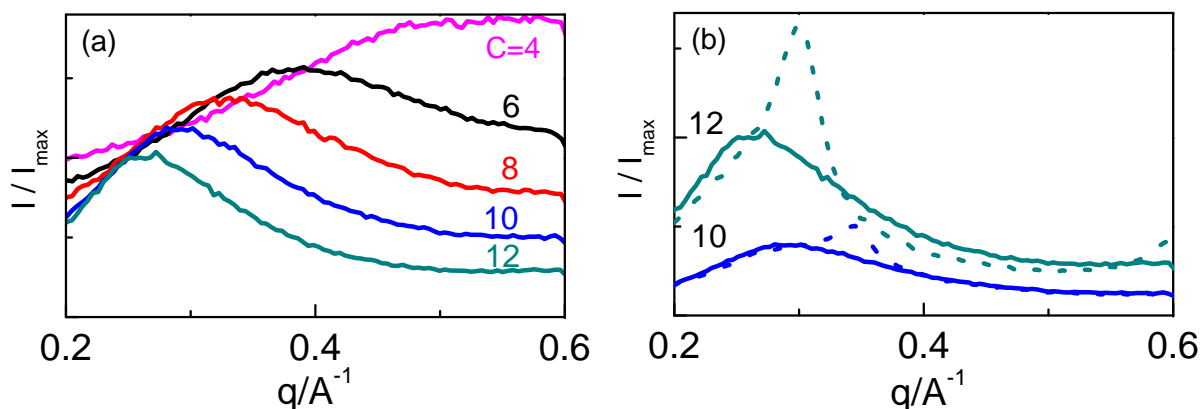


**Figure 5.3:** Intensity $vs.$ scattering vector $q$ for (a) series of regio-random P3ATs and (b) as received (dotted line) as well as quenched (solid line) for P3DT and P3DDT samples. Curves are vertically shifted for the sake of clarity.

***Regio-random poly(3-alkyl thiophenes)***. X-ray scattering data for the series of regio-random P3ATs are shown in Figure 5.3. A pre-peak in the range $0.2$ Å$^{-1} \leq q \leq 0.6$ Å$^{-1}$ is observed

for all samples with $6 \leq C \leq 12$ alkyl carbons indicating the existence of a characteristic length scale in the range of 10-30Å. The pre-peak sharpens slightly and shifts systematically to the lower scattering vectors $q$ with increasing number of methylene units in the alkyl side chains. For P3HT ($C = 6$), the maximum of the pre-peak is observed at approximately $q_{max} = 0.39$ Å$^{-1}$ while it appears at $q_{max} = 0.255$ Å$^{-1}$ for P3DDT ($C = 12$) in the amorphous state. According to Bragg's law $d = 2\pi/q_{max}$, this corresponds to equivalent Bragg spacings $d_{nps}$ in the range of 16 to 24.5Å. This pre-peak has been interpreted in similar systems as an indication for a nanophase separation of main and side chains [18] i.e. a strong tendency of the alkyl chains belonging to different monomeric units to aggregate and to form alkyl nanodomains. It should be noted that exception is P3BT (C=4) sample where a very broad smeared out pre-peak is observed indicating that this sample is probably not undergoing nanophase separation.

For as received P3DT and P3DDT samples ($C = 10, 12$) (Figure 5.3 b), the pre-peak looks significantly sharper indicating a better long range order of the corresponding structure. This behavior is well known from other semi-crystalline side chain polymers where the CH$_2$ units in the alkyl nanodomains are able to crystallize like in higher poly(n-alkyl methacrylates) with $C \geq 12$ methylene units. [53] Coherence lengths $d_S$ are about 50-80Å for amorphous samples and about 150Å for as received, semi-crystalline P3DDT estimated based on Scherrer's equation. According to Scherrer, the correlation length can be estimated using $d_c = K\lambda/(w \cdot cos\theta_{max})$ with $\lambda = 1.54$ Å being the wave length of Cu K$\alpha$ radiation, $K$ the Scherrer constant of about 1 and $\Delta(2\theta)$ the full width at half maximum height of a reflection observed at scattering angle $2\theta_{max}$. The appearance of higher orders to the pre-peak in semi-crystalline samples like P3DDT shows that a lamellar structure corresponding to staples of main chain and alkyl nanodomains exists in this sample. However, demixing effects leading to the formation of alkyl nanodomains with more irregular shape and boundaries seem to occur already in the amorphous state. The existence of higher order reflections to the pre-peak in semi-crystalline samples is a final proof for nanophase separation while the absence of it is no criterion for mixing.

The average main chain to main chain distances $d_{nps}$ for P3ATs and previously studied PnA-MAs [18, 25] are comparable as shown in Figure 5.4 (see also Table 5.1). In particular, the increase of $d_{nps}$ with $C$ is similar for both series. If compared with the all trans length of the alkyl chains, a nearly uniform offset seems to exist for all amorphous members. This finding is consistent with structural models assuming interdigitated side chains and main chain domains, which are responsible for the constant offset. Comparing the data for semi-crystalline
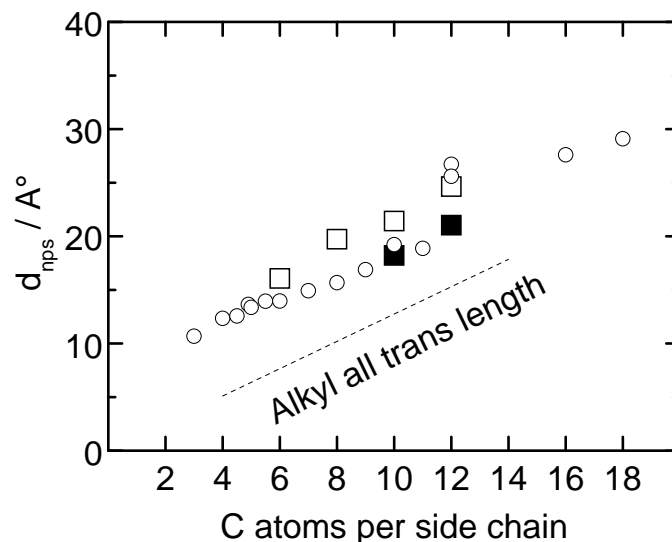
**Figure 5.4:** Equivalent Bragg spacings $d_{nps} = 2\pi/q_{max}$ as obtained from the pre-peak positions vs. number of carbon atoms per side chain $C$ (squares). Hollow squares denote amorphous and solid squares denote crystalline samples of regio-random P3ATs. Data for a series of atactic poly($n-$alkyl methacrylates) (small circles [18]) are given for comparison. The thin line indicates the slope, which is expected for extended (all trans) alkyl groups.

P3DT ($C = 10$) and P3DDT ($C = 12$) with their nearly amorphous counterparts one can conclude that $d_{nps}$ decreases slightly during crystallization. This behavior corresponds to the expected densification of the system during crystallization but is in contrast to the observation for crystallizable PnAMAs, where an opposite trend has been reported and interpreted as a consequence of an increasing trans content in the alkyl groups [51, 53] (see section 2.4).

***Regio-regular poly(3-alkyl thiophenes).*** Scattering experiments on regio-regular P3ATs with $6 \leq C \leq 12$ alkyl carbons per side chain in the intermediate $q$ range (0.2 Å$^{-1}$ $\leq q \leq$ 0.6 Å$^{-1}$) are performed to study the packing of main and side chains. The pattern for regio-regular P3ATs (Figure 5.5a) show expectedly (100) reflections as well as higher orders (200) in this $q$ range indicating a lamellar morphology formed by stacked thiophene and alkyl nanodomains. The (100) reflections shifts to lower scattering vectors $q$ with the increase in the side chain lengths indicating larger main chain to main distances ($d_{100} = 2\pi/q_{100}$) estimated to be in the range of 17 to 27 Å (Table 5.2). This is a clear confirmation for the nanophase separation of thiophene rings and alkyl nanodomains which is also indicated for fully amorphous regio-random P3ATs. The main chain to main chain distances are quite comparable in regio-regular and regio-random P3ATs (Figure 5.5b). The plot shows also a nearly linear increase of $d_{100}$ with the increase in the side chain lengths. The (100) reflections in
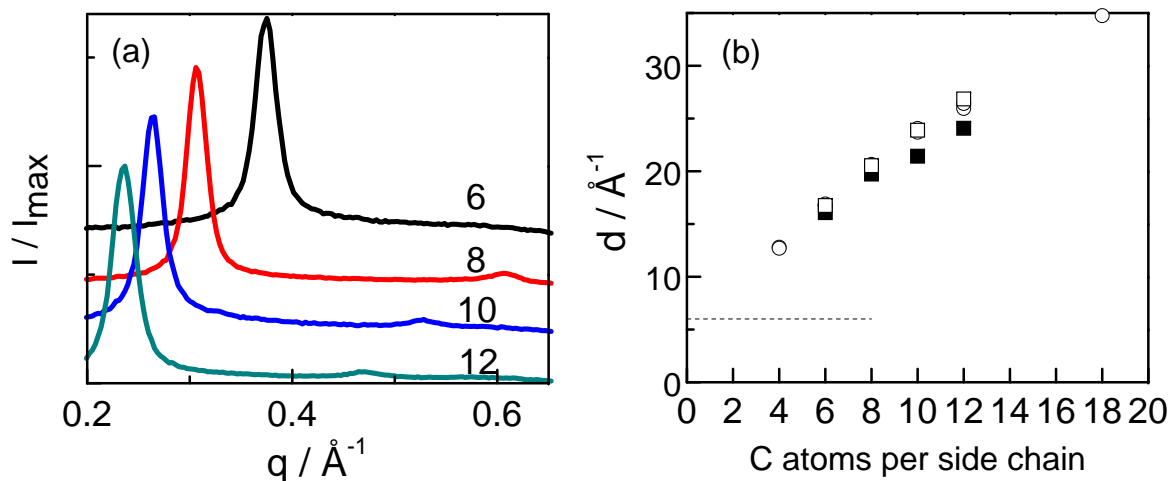
**Figure 5.5:** (a) Intensity $vs.$ scattering vector $q$ for a series of regio-regular P3ATs. Curves are vertically shifted for the sake of clarity. (b) Dependence of the interlayer-spacing $d_{100}$ on the number of alkyl carbons $C$ per side chain for and regio-regular (open squares) P3ATs. Additional data for the regio-regular P3ATs (circles) are taken from Ref. [38, 146] Main chain to main chain distances $d_{nps}$ from the pre-peaks for regio-random (solid squares) are shown for comparison.

regio-regular P3ATs are quite sharp and indicating long range order due to the presence of crystalline thiophene rings which is also observed in the DSC scans. The average correlation length related to the (100) reflections in our regio-regular P3ATs is $\approx$ 240-270 Å as estimated based on Scherrer's equation.
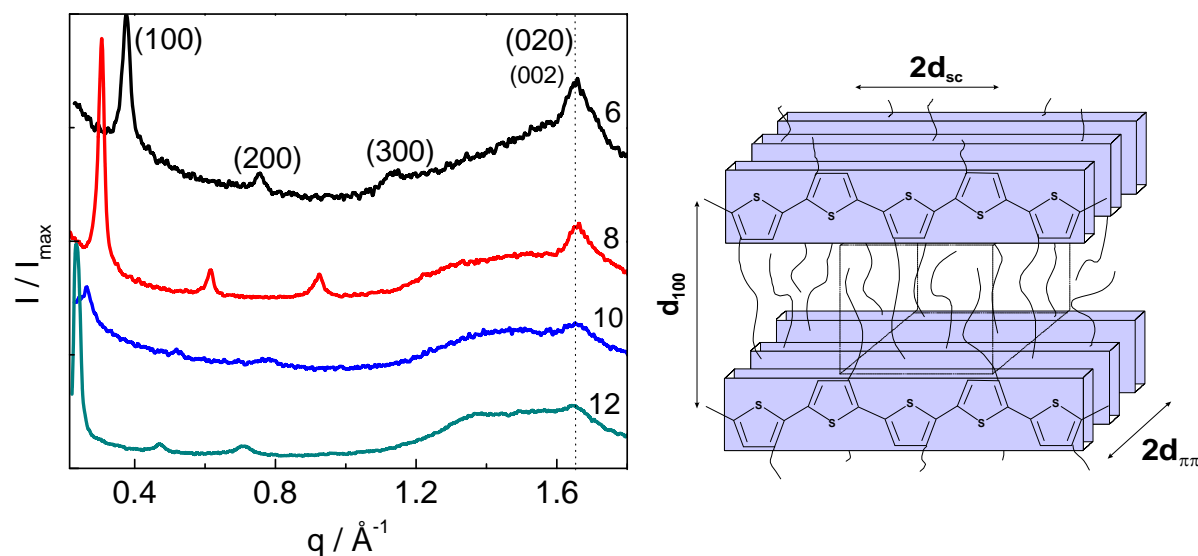


**Figure 5.6:** Intensity $vs.$ scattering vector q for a series of regio-regular P3ATs. Curves are vertically shifted for the sake of clarity. On r.h.s, schematic picture showing the packing of thiophene main chains and alkyl groups in regio-regular P3DDT where dotted lines indicate the unit cell used for volume calculations.

**Table 5.2:** Sample characterization for regio-regular samples

| Label | $C$ | $d_{100}$ Å | $d_{\pi\pi}$ Å | $d_{sc}$ Å | $V_{CH2}$ Å$^3$ |
|---|---|---|---|---|---|
| rreg P3HT | 6 | 17 | 3.80 | 3.88 | 26.45 |
| rreg P3OT | 8 | 21 | 3.79 | 3.88 | 26.77 |
| rreg P3DT | 10 | 24 | 3.80 | 3.88 | 26.45 |
| rreg P3DDT | 12 | 27 | 3.79 | 3.88 | 25.62 |

Wide angle x-ray diffraction was performed on the complete series of regio-regular P3ATs to characterize the crystalline packing in more detail. In all the cases four peaks are observed corresponding to (100), (200), (300) and a composite peak corresponding to (020) and (002) like discussed in chapter 4 (section 4.2.3). Consistent with the intermediate range scattering results, the WAXS pattern show the shift of (100) peak to lower scattering vectors with increasing side chain lengths leading to larger main chain to main chain distances. Well pronounced higher order peaks in the series (200) and (300) confirm lamellar packing of main and side chains on the mesoscale along with well defined interfaces between the domains and larger correlation lengths. The (020) reflection corresponds to $\pi - \pi$ stacking ($d_{\pi\pi}$) of the thiophene rings and (002) corresponds to the side chain to side chain distances along the main chains ($d_{sc}$) (Figure 5.6). Finding is that the crystalline thiophene rings show a $\pi - \pi$ stacking of about $d_{\pi\pi} = 3.80 \pm 0.01$ Å (Table 5.2) which is nearly independent on side chain lengths. The distance between the alkyl groups in main chain direction is quite similar ($d_{sc} = 3.88$ Å) (Table 5.2). Wide angle x-ray scattering pattern obtained at room temperature show basically only one common peak at 1.65 Å$^{-1}$ for the (020) and (002) reflections which is dominated by (020) contributions. [148] The broad underlying amorphous hallow seems to be also structured due to overlapping contributions from the alkyl nanodomains and amorphous thiophene backbones.

The structural data for regio-regular P3ATs in Table 5.2 can be also used to estimate the average volume per CH$_2$ unit $V_{CH2}$ for regio-regular P3ATs using a cell as shown in Figure 5.6. The volume of this cell depends on the average distance between two alkyl groups along the main chain $d_{sc}$, the average ring-to-ring distance $d_{\pi\pi}$ and the thickness of the alkyl nanodomain $d_{(a)} \approx (d_{(100)} - 6)$Å. 6Å seems to be a good estimate for the average thickness of the main chain layers in our nanophase separated samples and a suitable approximation for regio-regular as well as regio-random P3ATs which is calculated based on a linear extrapolation of $d_{100}$(C) to C=0 (Figure 5.5b) and also calculated from the dimensions of the thiophene rings. Both estimates are in good agreement. The average volume per $CH_2$ unit

can be calculated from

$$V_{CH2} = (d_{100} - 6\text{Å}) \cdot d_{sc} \cdot d_{\pi\pi}/C \tag{5.1}$$

with $C$ being the number of alkyl carbons per side chain. Note that the CH$_3$ end groups are treated like CH$_2$ units in this average. There are four alkyl stems in the plane, two point to the top and two point to the bottom. Further details of their arrangement are not considered here, since they are unimportant for the packing density. The $V_{CH2}$ values for regio-regular P3ATs are approximately 26.3±0.7Å$^3$ (Table 5.2) and are larger than those of crystalline polyethylene ($V_{CH2}^{PE}$ = 23.4Å$^3$) [118] and methylene units in crystalline lipids ($V_{CH2}^{lipid}$ = 24-25.5Å$^3$). [163] The average density of the alkyl nanodomains is obviously nearly constant and lower than that of polyethylene-like crystals as well as that of methylene sequences in crystalline lipids indicating high degree of amorphicity of the alkyl nanodomains. Further details are discussed in section 9.2.

Summarizing the results presented in this chapter, strong indications for nanophase separation exists for both the regio-random and regio-regular series as seen from the appearance of pre-peak and (100) reflections which both shift systematically to lower scattering vectors with the increasing side chain lengths corresponding to larger main chain to main chain distances. In case of regio-random P3ATs, main chains remain amorphous for the complete series. Side chain crystallization is indicated for P3DT and P3DDT member by appearance of melting peaks in expected temperature range in DSC scans. In regio-regular systems, main chains are packed in a crystalline lattice as shown by a melting endotherm as well as crystalline reflections in WAXS pattern. Indications for side chain crystalline regions exist in DSC scans for regio-regular P3DT and P3DDT samples. The glass transition in DSC scans for regio-random samples, shifts to lower temperatures with increasing side chain lengths showing internal plasticization. For regio-regular samples, a weak glass transition seems to appear at similar temperatures but is hard to analyze due to substantial crystallinity of the main chains.

# Chapter 6

# Relaxation dynamics of poly(3-alkyl thiophenes)

In this chapter, we will show the results of shear measurements on the series of regio-random thiophenes and regio-regular thiophenes where the thiophene rings act as disordered or ordered crystalline confinements for self assembled alkyl nanodomains respectively. Main aim is to study the dynamics within these alkyl nanodomains.

## 6.1 Dynamics of regio-random poly(3-alkyl thiophenes)

Dynamic mechanical measurements on our regio-random P3ATs series show a clear dependence of the relaxation behavior on the side chain length in isochrones measured at 10rad/s (Figure 6.1a). The $\alpha$ relaxation process in shear loss modulus $G''$ curves moves to lower and lower temperatures (Figure 6.1b) with increasing number of $CH_2$ groups in the side chains. The $\alpha$ peak appears at about 45°C for P3BT ($C = 4$) and approaches -18°C for nearly amorphous P3DDT ($C = 12$). The relaxation temperature as obtained from Gaussian fits to $G''(T)$ isochrones measured at 10 rad/s saturates for higher members of regio-random P3ATs. Corresponding behavior is seen for $T_g$ taken from the DSC scans (Figure 5.1). A similar shift of $\alpha$ relaxation process and DSC glass temperature $T_g$ has been reported for atactic PnAMAs. The relevant data are shown for comparison in Figure 6.1b. The shift of the $\alpha$ relaxation process in the PnAMA series has been related by Heijboer in the 1960s [161] to an 'internal plasticization' of the main chains by the highly mobile alkyl groups in the environment. The most interesting feature in the shear curves for regio-random P3ATs with $C \geq 6$ is that an additional relaxation process ($\alpha_{PE}$) appears at temperatures below the conventional $\alpha$ relaxation. This process occurs in the same temperature frequency range
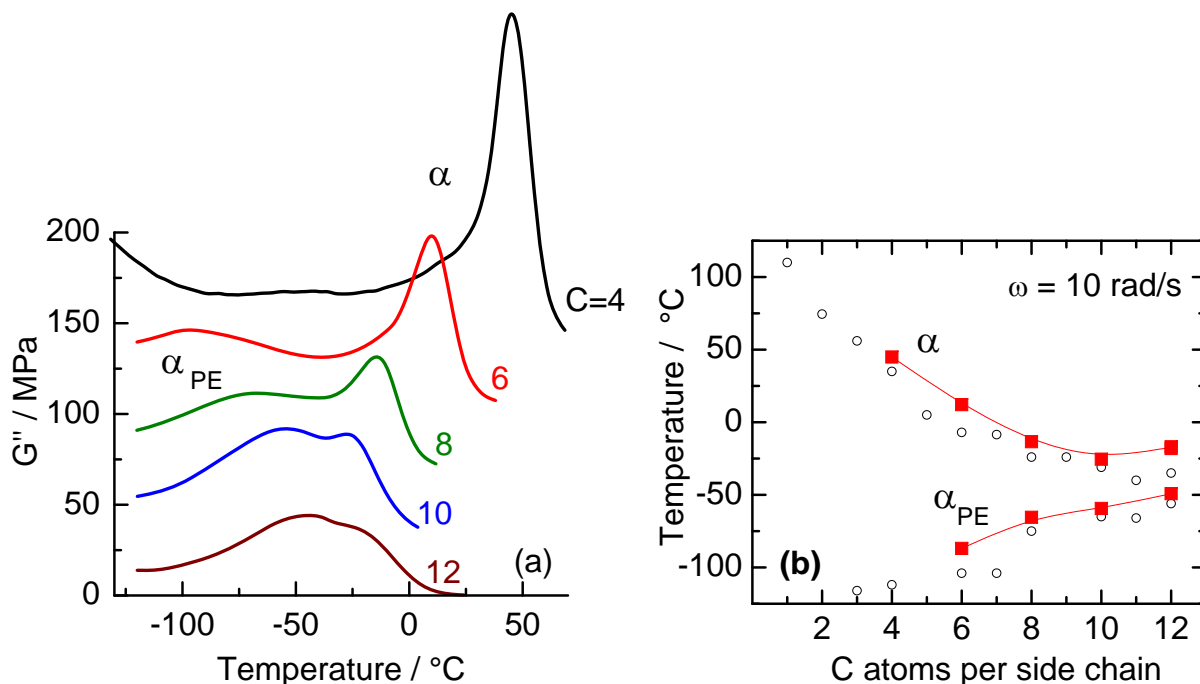
**Figure 6.1:** (a) Shear loss modulus $G''$ vs. temperature for regio-random P3ATs measured at a frequency of 10rad/s. The curves are vertically shifted for reasons of clarity. (b) Relaxation temperatures $vs.$ $C$ number for regio-random P3ATs (full squares). Peak maxima are taken from isochronal shear curves $G''(T)$ measured at 10rad/s by fitting the data using Gaussian functions. Data for previously measured PnAMA are shown for comparison (open circles [25]).

where the 'polyethylene-like glass transition' $\alpha_{PE}$ has been reported for PnAMAs and other polymer series with long alkyl groups in the side chain. [18] The $\alpha_{PE}$ process shifts systematically to higher temperatures with increasing number of methylene units per side chain and becomes stronger compared to the intensity of the conventional $\alpha$ relaxation peak. In case of atactic PnAMAs, it has been shown that the $\alpha_{PE}$ process in members with $C > 6$ is related to cooperative motions of the $CH_2$ units in small alkyl nanodomains. Thus, this relaxation process has been interpreted as 'polyethylene like glass transition' $\alpha_{PE}$. For PnBMAs with $C = 4$, the $\alpha_{PE}$ process seems to be more a Johari-Goldstein-like [68] secondary relaxation $\beta_{PE}$ with Arrhenius-like temperature dependence incorporating $CH_2$ units in the alkyl nanodomains. [164] The appearance of similar relaxation processes in amorphous regio-random P3ATs fits to the recent observation that the frequency temperature position of the $\alpha_{PE}$ process in nanophase-separated side chain polymers is practically independent on microstructure and softening behavior of the main chains. [18] The reported shear data for P3ATs support the idea that the tendency of main and side chain parts to separate is a general phenomenon in comb-like polymers containing long alkyl groups. Note that there is no clear

evidence for an $\alpha_{PE}$ process in P3BT. In the light of this fact and the occurrence of a broad pre-peak in the scattering data for P3BT (Figure 5.3), it seems to be open whether or not P3ATs with very short alkyl groups ($C \leq 4$) are really nanophase separated. An additional, tiny $\beta$ process is indicated in the shear curve for P3BT ($C = 4$) at about -45°C which is not seen for all higher P3ATs (Figure 6.1a). It is hard to get further information about the existence of this process in the higher members based on relaxation spectroscopy data since strong contributions related to $\alpha$ and $\alpha_{PE}$ occur in the same frequency temperature range. One may speculate that the $\beta$ process is hidden due to an overlap with the two prominent relaxation processes ($\alpha$ and $\alpha_{PE}$) in these samples.
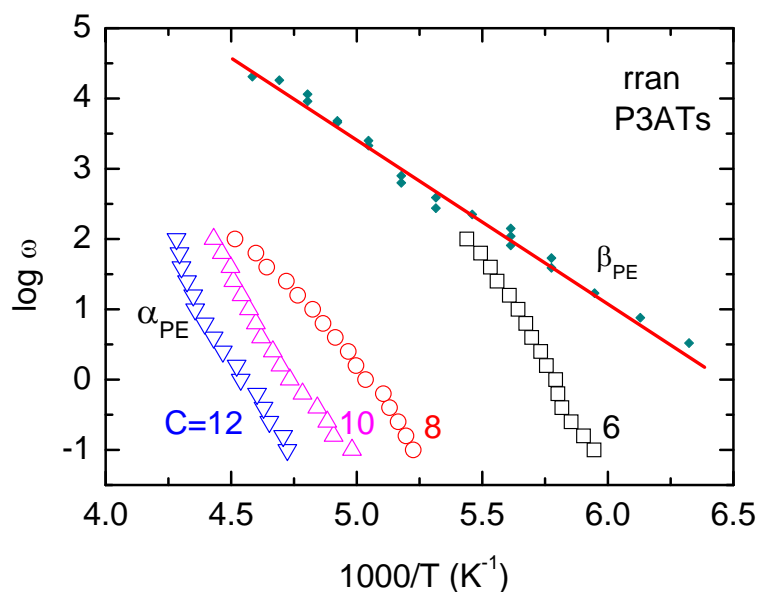


**Figure 6.2:** Arrhenius plot $\log\omega$ $vs$ 1000/T for regio-random P3HT (black), P3OT (red), P3DT (magenta) and P3DDT (blue). Hollow symbol corresponds to $\alpha_{PE}$ process take from the isochrones measured at different temperatures. Data for the $\beta_{PE}$ process in PnAAs (diamonds) with short side chains (C=4 and 5) are taken from Ref. [18] for comparison.

**Table 6.1:** Characteristic parameters for regio-random P3ATs

| Label | $T_\alpha{}^\dagger$ (°C) | $T_{\alpha,PE}{}^\dagger$ (°C) | $B$ (K) | $T_V$ (°C) | $m_{\alpha,PE}{}^\dagger$ |
|---|---|---|---|---|---|
| rran P3HT | 12 | -90 | 1025 | -83 | 30 |
| rran P3OT | -13 | -65 | 959 | -99 | 19 |
| rran P3DT | -25 | -59 | 878 | -108 | 32 |
| rran P3DDT | -18 | -49 | – | – | 49 |

$^\dagger$ Measurement frequency $\omega = 10$ rad/s.

An Arrhenius plot $\log\omega$ $vs$ 1000/T, showing the frequency-temperature dependencies of the

$\alpha_{PE}$ processes for different members of the series of regio-random P3ATs is shown in Figure 6.2. Steepness indices for the $\alpha_{PE}$ process calculated according to the equation [165]

$$m_{\alpha_{PE}} = -\mathrm{dlog}\omega/\mathrm{d}(T_{\alpha_{PE},10rad/s}/T)|_{T=T\alpha_{PE},10rad/s} \tag{6.1}$$

show a significant scatter in the range $m_{\alpha_{PE}} \approx 19 - 49$ (Table 6.1) for the series consistent with that for relatively strong glasses. This observation is in qualitative agreement with previous findings for other nanophase separated side chain polymers. Steepness index is the measure of cooperativity and quantifies the deviation from the Arrhenius-like temperature dependency. Johari-Goldstein $\beta$ processes should have m values in the range 13-16. Apparent activation energies $E_{A,\alpha_{PE}}$ calculated based on equation 2.3 are in the range 35.2kJ/mol to 50.6kJ/mol with limiting frequency $\omega_0$ of about $10^{20}$-$10^{34}$ rad/s. For $\beta$ process shown in Figure 6.2, activation energy is 19kJ/mol and limiting frequency $\omega_{\beta,PE}$ is of the order of $10^{15}$rad/s. Based on these findings we conclude that $\alpha_{PE}$ process shows typical features of a dynamic glass transition and reflects cooperative motions in self assembled alkyl nanodomains with typical dimensions in the range 10-30Å formed by aggregated side chains.

In a next step, more detailed dynamic mechanical measurements are performed on regio-random P3ATs from the glassy state to the flow region. Figure 6.3 shows a set of representative isotherms for P3OT as an example. At the lowest temperatures ($T \leq$ -100$^o$C), the typical behavior of a glassy material with a storage modulus $G' > 1$ GPa and significantly lower values for the loss modulus $G''$ is observed. A slight decrease of $G'$ and a broad maximum in $G''$ in the isotherms around -70$^o$C indicate the presence of a low temperature relaxation process $\alpha_{PE}$ reflecting the dynamics within the alkyl nanodomains. The softening process related to the conventional $\alpha$ process is seen in the isotherms between -20 and 12$^o$C. Expectedly, the $\alpha$ relaxation peak in $G''$ shifts rapidly to lower frequencies if the temperature decreases and leaves the frequency window of our measurements near the glass temperature taken from conventional DSC scans ($T_g =$ -22$^o$C). The $\alpha$ relaxation is followed by a rubber plateau with a plateau modulus of about 0.3 MPa seen in the isotherms around 52°C before the storage modulus decreases further in the flow transition region at higher temperatures. Note that the typical slopes of an ideal Newtonian liquid are approached but not reached up to 116 $^o$C being the high temperature limit of our shear measurements. This might be due to the relatively broad molecular weight distribution of the sample but could be partly also related to the internal structure of our nanophase-separated systems. Master curves are constructed by shifting the isotherms horizontally along the log frequency axis assuming that the shape of the relaxation processes is temperature independent as predicted by the time
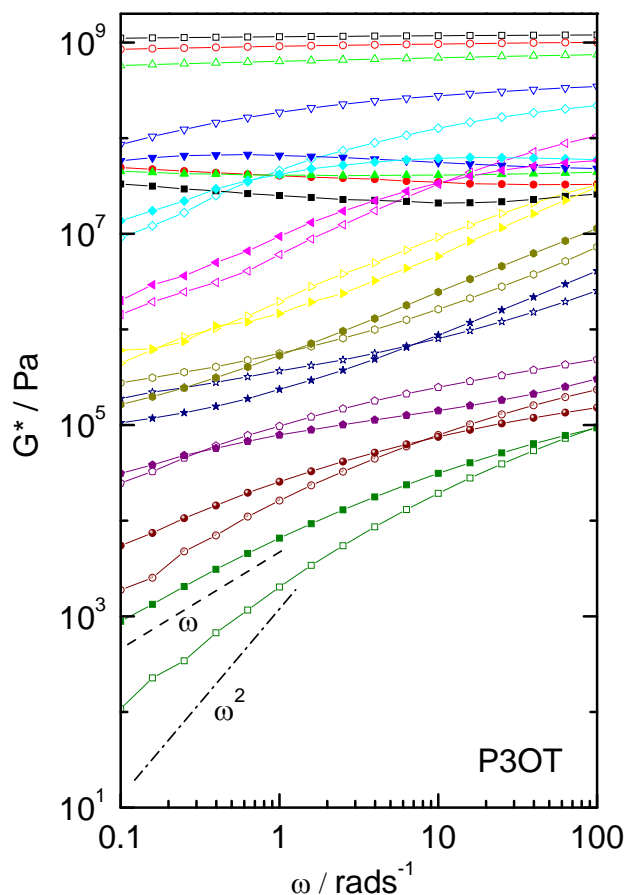
**Figure 6.3:** Shear storage modulus $G'$ (open symbols) and shear loss modulus $G''$ (full symbols) vs. angular frequency for regio-random P3OT measured at different temperatures (-120°C, squares; -90°C, circles; -60°C, triangles up; -20°C, triangles down; -12°C, diamonds; -4°C, triangles left; 4°C, triangles right; 12°C, hexagons; 20°C, stars; 52°C, pentagons; 84°C, spheres; 116°C, lower squares). The dashed lines indicate the slopes $G'' \propto \omega$ and $G' \propto \omega^2$ expected for a Newtonian liquid.

temperature superposition principle. This procedure neglects differences in the temperature dependence of the relaxation processes dominating in different temperature ranges but gives a useful overview of the relaxation spectrum of the investigated systems.

The master curves for different regio-random P3ATs in Figure 6.4 show consistently three relaxation processes which are already seen in the isotherms for P3OT: (i) the polyethylene like glass transition $\alpha_{PE}$ at high frequencies corresponding to the dynamics of $CH_2$ units within the alkyl nanodomains, (ii) the conventional $\alpha$ relaxation at lower frequencies related to the softening of the entire system and cooperative motions of a large number of monomeric units and (iii) the flow transition $ft$ corresponding to relaxational motions of complete chains indicating the transition from the rubber plateau to Newtonian flow. The
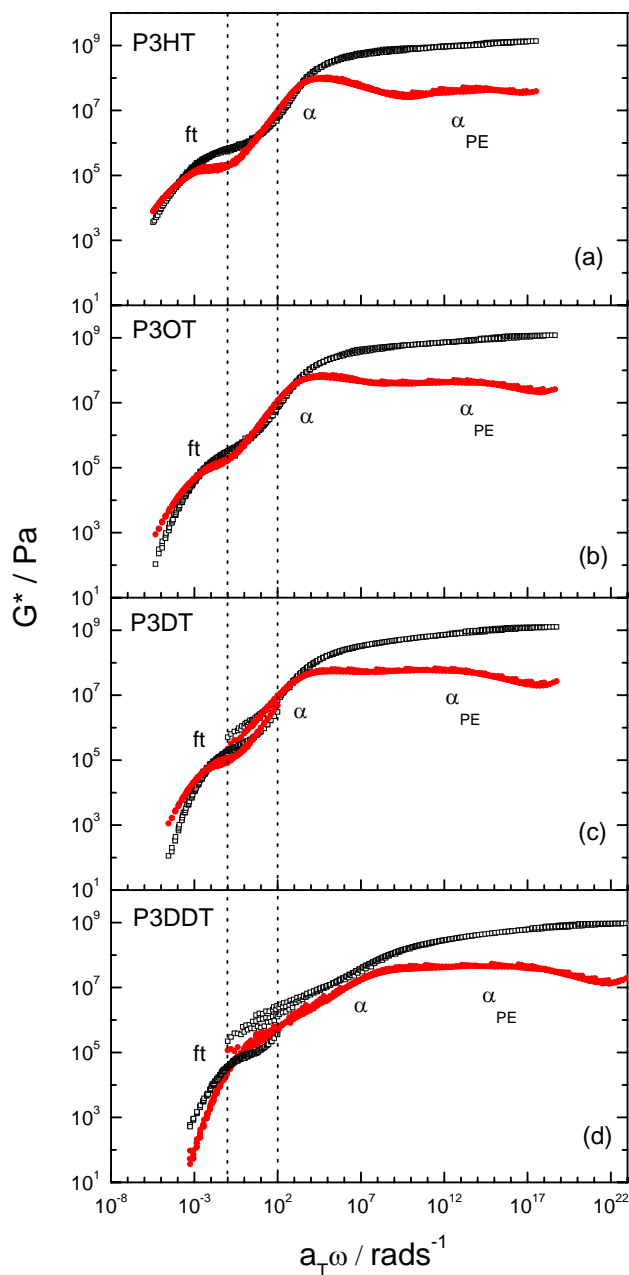
**Figure 6.4:** Master curves log G* $vs$ log $a_T\omega$ for a series of regio-random P3ATs. Storage modulus $G'$ (open symbols) and loss modulus $G''$ (solid symbols) for (a) P3HT with $T_{ref}$=38°C, (b) P3OT with $T_{ref}$=12°C, (c) P3DT with $T_{ref}$=4°C and (d) P3DDT with $T_{ref}$=24°C are shown. All isotherms above $T_{ref}$ are measured using parallel plates during step-wise heating starting at $T_{ref}$ and the isotherms below $T_{ref}$ are measured using stripes during step-wise heating starting at -120°C. The dashed lines indicate the frequency window of the measurements. Isotherms in the range 0.1 to 100rad/s with five points per decade are measured in the temperature range of $T$=-120°C to $T$=174°C. Soak time for each temperature was 600s. The temperature step was 4K in the $\alpha$ relaxation range, 10K significantly below and 8K above this region.

appearance of a pronounced rubber plateau between $\alpha$ relaxation and flow transition $ft$ for all investigated P3ATs shows clearly that their molecular weight is higher than the critical entanglement molecular weight $M_c$. For completely amorphous P3HT and P3OT samples, more or less smooth master curves are obtained although a certain scatter appears in specific ranges (Figures 6.4a and b). This scatter at large $a_T \omega$ values is basically due to the fact that the temperature dependence of $\alpha$ and $\alpha_{PE}$ processes is significantly different. The frequency gap between both processes changes with temperature and deviations appear in the master curves. Changes in the $\alpha_{PE}$ peak shape is another possible reason. The scatter in the range between $\alpha$ relaxation and flow transition ($ft$) is negligible for the amorphous samples since both processes have similar temperature dependencies. Certain differences in the temperature dependence of flow transition $ft$ and $\alpha$ relaxation with $T_{V(ft)} < T_{V(\alpha)}$ are reported based on detailed studies on polymers like PS and PVAC [166, 167] but have surely a negligible influence on the master curves shown here.

The master curves for regio-random P3DT and P3DDT (Figures 6.4c and d) show a similar sequence of relaxation processes but significant peculiarities near the reference temperature $T_{ref}$ slightly above $T_g$. The $G'$ and $G''$ isotherms measured using parallel plates after step-wise cooling the samples from higher temperature to the common $T_{ref}$ (l.h.s.) do not coincide with the data obtained by heating rapidly cooled stripes from low temperatures to $T_{ref}$ (r.h.s.). Thus, the master curve construction has been done for both data sets independently and a vertical gap appears between the two curves at $T_{ref}$. The reason for the obvious discrepancy in the modulus values at $T_{ref}$ is that the side chains in regio-random P3DDT and P3DT samples can crystallize. The alkyl groups are partly crystalline if the stripes have been heated from -120°C to $T_{ref}$ while the side chains can not crystallize if the samples are cooled down from high temperatures to $T_{ref}$ in the rheometer. Obviously, the different thermal history causes the gap in the moduli at $T_{ref}$ since slightly crystalline samples (r.h.s.) do have significantly higher storage moduli $G'$ in the rubber plateau region. This shows that shear measurements in the rubber plateau region are a sensitive tool to detect side chain crystallization in regio-random P3ATs. Important for an understanding of the shear data is the fact that stable crystalline forms of P3DDT melt above room temperature while crystallization appears basically below this temperature. The gap in the $G'$ master curves appears since stripes are quenched to -120°C before the measurements have been started, while all experiments using 8mm plates are performed above room temperature. In the latter case, the crystallinity is negligible since the sample has never been below room temperature where the crystallization process is most efficient (see Chapter 7). Hence the measurements on P3DDT in stripe ($T \leq T_{ref}$) and parallel plate geometry ($T \geq T_{ref}$) are performed on sam-
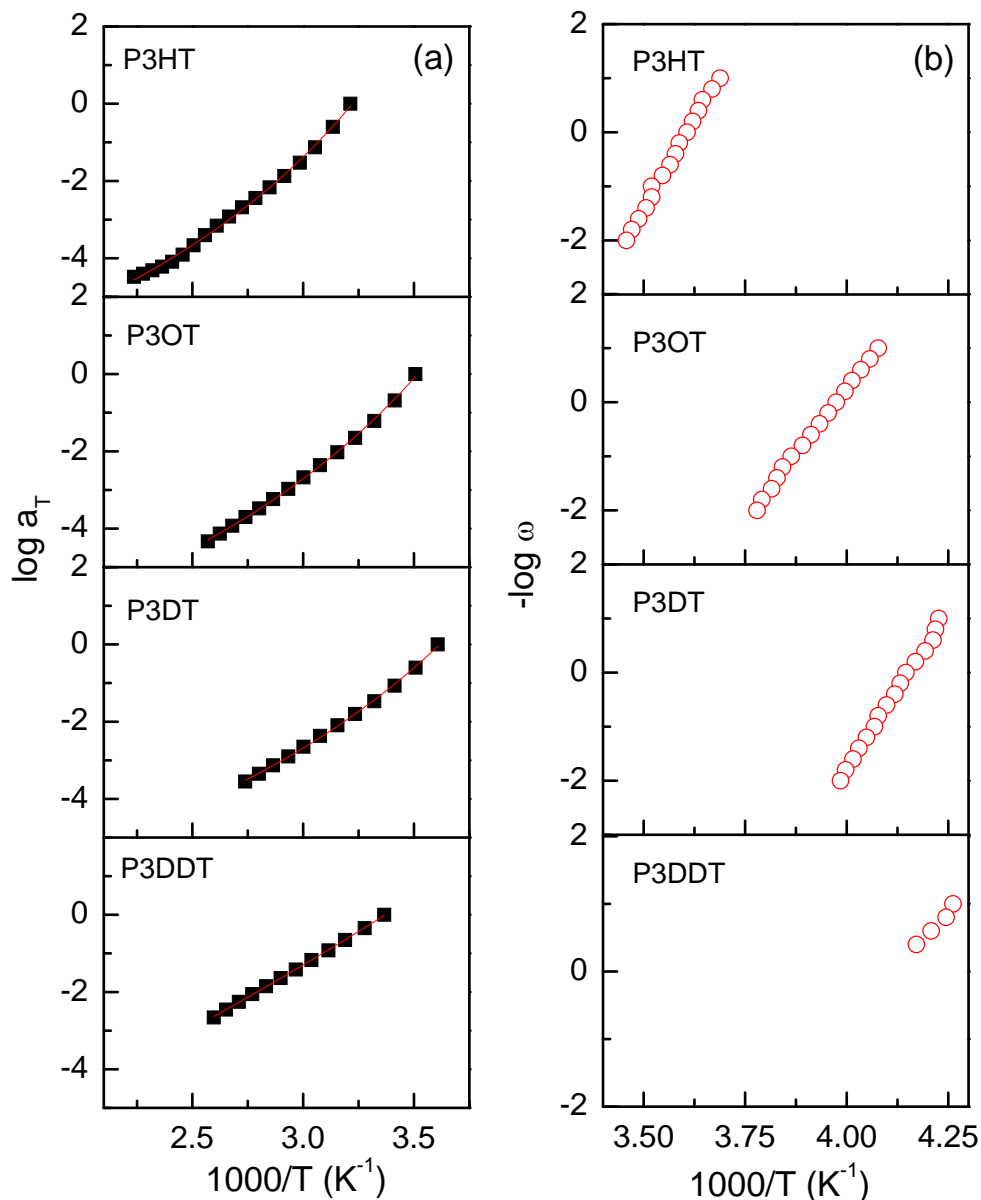
**Figure 6.5:** (a) Logarithm of shift factor $\log a_T$ in the flow transition region and (b) -$\log \omega$ in the $\alpha$ relaxation range $vs$ 1000/T for regio-random P3HT, P3OT, P3DT and P3DDT. Thin lines in part (a) are fits using VFTH equation. The data for the $\alpha$ process in part (b) are estimated from isochronal data.

ples containing different fractions of crystalline material. The results clearly indicate that the side chain crystallization process is strongly influencing the mechanical properties. Similar but weaker effects occur for P3DT where DSC experiments show only weak crystallization effects after long times and degrees of crystallinity which are significantly smaller than in P3DDT (see Chapter 7).

Irrespective of this problem with crystallization effects in the $\alpha$ relaxation range, the temperature dependence of the flow transition can be parameterized by using the Vogel-Fulcher-Tamman-Hesse (VFTH) equation (equation 2.2) to fit the shift factors $a_T$ in the flow range as shown in Figure 6.5a. Curvature $B$ and Vogel temperature $T_V$ where the relaxation time diverges are listed in Table 6.1. To estimate the fragility $m_\alpha$, $\alpha$ relaxation temperatures are determined based on the $\alpha$ peak positions in $G_T''$ isochrones measured for different frequencies $\omega$. The data are shown in Figure 6.5b. The calculated steepness indices $m_\alpha$ scatter around 40 indicating strong glasses and indicates cooperative nature of the process. A clear trend in the $m_\alpha$ values depending on the side chain length is not observed.

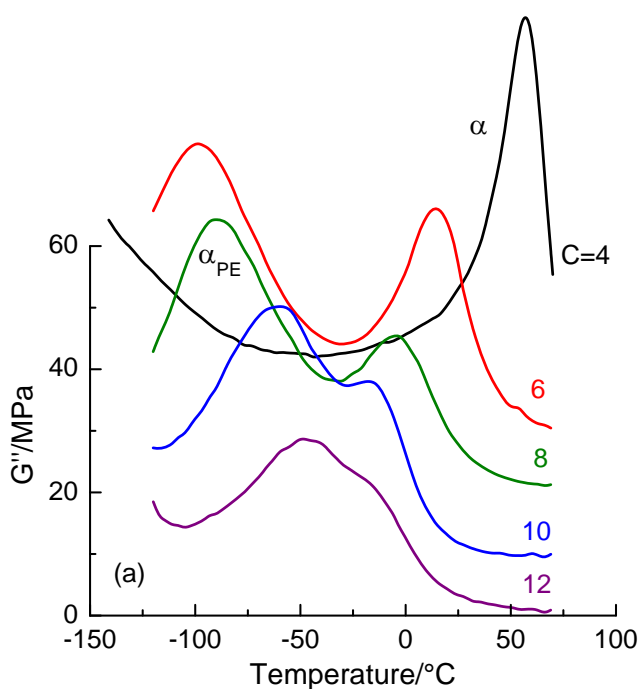## 6.2 Dynamics of regio-regular poly(3-alkyl thiophenes)



**Figure 6.6:** (a) Shear loss modulus $G''$ vs. temperature for regio-regular P3ATs measured at a frequency of 10rad/s. The curves are vertically shifted for reasons of clarity.

Temperature-dependent shear loss modulus data $G''(T)$ for the regio-regular P3AT series provide additional insights. Interestingly, two independent relaxation processes are also seen for these semi-crystalline samples with highly crystalline thiophene backbones (Figure 6.6). The low temperature process corresponds to $\alpha_{PE}$ process within the alkyl nanodomains,

while the high temperature process is quite similar to the $\alpha$ relaxation process in regio-random P3ATs with identical side chain lengths. The relative intensity of the $\alpha_{PE}$ process is large compared to that of the $\alpha$ relaxation and dominates in the higher members. With increasing side chain lengths $\alpha_{PE}$ moves to higher temperature, while the conventional $\alpha$ peak moves to lower temperature due to internal plasticization. [161] This relaxation behavior is similar to that of regio-random P3ATs, higher poly(n-alkyl methacrylates) and other comb-like polymers containing long alkyl groups in the side chain. [18] In particular, the $\alpha_{PE}$ peaks occur in all these cases at temperatures which are comparable as expected for a main chain independent dynamics within self-assembled alkyl nanodomains. Exception again is P3BT, where only a single $\alpha$ relaxation peak is observed in the investigated temperature range.
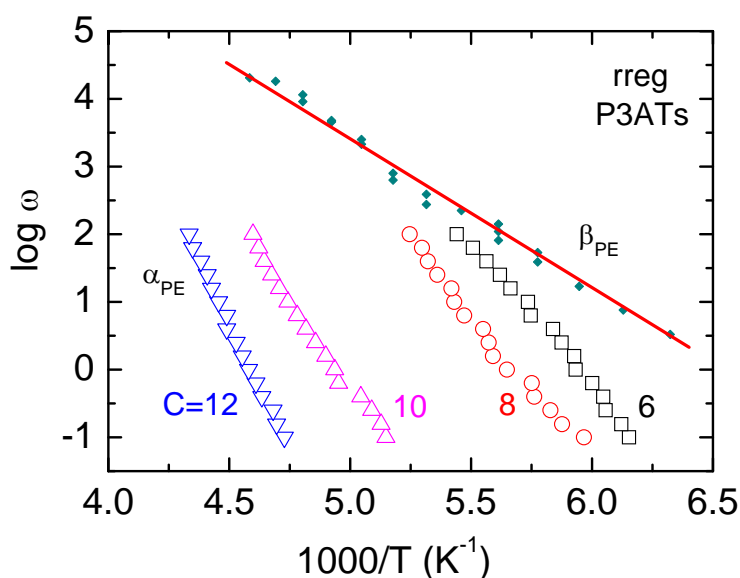


**Figure 6.7:** Arrhenius plot $\log\omega$ $vs$ 1000/T for regio-regular P3HT (black), P3OT (red), P3DT (magenta) and P3DDT (blue). Hollow symbol corresponds to $\alpha_{PE}$ process taken from the isochrones measured at different temperatures. Data for the $\beta_{PE}$ process in PnAAs (diamonds) with short side chains (C=4 and 5) are shown for comparison. [18]

An Arrhenius plot $\log\omega$ $vs$ 1000/T showing the frequency-temperature dependencies of the $\alpha_{PE}$ processes for different regio-regular P3ATs is shown in Figure 6.7. The steepness index $m_{\alpha_{PE}}$ shows values in the range $m \approx 19 - 37$ (Table 6.2). This corresponds to apparent activation energies in the range $E_{A,\alpha_{PE}} \approx$ 29-55 kJ/mol and limiting frequencies in the range $10^{20}$-$10^{31}$ rad/s. These values indicate consistently strong deviations from an Arrhenius like temperature dependence typical for cooperative processes.

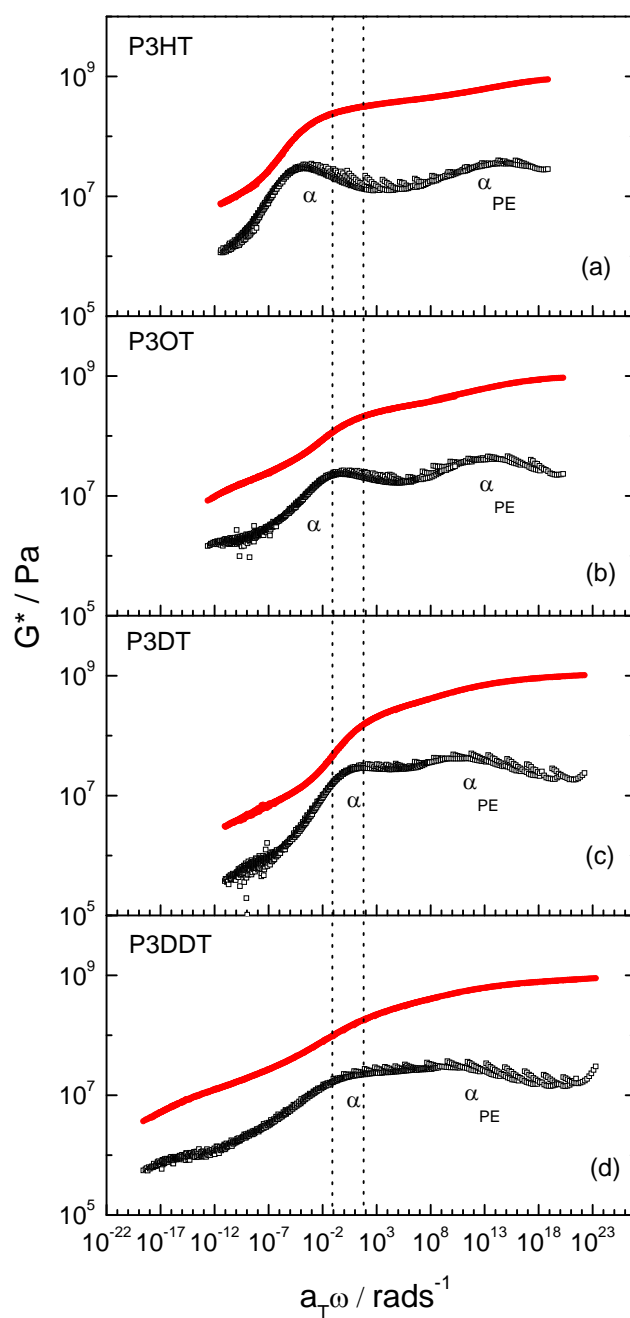Further, master curves are constructed based on the isotherms measured in the frequency

**Figure 6.8:** Master curves log G* $vs$ log $a_T\omega$ for a series of regio-regular P3ATs. Storage modulus $G'$ (solid symbols) and loss modulus $G''$ (open symbols) for (a) P3HT , (b) P3OT , (c) P3DT and (d) P3DDT with $T_{ref}$=-12°C are shown. The isotherms are measured using stripes during step-wise heating starting at -120°C. The dashed lines indicate the frequency window of the measurements. Isotherms in the range 0.1 to 100rad/s with five points per decade are measured in the temperature range of $T$=-120°C to $T$=120°C. Soak time for each temperature was 600s. The temperature step was 4K in the $\alpha$ relaxation range, 10K significantly below and 4K above this region.
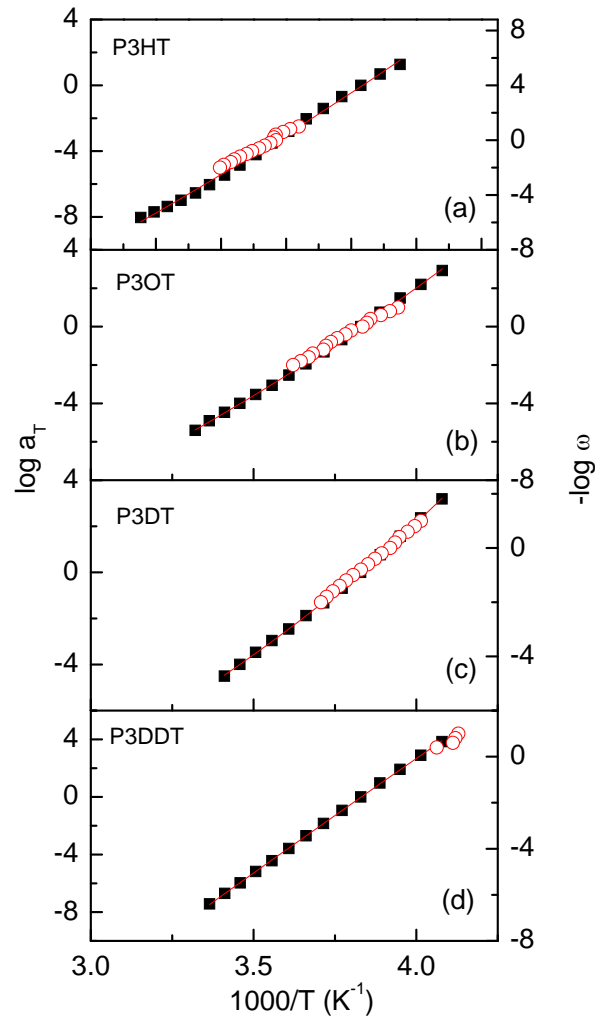
**Figure 6.9:** Logarithm of shift factor $\log a_T$ (l.h.s) and $-\log\omega$ (r.h.s) $vs$ 1000/T for regio-regular (a) P3HT, (b) P3OT, (c) P3DT and (d) P3DDT. Solid squares represents the shift factors from the master curve construction and the thin lines are fits using VFTH equation. Red circles correspond to the $\alpha$ peak maxima in $G''(T)$ isochrones measured at different frequencies $\omega$.

**Table 6.2:** Characteristic parameters for regio-regular P3ATs

| Label | $T_\alpha$[†] | $T_{\alpha,PE}$[†] | $B$ | $T_V$ | $m_{\alpha,PE}$[†] |
|---|---|---|---|---|---|
|  | (°C) | (°C) | (K) | (°C) |  |
| rreg P3HT | 14 | -99 | 6375 | -195 | 19 |
| rreg P3OT | -5 | -88 | 3963 | -165 | 26 |
| rreg P3DT | -10 | -62 | 2926 | -141 | 27 |
| rreg P3DDT | -15 | -44 | — | — | 37 |

[†] Measurement frequency $\omega = 10$ rad/s.

range from 0.1 to 100 rad/s in the temperature range from glassy region to the rubber plateau region as shown in Figure 6.8. In accordance with the time-temperature superposition principle, the isotherms have been horizontally shifted to form master curves showing all relevant relaxations. During the horizontal shifts, different temperature dependence of the two relaxation processes ($\alpha$ and $\alpha_{PE}$) is neglected. A common reference temperature of $-12°C$ has been chosen. Three distinct regions appear in the master curves for all P3ATs. (i) the $\alpha_{PE}$ relaxation process in alkyl nanodomains at short relaxation times; (ii) process at long relaxation times ($\alpha$) corresponding to cooperative motions of those monomeric units which are in the amorphous state and (iii) the plateau region at low frequencies with storage moduli of about 10 MPa indicating a significant fraction of crystalline thiophene main chains. Based on the shift factors $a_T$ obtained in the $\alpha$ relaxation range, VFTH parameters (Table 6.2) have been estimated (Figure 6.9). A similar temperature dependence is indicated if the $\alpha$ peak positions in $G''(T)$ isochrones are evaluated (Figure 6.9). Steepness index $m_\alpha$ scatter around $m_\alpha \approx 40$ like observed for regio-random systems. No smooth master curves could be obtained in the region of the $\alpha_{PE}$ process. This is most likely due to the deviations between the $T$ dependencies of $\alpha_{PE}$ and $\alpha$ relaxations or possibly also related to changes in $\alpha_{PE}$ peak shape with temperature. Note that a flow region is not appearing below $T_m$ what seems to be natural for a semicrystalline system containing a lot of nanosized crystals connecting the chains physically.

## 6.3   Comparison between both series

The main features of the shear relaxation curves of regio-random and regio-regular P3ATs are quite comparable although these systems are structurally quite different systems (Figure 6.10). The thiophene main chains are amorphous in regio-random systems while highly crystalline in regio-regular P3ATs. Nevertheless, two prominent relaxation processes are observed in all samples and the trends are quite similar. Frequency temperature position and intensity of the $\alpha_{PE}$ processes are comparable for regio-regular and regio-random P3ATs containing alkyl groups with identical length. This confirms nicely that the $\alpha_{PE}$ process is related to a dynamics within alkyl nanodomains which is basically main-chain independent and that nanophase separation of main and side chains occurs in both cases. A similar shape and intensity of the $\alpha_{PE}$ process would not be found if the side chain dynamics would strongly depend on the crystalline state of the main chains in their environment. This statement holds even considering the observation that not all main chains are crystalline in regio-regular P3ATs. [149–152] Main difference between the relaxation spectra for regio-random
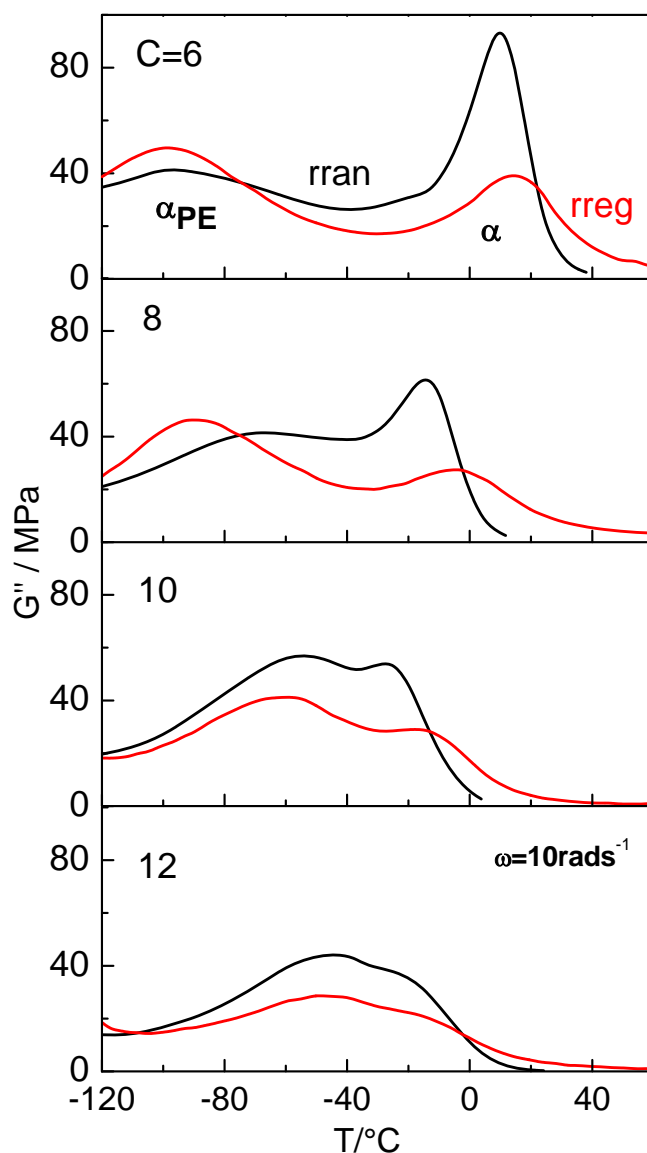
**Figure 6.10:** Comparison of shear loss modulus $G''(T)$ data for regio-random P3ATs (black lines) and regio-regular P3ATs (red lines) measured at an angular frequency of $\omega$=10rad/s.

and regio-regular systems is that the intensity of the $\alpha$ processes in regio-regular P3ATs is significantly lower and that their maxima are slightly shifted to higher temperatures compared to corresponding regio-random P3ATs. This is an expected finding considering the fact that a large fraction of the main chains in regio-regular P3ATs is crystalline. The negligible change in the $\alpha_{PE}$ peak intensity for regio-regular P3ATs compared to their melt quenched regio-random counterparts shows that the fraction of crystalline methylene units in these samples is obviously very small. Slightly broader $\alpha_{PE}$ peaks in some of the regio-random

P3ATs may indicate the existence of wider interfacial regions or certain density gradients within the alkyl nanodomains.

Summarizing the results presented in this chapter, one can put on record that two independent relaxation processes, $\alpha$ and $\alpha_{PE}$, corresponding to cooperative motions of complete monomeric units and $CH_2$ units within the alkyl nanodomains respectively occur in regio-regular and regio-random P3ATs. These processes appear at similar positions. The $\alpha_{PE}$ process shifts to higher temperatures with increasing side chain lengths while the $\alpha$ process shifts to lower temperature due to internal plasticization. Position and intensity of the $\alpha_{PE}$ process are nearly independent of the confining environment, i.e. for regio-random P3ATs where completely amorphous main chains exist and regio-regular P3ATs where the main chains are highly crystalline. Finally one can conclude that (i) nanophase separation of main and side chains exists in both the series and (ii) alkyl nanodomains are basically amorphous for melt quenched regio-random as well regio-regular P3ATs with $C \leq 10$ alkyl carbons per side chains.

# Chapter 7

# Side chain crystallization and polymorphism in poly(3-alkyl thiophenes)

In this chapter, results for regio-random and regio-regular P3DDT (C=12) and regio-random P3DT (C=10) samples are compiled showing the effects of side chain crystallization in DSC, x-ray scattering and infrared spectroscopy (IR) data.

## 7.1 Regio-random poly(3-dodecyl thiophene)

DSC heating scans for differently prepared regio-random P3DDT ($C = 12$) samples are presented in Figure 7.1. A large melting peak (I) at 44.5°C is seen for the as received sample while a two peak feature (II & III) is observed in DSC scans performed after slow cooling (-20 K/min). Peak III has an onset at about -25°C and peak II starts at about 5°C. Melting peak I at 44.5°C, which was seen for the as received sample, is not observed in this case. The double peak feature was re-traceable after fast quenching from 100 to -60°C with a nominal rate of -200 K/min. This indicates that even fast quenching cannot suppress this feature.

In order to clarify further details, isothermal crystallization experiments at different temperatures ($T_c = -25$, 5 and 26°C) have been performed. This corresponds to temperatures near the onset of the melting peaks III, II and I seen in Figure 7.1. The crystallization time $t_c$ was varied between 5 minutes and 7 hours at each temperature $T_c$. The results of isothermal crystallization experiments are presented in Figure 7.2. Heating scans measured after crystallization at $T_c = -25$°C show an increase of peak intensity and a slight shift of the
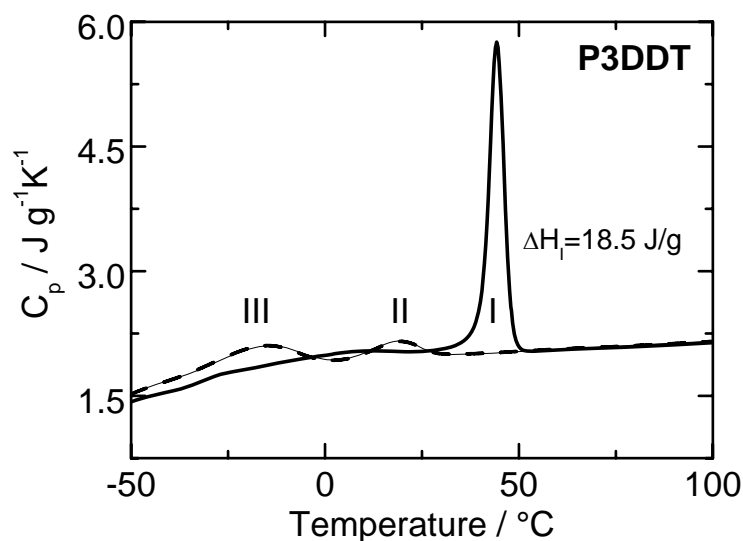
**Figure 7.1:** DSC heating scans regio-random P3DDT (d$T$/d$t$ = 20 K/min) performed on samples with different thermal history. Scans for the as received sample (thick solid line), a second scan after slow cooling to -60°C with d$T$/d$t$= -20K/min (thin solid line), and a third scan after quenching to -60°C with d$T$/d$t$= -200K/min (thick dashed line) are compared.
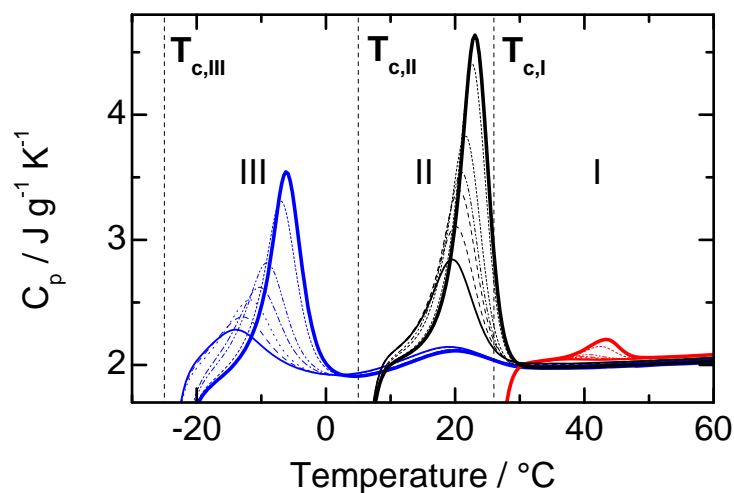


**Figure 7.2:** DSC heating scans for regio-random P3DDT (d$T$/d$t$ = 20 K/min) preformed after isothermal crystallization for different times $t_c$ (from bottom to top: 5, 10, 20, 30, 60, 240, 420 min) at $T_c$ =-25°C (blue), 5°C (black) and 26°C (red). The labels I, II and III indicate the different melting peaks. The samples are cooled from 80°C to $T_c$ with a nominal rate of 200K/min.

peak position with time $t_c$. The results indicate that heat of fusion $\Delta H_{III}$ as well as melting temperature $T_{m,III}$ do systematically increase. A weak additional peak (II) at about 20°C is seen in all scans. This peak remains practically unaffected if $t_c$ is varied. The crystalline

fraction related to this peak is probably formed during cooling from 80 to -60°C. Results from isothermal crystallization experiments at $T_c = 5$°C and 26°C show that similar changes with time $t_c$ are observed for peak II and peak I, respectively. Additional contributions at other temperatures are not observed under these conditions.
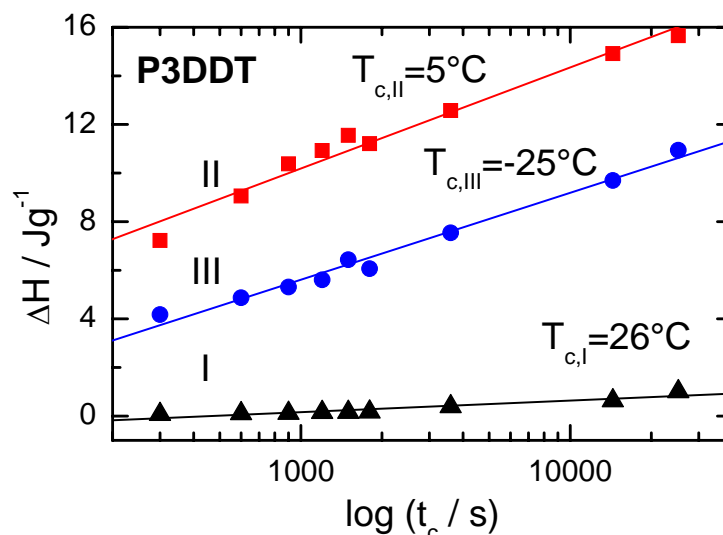


**Figure 7.3:** Heat of fusion $\Delta H$ *vs.* crystallization time $t_c$ for regio-random P3DDT measured at $T_c = -25$°C, 5°C and 26°C. Heats of fusion are calculated based on the area of the melting peaks in Figure 7.2.

The dependence of the heat of fusion $\Delta H_I, \Delta H_{II}, \Delta H_{III}$ on isothermal crystallization time $t_c$ measured at different temperatures $T_c$ is compared in Figure 7.3. Obviously, the degree of crystallinity $D_c$ increases in all cases on logarithmic time scales. Clear indications for a significant primary crystallization step are not observed. One can estimate based on existing information about the heat of melting for different crystalline forms ($\Delta h_{hex} = 3.07 - 3.4$ kJ/mol [128, 168], $\Delta h_{ortho} = 3.4 - 3.99$ kJ/mol [168, 169], $\Delta h_{triclin} = 4.2$ kJ/mol [128]) that at most 12% of the $CH_2$ units are crystalline for the as received sample.

The melting temperatures $T_m$ of the crystals grown at different temperatures $T_c$ are obviously not comparable, i.e. the crystalline state seems to depend significantly on the crystallization conditions (Figure 7.2). In general, melting seems to appear in the same temperature range like in case of alkanes and other side chain polymers containing crystallizable alkyl groups with similar length. [53, 168] Note, that the occurrence of alkyl groups, which can crystallize either on a hexagonal or on orthorhombic lattice, has been reported recently for eicosylated poly(ethyleneimine) with $C = 20$ alkyl carbons in the side chain. [52, 128] A resulting question is whether the appearance of different $T_m$ values depending on the crystallization condi-

tions indicates polymorphism in P3DDT, i.e. the existence of different crystalline forms, or it is simply a result of other effects like differences in the thickness of the crystal lamellae.

A standard methodology to answer this question is to perform wide angle x-ray scattering (WAXS) measurements. The results of experiments on differently prepared P3DDT samples are presented in Figure 7.4. The WAXS data for the as received sample, which should contain according to our DSC data 10-12% crystalline methylene units, and a freshly quenched sample containing presumably only a very small fraction of crystalline $CH_2$ units are quite similar. Main difference between both data sets is the appearance of higher orders belonging to the pre-peak at $2q_{max}$ and $3q_{max}$ related to a lamellar packing of main and side chain domains on the mesoscale for the as received sample. Otherwise, there is in all WAXS curves an intense amorphous halo with a maximum at $2\Theta \approx 20°$ corresponding to $q = 4\pi \sin\Theta/\lambda = 1.41 \text{Å}^{-1}$. The shape of this halo is not significantly affected by the chosen program. The only difference might be a weak shoulder in the range around $2\Theta \approx 22°$ ($q \approx 1.63 \text{ Å}^{-1}$). It is well known that WAXS pattern of side chain polymers containing a significant fraction of hexagonally packed methylene units in the alkyl groups are usually characterized by a sharp peak at $2\Theta \approx 21°$ ($q \approx 1.49 \text{Å}^{-1}$) as seen in the poly(n-octadecyl methacrylate) [PODMA] data in Figure 7.4. [50, 51, 53] In case of orthorhomically packed methylene units, an additional peak appears at around $2\Theta = 23.5°$ ($q = 1.66 \text{Å}^{-1}$) [128]. Obviously, clear peaks related to the crystalline fraction are not seen in WAXS data for our P3DDT sample. The shoulder at $2\Theta \approx 22°$ indicates most likely a small fraction of crystalline side chain segments. Information about the packing of the crystalline methylene units, however, can not be extracted from WAXS data for regio-random P3DDT. The problem is that the relevant scattering peaks sit on top of a strong amorphous halo since the degree of crystallinity is very small as compared to those of other semi-crystalline side chain polymers studied in the literature. Note that the WAXS data for semi-crystalline PODMA shown for comparison in Figure 7.4 are measured on a sample containing $\approx 30\%$ crystalline $CH_2$ units [53] in an octadecyl side chains, while the P3DDT sample contains in the average around 12% crystalline $CH_2$ per dodecyl (C=12) side chain. Since main chains are amorphous in both the cases, they will also contribute to the halo. The presented results demonstrate that DSC is a very sensitive tool to detect small fractions of crystalline material which are not easily detectable by WAXS experiments.

Interestingly, the pre-peak in the $q$ range around 0.261 $\text{Å}^{-1}$ which is previously discussed in section 5.2 is significantly and systematically affected by crystallization. A detectable
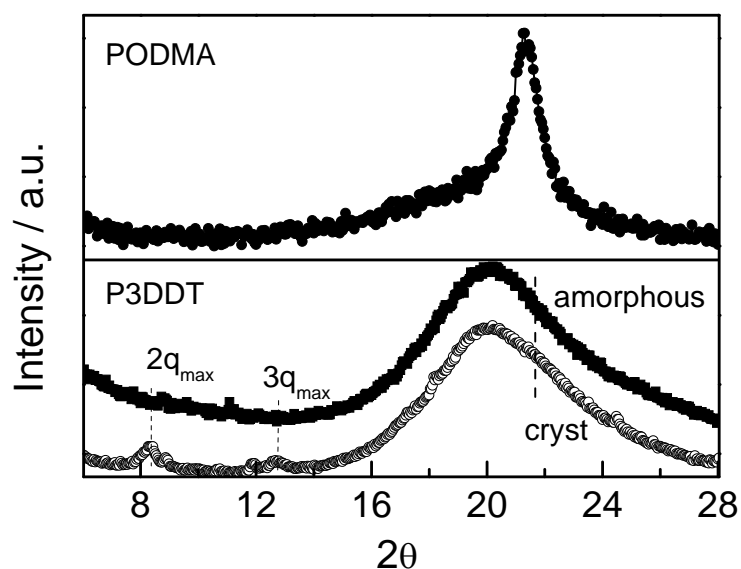
**Figure 7.4:** Wide angle x-ray scattering for regio-random P3DDT measured at room temperature. WAXS data for a semi-crystalline as received sample (open circles) and a practically amorphous P3DDT sample produced by fast melt quenching with -200 K/min (full squares) are compared. Higher order peaks belonging to the pre-peak at $2q_{max}$ and $3q_{max}$ are labeled. Results for poly($n-$octadecyl methacrylate) in the semi-crystalline state (full circles) from Ref. [53] are shown for comparison.
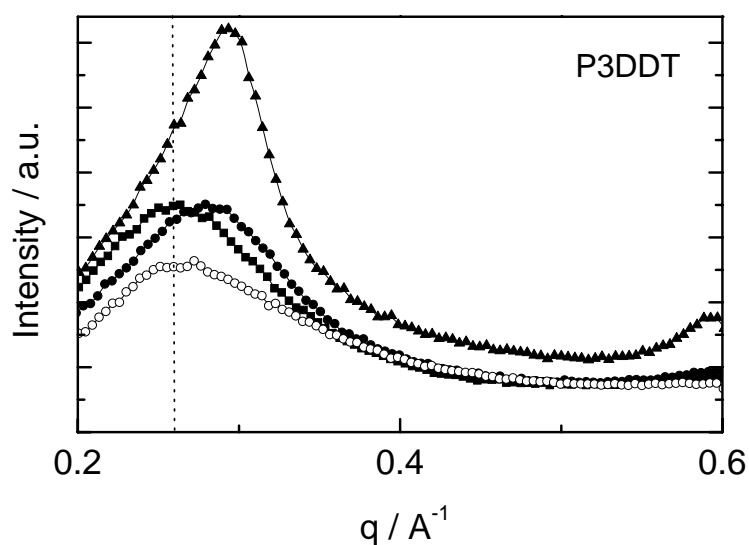


**Figure 7.5:** Scattering pattern $I(q)$ for regio-random P3DDT measured at 25°C after fast cooling from the molten state (○), at room temperature on an as received sample (△) as well as on samples which are crystallized for 7 hours at -25°C (■) and 5°C (●).

shift of the peak maximum position is observed for semi-crystalline samples compared to the situation for the freshly quenched samples. This shows that the side chain crystallization

changes the overall structure of nanophase-separated polymers particularly the average interlayer distance $d_{nps}$ (Figure 5.3). As seen in Figure 7.5, the pre-peak narrows and the peak maximum shifts a little bit to lower $q$ values (0.255 Å$^{-1}$) if the sample is crystallized for 7h at $T_c = -25°$C. This corresponds to an increase of $d_{nps}$ due to side chain crystallization from 24.1 Å to 24.6 Å. Higher order peaks at $2q_{max}$ and $3q_{max}$ start to appear for the higher degrees of crystallinity indicating a lamellar morphology (Figure 7.4). Similar behavior is seen for crystallizable side chain polymers like poly(n-octadecyl methacrylate) (PODMA) where the methylene units are packed on a hexagonal lattice. This effect has been explained by an increase of the all trans content in the alkyl groups during crystallization. [51] Regio-random P3DDT samples in the as-received state and samples crystallized for long times at $T_c = 26°$C show an opposite trend, i.e. the pre-peak maximum shifts to larger $q$ values (0.291 Å$^{-1}$) corresponding to $d_{nps} = 21.6$ Å due to crystallization. This indicates that the average interlayer distance $d_{nps}$ is reduced if the alkyl groups crystallize under these conditions. Note that a state having an intermediate $d_{nps}$ value (22.8 Å) appears for regio-random P3DDT crystallized at $T_c = 5°$C. In this case, the pre-peak sharpens during crystallization but shifts only slightly to larger $q$ values. A possible interpretation of these finding will be given in discussion (section 9.3).
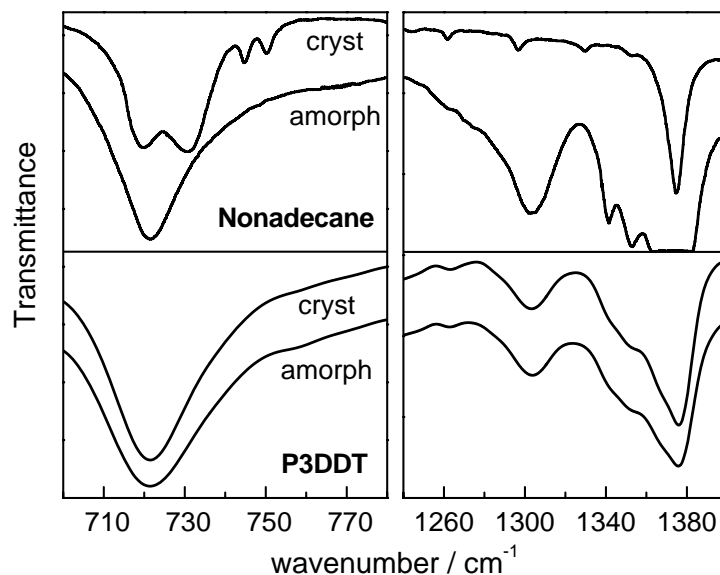


**Figure 7.6:** IR spectroscopy data for the as received, semi-crystalline (cryst) and the quasi-amorphous quenched (amorph) regio-random P3DDT sample are presented. IR results for nonadecane in the molten state (amorph, 29°C) and in the orthorhombically packed crystalline state (cryst, 19.5°C) taken from Ref. [170] are shown for comparison.

Further attempts to verify structural changes and differences in the crystalline packing of the methylene sequences have been made by infrared spectroscopy. This method has been often used to learn more about the crystalline state of alkanes [170, 171], polyethylene [172] and long $CH_2$ sequences in side chain polymers. [128] IR data for P3DDT in the spectral ranges around 720 cm$^{-1}$, where $CH_2$ rocking modes have been reported for crystalline methylene sequences [171, 172], and near 1375 cm$^{-1}$, where usually a $CH_3$ group deformation (U mode) and $CH_2$ wagging modes do appear [171], are shown in Figure 7.6. Results for the as received P3DDT sample having the highest accessible degree of crystallinity (Figure 7.1) are compared with that for a freshly quenched sample, which is practically amorphous. The data show that there are no significant differences between both samples. IR spectra of P3DDT in both states are quite similar to that for molten nonodecane in this wavenumber range (Figure 7.6) and quite different from that for orthorhombic nonadecane crystals [171]. Effects, which allow to analyze the structure of semi-crystalline P3DDT like a series of additional bands around 720 cm$^{-1}$ related to $CH_2$ rocking modes reported for crystalline methylene sequences [128, 170, 171] are not observed. There is also no detectable shift of the $CH_3$ band near 1375 cm$^{-1}$ and no clear indication for the disappearance of higher $CH_2$ wagging modes below 1375 cm$^{-1}$ being additional features reported for crystalline alkyl groups. [171] Presumably, this is again a consequence of the small degree of crystallinity of the investigated P3DDT sample. The presented results show clearly that it is hard to get detailed information about the structure of regio-random P3DDT in the crystalline state based on standard techniques like x-ray scattering and vibration spectroscopy.

## 7.2   Regio-random poly(3-decyl thiophene)

Isothermal crystallization experiments on P3DT performed at -25°C and 5°C over long times show that side chain crystallization occurs (Figure 7.7) like shown for P3DDT. Thick line represents a scan for an as received sample. A glass transition around -32°C is seen followed by an endotherm at 48°C designated as melting of form I. The estimated degree of crystallinity of the alkyl groups is around 5%. On varying the crystallization times from 5 min to 7 h at $T_c$=-25°C, subsequent heating scans show an increase in the intensity of the melting peak of form III at about 10°C appearing significantly above $T_g$. Heat of fusion and melting temperature do increase systematically. Similar trends occur when the sample is annealed at $T_c$=5°C leading to a tiny melting peak centered around 28°C (form II). In contrast to the findings for regio-random P3DDT, form I does not grow after annealing at 26°C on time scales of hours. Possibly longer times or slightly different temperatures are required to get a significant fraction of form I crystals which are present in the as-received sample.
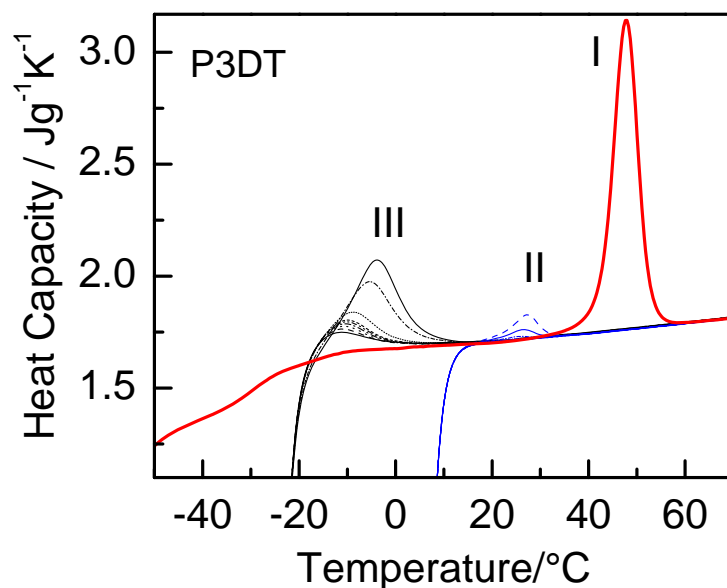
**Figure 7.7:** DSC heating scans (dT/dt=20K/min) for regio-random P3DT performed after crystallization for different times $t_c$ (5, 10, 15, 20, 25, 30, 60, 240 and 420 min) at $T_c$= -25°C (black) and 5°C (blue). Thick line (red) represents a scan for an as received sample. The melting peaks of different forms are labeled with I, II and III.

## 7.3    Regio-regular poly (3-dodecyl thiophene)

The results of isothermal crystallization experiments on a regio-regular P3DDT sample are presented in Figure 7.8. Two main features are seen in DSC heating scans performed on samples which are melt quenched and isothermally crystallized at $25°C$ for different times $t_c$. Firstly, broad endotherms are observed in the temperature range 0°C < T <70°C considered as the region where crystalline $CH_2$ units in the side chains melt. Secondly, a trimodal melting peak in the range 120 °C < T < 170°C corresponding to melting of crystalline thiophene rings in the main chains is found. On annealing for long times at room temperature ($25°C$), the state of the side chains seemingly changes. This can be concluded from an increase of the melting endotherm at $40°C$. The degree of crystallinity also increases with the annealing time from initially about $5\%$ to about $8\%$ of the $CH_2$ units after annealing for 4 months. These values are estimated based on experimental $\Delta H_{m,sc}(t_c)$ values and existing information about the heat of melting for hexagonally packed $CH_2$ units ($\Delta h_{hex} = 3.07 - 3.4$ kJ/mol). [168] The bump at around $55°C$ exists in all the cases and remains basically unaffected by isothermal crystallization at 25°C. This might also be an indication for the coexistence of different polymorphic side chain crystals formed in self assembled alkyl nanodomains. Interestingly, the changes in the melting behavior of the side

chains are accompanied by changes in the melting behavior of the main chains above 120°C. For quenched samples, fractions melting at lower temperatures are dominant while with long annealing this fraction reduces and simultaneously fractions melting at higher temperature increases. For the as received sample, the complete three peak feature is dominated by one peak appearing at the highest temperature ($T_m \approx 161$°C). For quenched samples, the peak at lower temperatures at around $T_m \approx 145$°C dominates. One can conclude that irrespective of the state of the main chains, long side chains can crystallize. It can be also seen that strong interrelations between main and side chain crystallization processes exist. This is interesting and can be understood as a competition of both structure formation mechanisms and will be discussed in section 9.3. Further details, however, have to be puzzled out in future investigations.
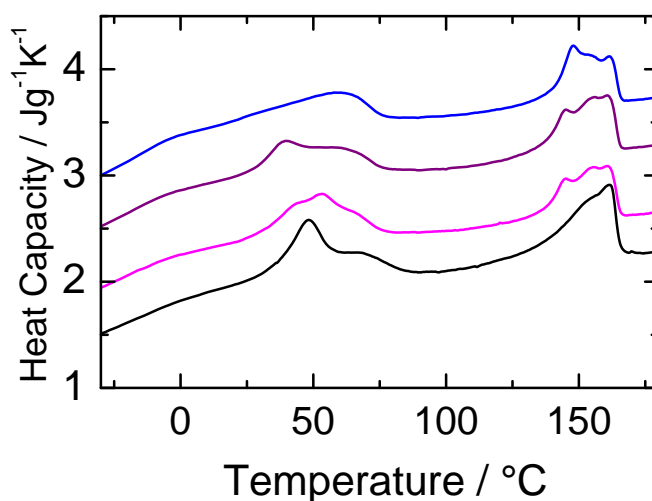


**Figure 7.8:** DSC heating scans for regio-regular P3DDT at the rate of 20K/min after melt quenching (blue) and after 24 hrs (purple) and 4 months (magenta) annealing at $25°C$. Black curve represents the as received sample. All upper curves are vertically shifted by 0.5 J/gK.

Summarizing the main findings of this chapter, one conclude that the alkyl groups can occur in different polymorphic state for regio-random P3DDT, regio-random P3DT and regio-regular P3DDT as seen by multiple melting peaks in DSC measurements. It is hard to predict the structure of the side chains by x-ray scattering and IR spectroscopy due to very low degree of crystallinity. Hence, more sophisticated methods need to be applied in the future, such as solid state NMR to confirm and specify the nature of the different crystalline states. Changes in the polymorphic state of the side chains in regio-regular P3DDT are obviously connected with change in the crystal structure of the thiophene main chains.

# Chapter 8

# Long term changes in the dynamics of poly(3-alkyl thiophenes)

In this chapter, long term behavior of P3ATs is studied in order to understand the influence of side chain crystallization and physical aging on the dynamics of these nanophase separated polymers.

## 8.1   Regio-random poly(3-alkyl thiophenes)

***Regio-random poly(3-dodecyl thiophene).***  Considering the calorimetric data presented in chapter 7, side-chain crystallization in regio-random P3DDT is practically unavoidable below room temperature. Even for the highest DSC cooling rates (nominally -200K/min) melting peaks appear in the subsequent heating scans (Figure 7.1). Three distinct melting peaks between -10°C and 50°C have been observed after isothermal crystallization at -25, 5 and 26°C (Figure 8.1). This indicates polymorphism in regio-random P3DDT. The melting temperatures are quite comparable to that of alkyl groups in other side chain polymers and alkanes supporting the idea that side chain crystallization occurs in regio-random P3ATs. Further, it will be interesting to see whether and to what extent side chain crystallization influences the mechanical properties of these heterogeneous systems and in particular the dynamics in the alkyl nanodomains.

To study the influence of the side chain crystallization on the mechanical properties, isothermal crystallization experiments were performed in the shear instrument. Melt-quenched strips were annealed under isothermal conditions at temperatures -25°C and 5°C respectively
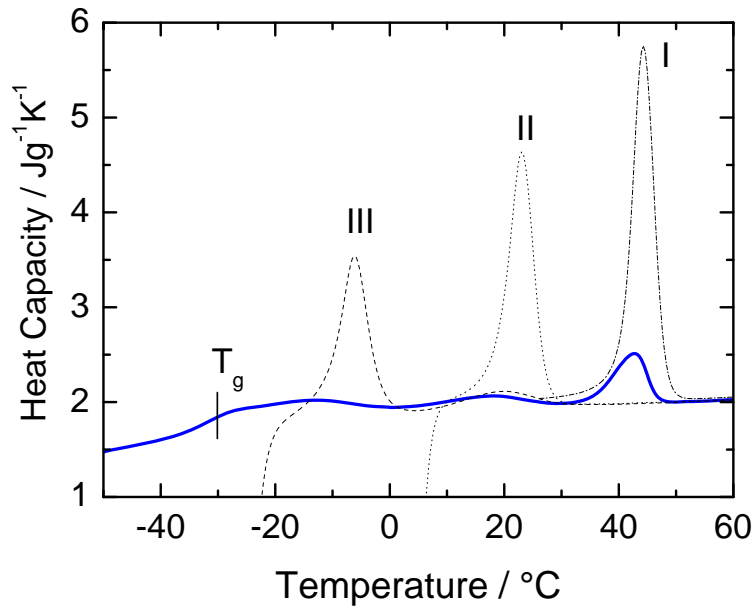
**Figure 8.1:** DSC heating scans for differently crystallized regio-random P3DDT samples measured with a rate of dT/dt = 20K/min. The bold line corresponds to the sample crystallized at room temperature for 96h after cooling the sample at a rate of -20K/min from 90°C to -60°C. Dashed line and dotted line corresponds to sample crystallized at $T_c$=-25°C and $T_c$=5°C for 7h respectively. Dashed dotted line corresponds to an as received sample stored for a long time under ambient conditions.

for 420mins. Figure 8.2a shows scans measured during isothermal crystallization at -25°C. The conventional $\alpha$ process shifts significantly to lower frequency or longer relaxation times and broadens with increasing annealing time. Along with that, the low frequency wing of the $\alpha_{PE}$ peak in $G''(\omega)$ goes down. This is accompanied by a systematic increase of $G'$ with time in the entire frequency range from 0.01 to 100 rad/s. Similar trends are visible for the $\alpha$ relaxation in scans measured during isothermal crystallization at 5°C (Figure 8.2b). This temperature is significantly above the glass transition for P3DDT hence only low frequency wing for the $\alpha$ process is visible. This wing continuously moves to lower frequency with increasing annealing time. An increase in the storage modulus $G'$ at low frequency end of the $\alpha$ relaxation is also observed. This effect indicates that a small fraction of crystalline side chains increases the plateau modulus.

A comparison of isochronal scans performed before and after 420 minutes of annealing at -25°C and 5°C indicates that the intensity of the $\alpha_{PE}$ process at low temperatures is significantly reduced due to isothermal crystallization, while the intensity of the $\alpha$ peak seems to be less affected (Figure 8.3). Reduction in the $\alpha_{PE}$ intensity is due to the fact that the crystalline side chains do not contribute to this relaxation process related to cooperative motions
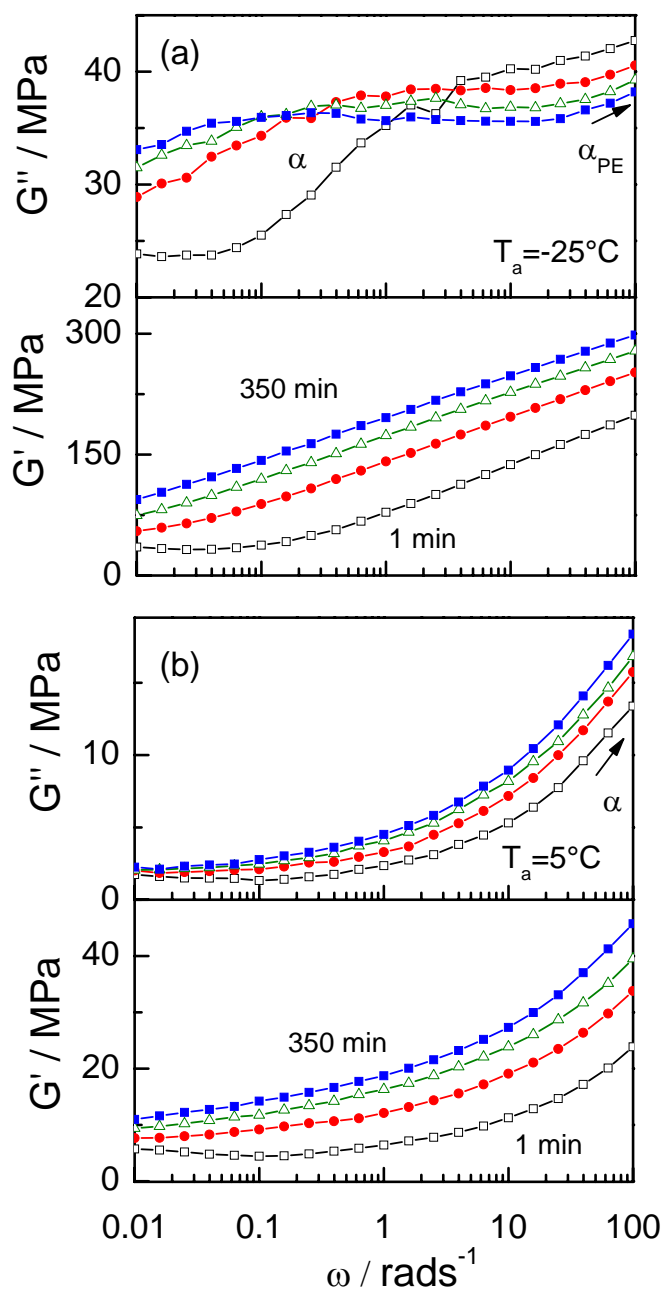
**Figure 8.2:** Dynamic shear loss $G''(\omega)$ and storage $G'(\omega)$ modulus of regio-random P3DDT measured during isothermal crystallization at (a) -25°C and (b) 5°C. The crystallization times are 1 ($\square$), 50 ($\bullet$), 150 ($\triangle$), and 350 minutes ($\blacksquare$) respectively.

within alkyl nanodomains. This confirms nicely that side chain crystallization occurs within self-assembled alkyl nanodomains for P3DDT. A certain broadening of the $\alpha$ peak (Figure 8.2a) might be explained by a non-uniform distribution of density and/or crystallinity in the system leading to a broader distribution of $\alpha$ relaxation times. Note that there is a slight up-
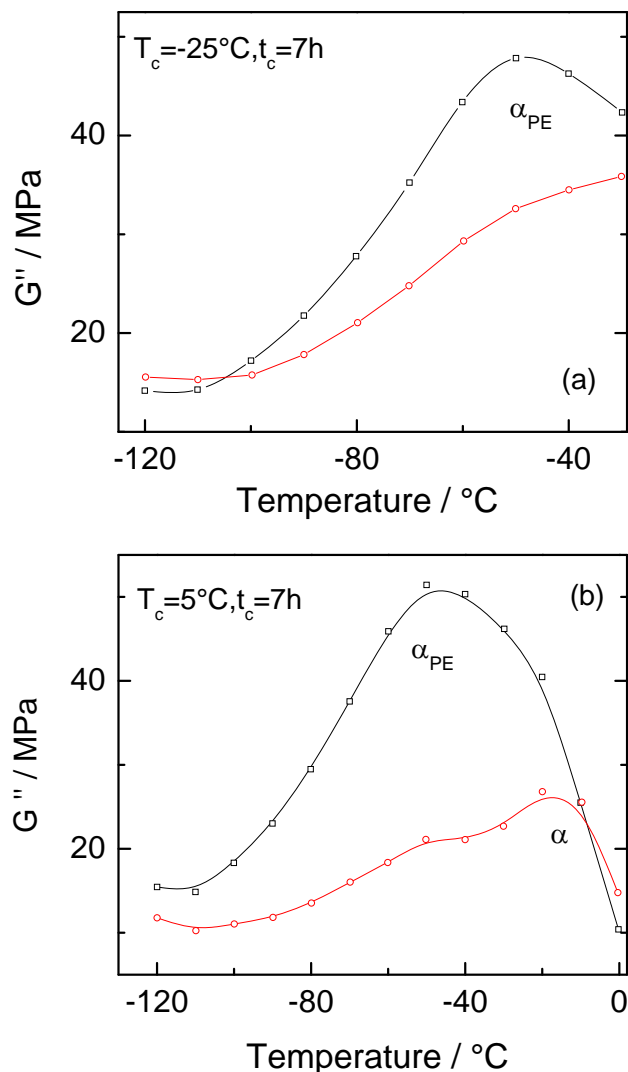
**Figure 8.3:** Shear loss modulus $G''$ $vs$ temperature for regio-random P3DDT measured at an angular frequency of 10 rad/s. Heating ($\square$) and cooling scans ($\circ$) performed before and after 7h crystallization at (a) $T_c$ = -25°C and (b) $T_c$ = 5°C are compared.

turn in $G''(T)$ at very low temperature after crystallization which may indicate an upcoming secondary relaxation process outside the temperature range of measurements (Figure 8.3).

***Regio-random poly(3-decyl thiophene).***  Dynamic shear measurements on regio-random P3DT were performed to quantify the effects of slow side chain crystallization processes on the dynamics. Obviously, both relaxation processes, $\alpha_{PE}$ and $\alpha$, are affected by crystallization like in regio-random P3DDT. The $G''$ curves show that the conventional $\alpha$ process
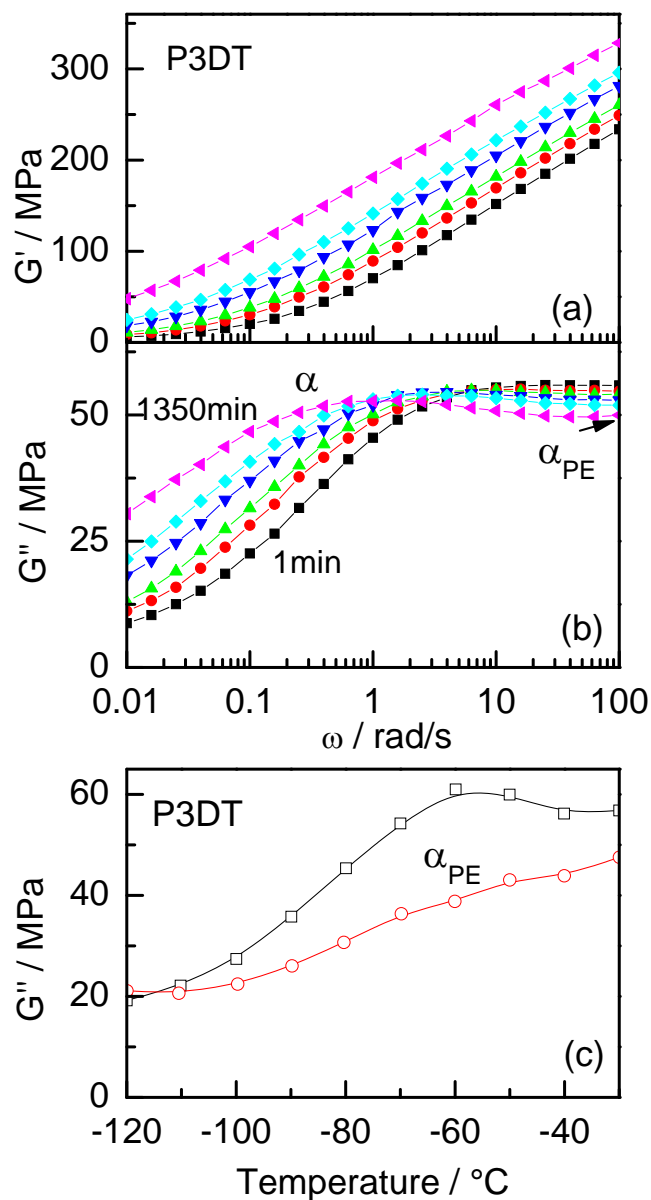
**Figure 8.4:** Dynamic shear storage (a) $G'(\omega)$ and loss (b) $G''(\omega)$ modulus of regio-random P3DT measured during isothermal crystallization at -25°C. Crystallization times are 1 (black), 50 (red), 100 (green), 250 (dark blue), 400 (light blue) and 1350 (magenta) minutes. (c) Shear loss modulus $G''(\omega)$ for P3DT at angular frequency of 10 rad/s. Heating (squares) and cooling (circles) performed before and after isothermal crystallization at -25°C for 24 hours.

slows down and it becomes broader (Figure 8.4b). A systematic increase in the plateau modulus is seen in $G'$ curves (Figure 8.4a). Interestingly, there is again a significant decrease in the intensity of the $\alpha_{PE}$ process during crystallization as seen by comparing the isochrones measured before and after isothermal annealing at -25°C for 24 h (Figure 8.4c). This indicates side chain crystallization within existing alkyl nanodomains since crystalline

methylene units cannot contribute any longer to the $\alpha_{PE}$ process. Findings are similar to that of regio-random P3DDT as previously discussed. The observed changes in the conventional $\alpha$ process are an indication for an influence of side chain packing on the mobility of the main chain. In general, there seems to be a certain coupling between main and side chains. The immobile thiophene main chains do hinder side chain crystallization while the packing state of the side chains is affecting the mobility of the thiophene rings in polymer backbone. Hence, the crystallization tendency of the alkyl groups is a driving force for long term changes in the dynamics of main and side chains in nanophase separated P3ATs.

***Regio-random poly(3-octyl thiophene).*** According to the DSC and scattering data reported in sections 5.1 and 5.2, there is no clear indication for side chain crystallization effects in regio-random P3OT. However, it is interesting to see whether equilibration effects below $T_g$ appear on long time scales in this sample and whether or not features similar to the regio-random P3ATs with clearly crystallizable side chains will be observed. This may contribute to a better understanding of equilibration and densification processes in side chain polymers containing alkyl groups.
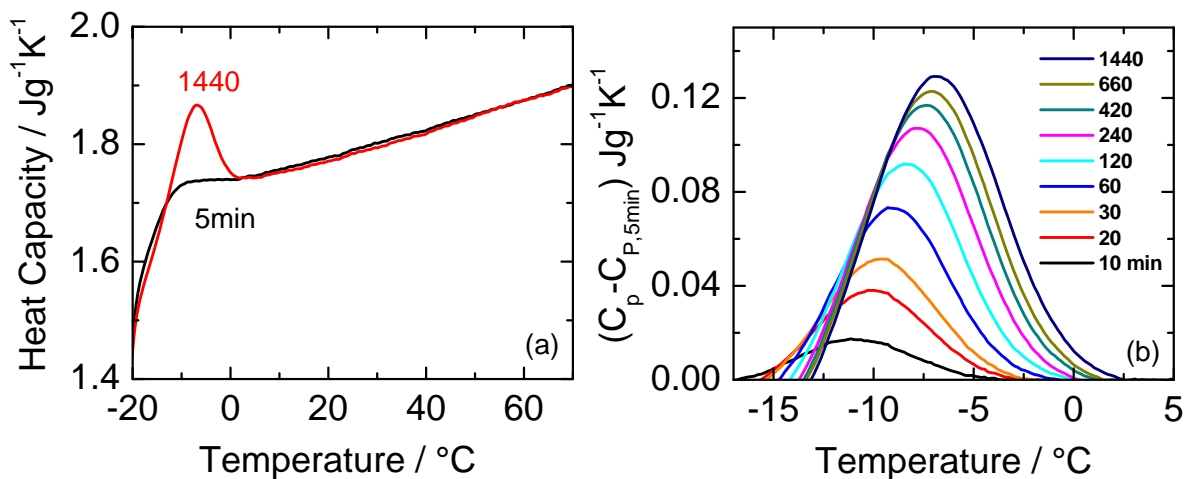


**Figure 8.5:** DSC heating scans for regio-random P3OT samples measured with a rate of dT/dt = 10K/min after different periods of isothermal annealing at $T_e$= -23°C. Annealing experiments are started after quenching the sample at a rate of dT/dt = -200K/min from 90°C to -60°C and reheating it to $T_e$. Original $C_p$ data is shown in part (a). Subtracted scans $C_p - C_{p,5min}$ are shown in part (b).

In order to check whether or not indications for side chain crystallization can be seen in

calorimetric data after extremely long times, isothermal annealing experiments were performed on melt quenched regio-random P3OT at $T_e$ = -23°C for $t_e = 5 - 1440$ mins in the DSC. The results are shown in Figure 8.5. A continuous increase in the enthalpic peak following the glass transition step is seen with the increase in annealing time. The observations are in line with the expectations for a fully amorphous polymer measured after structural relaxation below $T_g$ as shown in Figure 2.6. Structural relaxation peaks are commonly seen in such systems above $T_g$. However, melting of side chain crystals would occur in the same temperature range. Hence, it is difficult to exclude contributions due to side chain melting despite of the fact that peculiarities in the peak shape and time dependence are not observed.
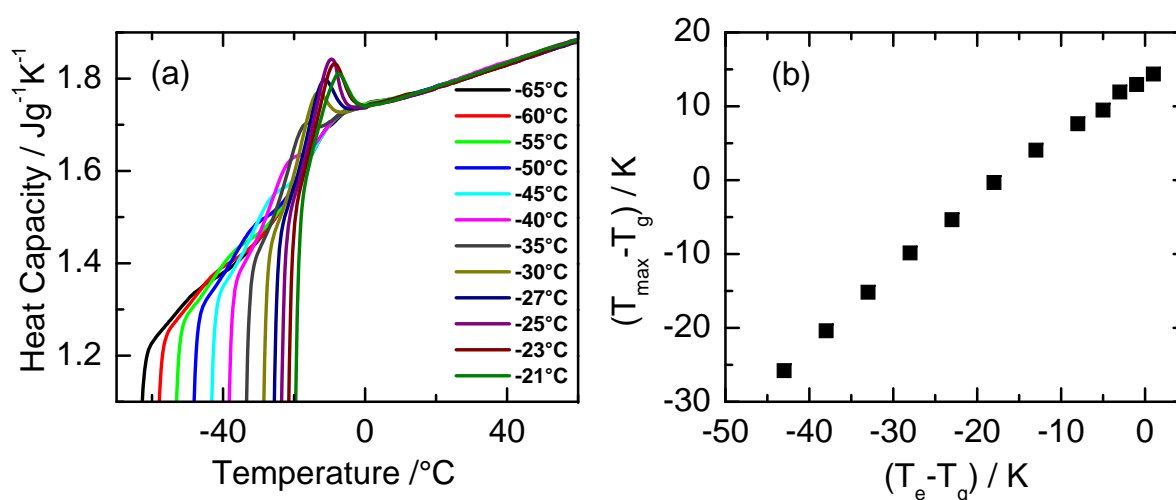


**Figure 8.6:** (a) DSC heating scans for annealed regio-random P3OT samples measured with a rate of dT/dt = 10K/min after quenching the sample at the rate of dT/dt = -40K/min from 90°C to -80°C. Annealing temperatures are indicated in labels and annealing time is 1 hr for all temperatures. (b) Peak temperature $T_{max}$ as a function of aging temperature $T_e$ for an aging time of 1hr.

DSC scans measured after 1h isothermal annealing at different temperatures are shown in Figure 8.6a. Structural relaxation peak $T_{max}$ is commonly observed. The peak shifts systematically to the lower temperatures with decrease in the annealing temperature which a typical feature of amorphous polymers like polystyrene, polymethylmethacrylate and polyethylmethacrylate etc. without crystallization tendency. [173] A plot representing the peak temperature $T_{max}$ as a function of aging temperature $T_e$ is shown in Figure 8.6b. The slope $\mu \equiv dT_{max}/dT_e \approx .90$ is similar to the slopes reported for other amorphous polymers. [173] Obviously, the behavior is quite similar to that of other amorphous polymers and indications for side chain crystallization are missing.
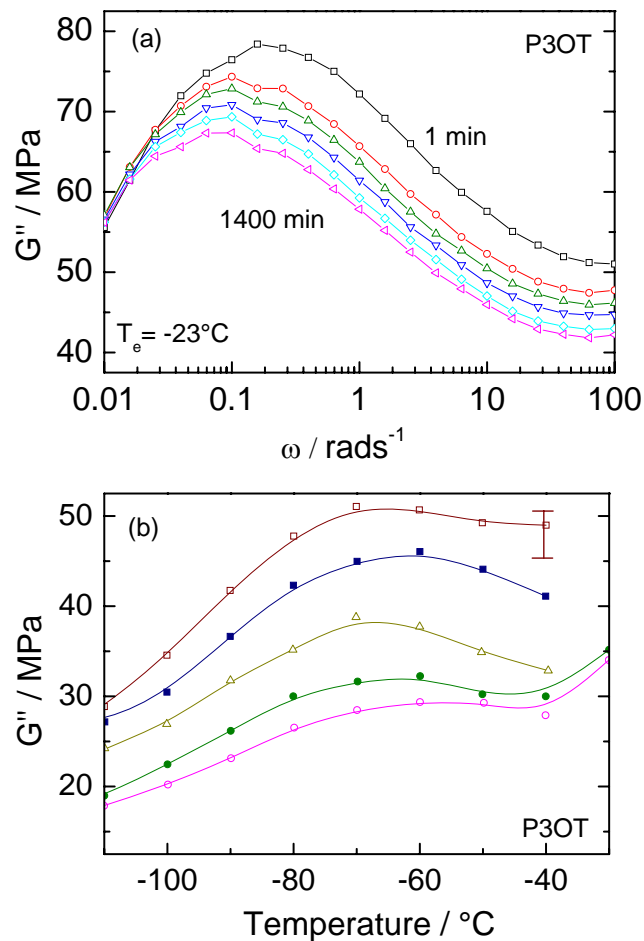
**Figure 8.7:** Shear loss modulus $G''$ vs. angular frequency for regio-random P3OT measured at -23°C. The isotherms are measured after different annealing times at -23°C (1 min, squares; 45 min, circles; 90 min, triangles up; 180 min, triangles down; 360 min, diamonds; 1400 min, triangles left). (b) $G''$ $vs$ temperature curves for P3OT measured at 10 rad/s. Heating (□) and cooling scans taken after 24 hrs annealing at -23°C(○), -27°C (●), -35°C (△) and -40°C(■) are compared. Error bar indicates the reproducibility of the first heating scan after quench.

The results of continuous isothermal shear experiments on P3OT performed at -23°C are shown in Figure 8.7. According to DSC data, the glass temperature of regio-random P3OT should be about -22°C. Considering this situation, physical aging effects would be expected for this sample at -23°C driven by the equilibration tendency of the entire system on logarithmic time scales below $T_g$. Expectedly, the conventional $\alpha$ process in shear data of P3OT moves to lower frequencies during annealing below $T_g$ (Figure 8.7a) as seen in other glasses. More unusual is the observation that (i) this happens at a temperature where the $\alpha$ peak maximum is still in the frequency window of our shear measurements and (ii) that the $\alpha$ peak intensity decreases significantly. These effects are mainly observed on the side of high

frequency wing of $\alpha$ peak. Equilibration effects at 1K below $T_g$ which continue for several hours are also unusual. Normally the equilibration time should be rawly similar to the corresponding $\alpha$ relaxation time which is $\tau_\alpha = 1/\omega_\alpha \approx 10s$ for the given example. $G''(T)$ data measured before and after annealing at -23°C for 24 hours (Figure 8.7b) are compared to check for the effects on the $\alpha_{PE}$ process. It is obvious that the intensity of the $\alpha_{PE}$ process is decreasing in case of P3OT as expected for crystallizing methylene units. The findings for regio-random P3OT correspond qualitatively to those for crystallizable regio-random P3DDT. Similar measurements are performed after annealing at slightly different temperatures, i.e. at $T_e$ = -27, -35 and -40°C. The main trends remain unchanged irrespective of the annealing temperature. Effects are seen in all cases but the decrease of the $\alpha_{PE}$ intensity is less pronounced at lower annealing temperatures as compared to that at higher temperatures. Possibly, this is a consequence of more serious frustration effects far below $T_g$ where the main chains freeze-in.
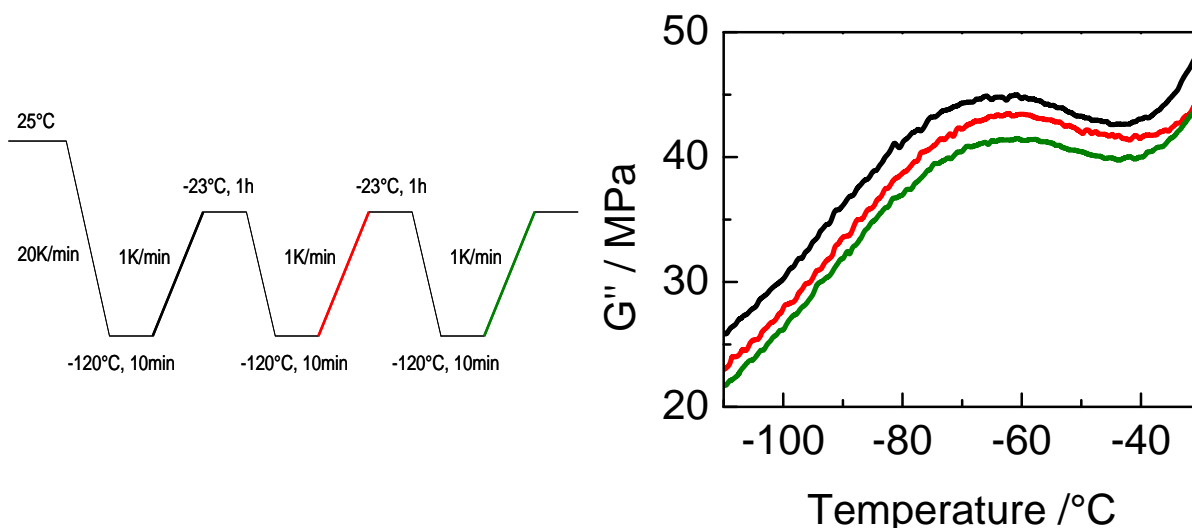


**Figure 8.8:** Shear loss modulus $G''$ $vs$ temperature for regio-random P3OT measured at an angular frequency of 10 rad/s. Heating scans at the rate 1K/min were performed after the quenching the sample from 25°C » $T_g$ to -120°C (black), after 1h annealing (red) and after additional 1h of annealing (green) at $T_e$ = -23°C.

To confirm the systematic decrease in the $\alpha_{PE}$ intensity, cycling measurements were performed with the program as shown in Figure 8.8. With the increase in annealing time, a systematic decrease in the intensity of the $\alpha_{PE}$ process is observed. Note that the peak shape remains basically the same and only the intensity is reduced in agreement with finding for P3DDT.

To check for structural changes during the annealing process, intermediate range (0.2 Å$^{-1}$ ≤
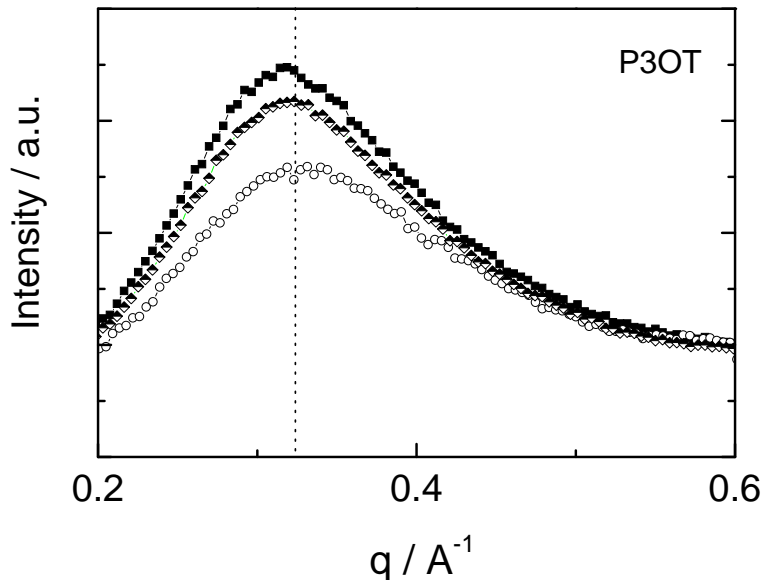
**Figure 8.9:** Scattering pattern $I(q)$ for regio-random P3OT measured at 25°C (open circles) and at -23°C after annealing time of 1 minute (half filled diamonds) and 420 minutes (filled squares) at this temperature.

$q \leq 0.6$ Å$^{-1}$) x-ray scattering measurements were performed to see effects in the pre-peak region. Scattering curves were measured after annealing at -23°C for 1 minute and 420 minutes respectively (Figure 8.9). Note that the curve labeled with $t_e$=1min has been kept at -23°C in total for 30 minutes since this is the accumulation time for obtaining the x-ray diffraction pattern. Obviously, the pre-peak gains intensity during annealing and shifts slightly to lower $q$. These trends are comparable to those observed for regio-random P3DDT crystallized at low temperatures ($T_c$ = -25°C in Figure 7.5).

All annealing experiments on P3OT indicate a densification in the alkyl nanodomains. The time and temperature dependent changes in shear data correspond qualitatively to those observed for crystallizable P3DDT. However, typical features of a truly crystalline sample like a melting peak in DSC scans or a sharp peaks in wide angle diffraction pattern are not observed. Regio-random P3OT may show preordering of the side chains or densification due to physical aging. A certain fraction of rigid amorphous material like known for several other semi-crystalline polymers cannot be ruled out.

## 8.2   Regio-regular poly(3-alkyl thiophenes)

***Regio-regular poly(3-dodecyl thiophenes).*** In chapter 7, it is shown that in regio-regular P3DDT side chain crystallization occurs at room temperature (Figure 7.8). Further isothermal crystallization experiments by DMA were performed at $T_e = 25°C$ for 10100 minutes. The isotherms measured at $T_e$ are presented in Figure 8.10a and b. and show that the storage modulus $G'$ systematically increases while loss modulus $G''$ remains constant. On comparing the isochrones after quenching and isothermally crystallized sample for 7 days at $25°C$, a significant reduction in the intensity of the $\alpha_{PE}$ process occurs without change of the shape while the conventional $\alpha$ process remains more or less unaffected (Figure 8.10c). This result strongly supports side chain crystallization and the occurrence of alkyl nanodomains having an independent dynamics. Reduction of the $\alpha_{PE}$ intensity is obviously related to an increasing number of crystalline $CH_2$ units in the alkyl nanodomains which cannot participate in the cooperative dynamics of the side chains. The results indicate that the degree of crystallinity of the main chain matrix remains basically constant. Most likely the increase in the rubber plateau modulus is due to increase in side chain crystallinity. Comparing the results for regio-random and regio-regular systems, the efficiency of side chain crystallization is small for regio-regular systems. Crystalline main chains obviously slow down the crystallization process within the alkyl nanodomains.
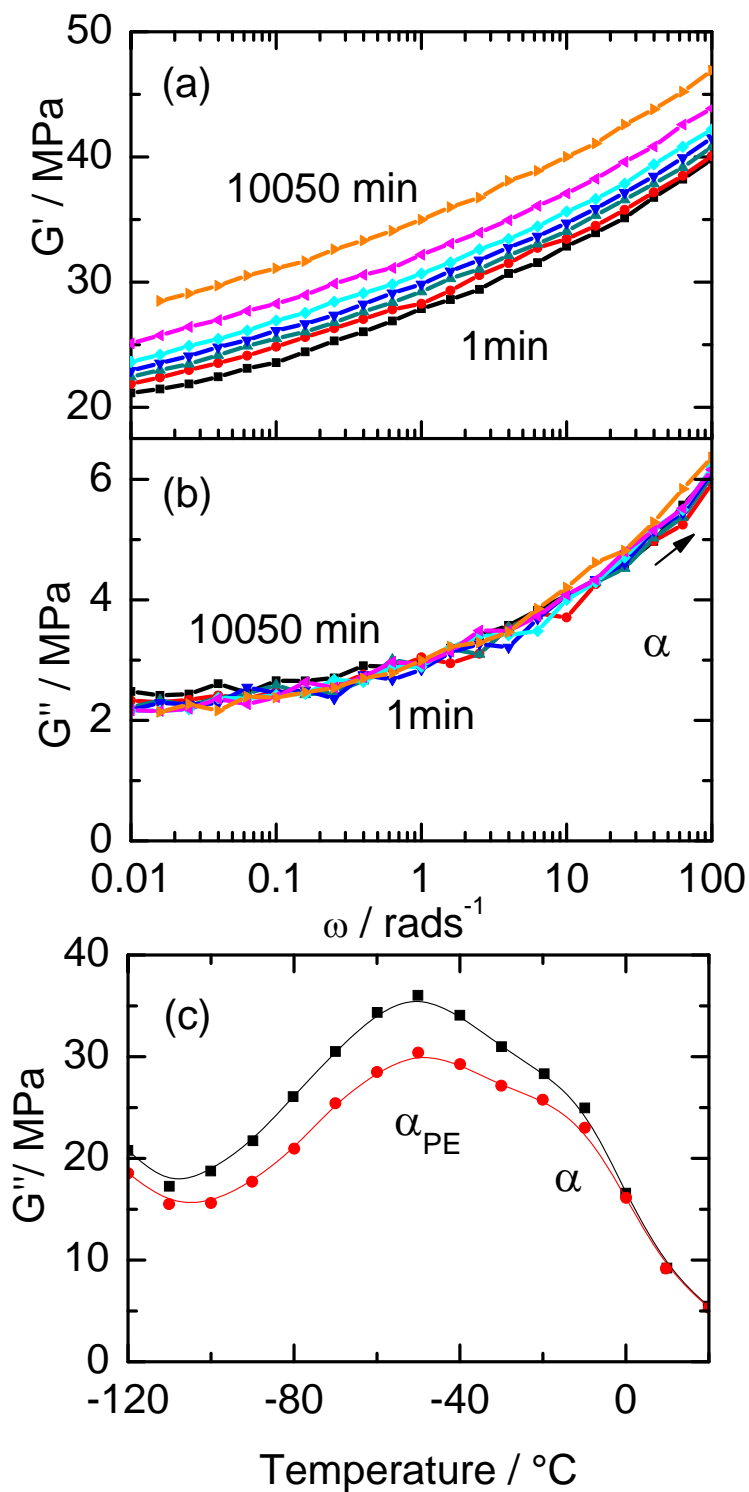
**Figure 8.10:** Dynamic shear storage (a) $G'(\omega)$ and loss (b) $G''(\omega)$ modulus of regio-regular P3DDT measured during isothermal crystallization at 25°C. The crystallization times are 1 (black), 50 (red), 100 (dark cyan), 200 (dark blue), 400 (light blue), 1400 (magenta) and 10050 (orange) minutes respectively. (c) $G''$ $vs$ temperature curves for P3DDT measured at 10 rad/s. Heating ($\square$) and cooling scans ($\circ$) taken before and after 10100 minutes annealing at 25°C are presented.

**Figure 8.11:** (a) DSC heating scans for regio-regular P3OT at the rate of 20K/min after 5 (black) and 1440 minutes (red) annealing of previously quenched samples at $T_e = -23°C$.(b) Glass transition region in DSC hea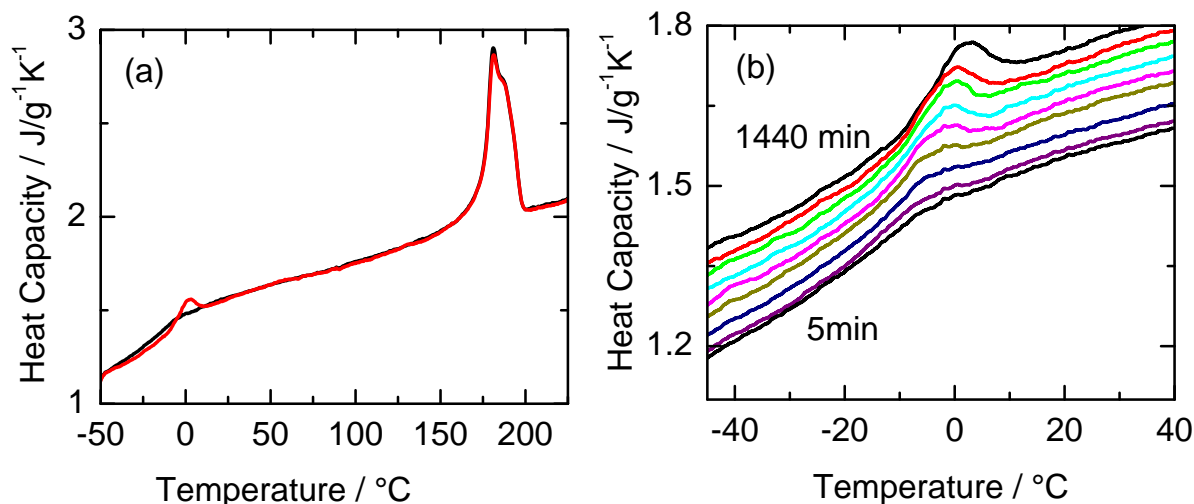ting scans (20K/min) after different annealing times from 5 minutes to 1440 minutes at $T_e = -23°C$. Curves are vertically shifted for the sake of clarity.

***Regio-regular Poly(3-octyl thiophene).*** DSC studies on regio-regular P3OT show that side chain crystallization is practically absent in this sample. Even long annealing times at suitable temperatures do not result in melting peaks in the range 0°C < T <70°C where side chain melting should appear (Figure 8.11a). Annealing at -23°C below $T_g \approx -13°C$ of the amorphous P3OT units leads only to a developing structural relaxation peak slightly above $T_g$ (Figure 8.11b). Whether the unusual shape of the broad overshoot indicates a tiny fraction of crystalline $CH_2$ units melt in the same temperature range is not finally clear. In any case, less than 1% of the $CH_2$ units would be crystalline and the main chain crystallinity is unaffected by this procedure since the melting peak around 190°C is not changing. Considering the glass step, one may assume that about 30 % of the monomeric units in regio-regular P3OT is amorphous since $\Delta C_p(rregP3OT) \approx .075$J/gK compared to $\Delta C_p(rranP3OT) \approx .240$J/gK for fully amorphous regio-random P3OT. Whether this is a suitable estimate remains questionable since the glass step does not appear for all P3ATs in the same temperature range like $T_g$ of the amorphous regio-random P3ATs. Secondly, uncertainities in estimating $\Delta C_p$ are large since it is hard to define appropriate tangents.

Thick melt quenched regio-regular P3OT strips were annealed at $-23°C$ in the DMA instrument. Loss modulus $G''$ isotherms show a shift of the high frequency wing of the $\alpha$ process to lower frequency or longer relaxation times as seen during physical aging of conventional
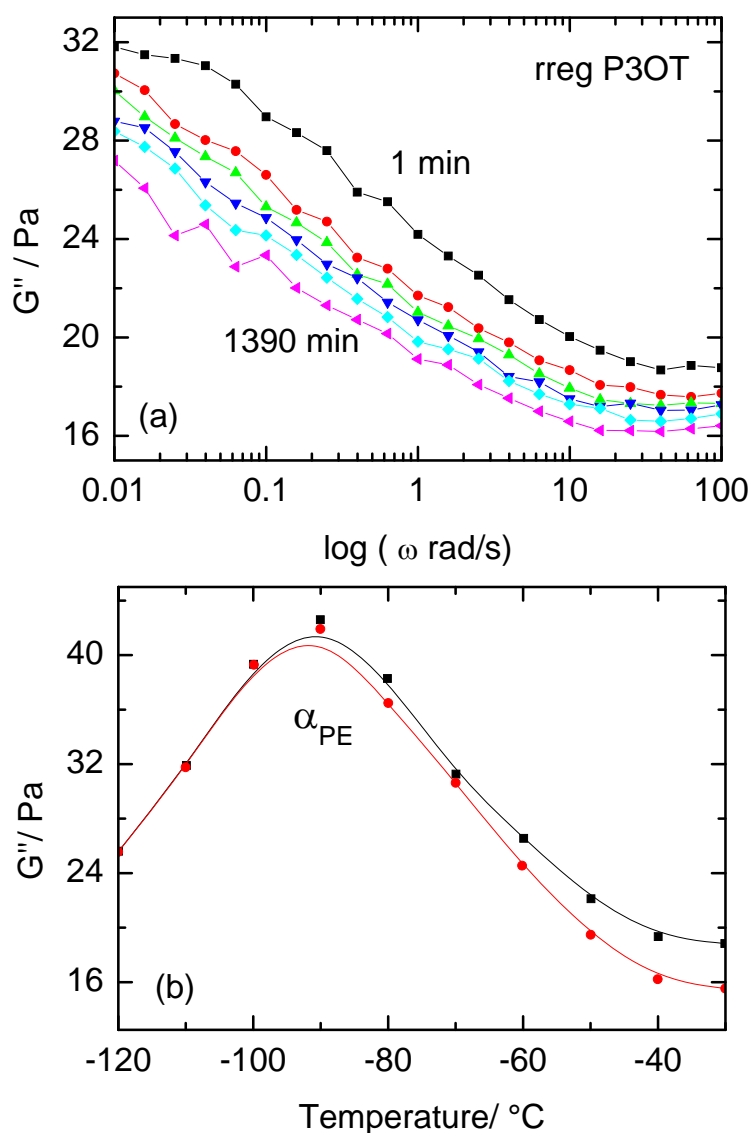
**Figure 8.12:** (a) Shear loss modulus $G''$ vs. angular frequency for regio-regular P3OT measured at -23°C. The isotherms are measured after different annealing times at -23°C (1 (black), 50 (red), 100 (green), 200 (dark blue), 400 (light blue) and 1390 min (magenta). (b) $G''$ $vs$ temperature curves for P3OT measured at 10 rad/s. Initial heating scan(□) and cooling scan (○) taken after 24 hrs annealing at -23°C(○) are compared.

glasses (Figure 8.12a). On comparing the isocrones measured before and after annealing at $-23°C$ for 24h (Figure 8.12b), no significant reduction in the $\alpha_{PE}$ peak intensity is seen and peak shape remains constant indicating no changes in the state of the side chains. This behavior differs from that of regio-random P3OT samples, where significant changes due to physical aging are observed by DSC and DMA. In case of regio-regular P3OT, ordering of the side chains is probably hindered by highly crystalline main chains packed on a lattice which is different from the native lattices of the methylene sequences. In contrast to regio-

regular P3DDT where $CH_2$ units far away from the thiophene backbone can crystallize, the octyl groups are too short to overcome this problem (on the time scales of days). Whether or not densification or crystallization effects in the alkyl nanodomains will appear on much longer time scales remains open at that point. Long term effects in P3ATs and the driving forces responsible for the observed changes will be discussed in sections 9.3 and 9.4.

# Chapter 9

# Discussion

## 9.1 Nanophase separation

Nanophase separation refers to the phenomenon that incompatible main and side chains in polymers with comb-like architecture separate driven by the tendency of the side chains to form nanodomains having sizes in the range 10-30Å. Experimental findings for different P3ATs shown in this work strongly support this physical picture derived originally for other amorphous side chain polymers containing long alkyl groups like PnAMA, PnAA, poly(n-alkyl itaconates) etc. [18, 25, 33] Main arguments for nanophase separation are (i) pre-peaks in the intermediate scattering range and (ii) an independent dynamics in the alkyl nanodomains seen as $\alpha_{PE}$ process in relaxation spectra.

From the structural point of view, results for the investigated series of regio-random poly(3-alkyl thiophenes) are well in accordance with this nanophase separation picture. A pre-peak occurs in the intermediate range x-ray scattering data for all members with more than C=4 alkyl carbons per side chains, which shifts systematically to smaller scattering vectors $q$, if the number of $CH_2$ units per side chain increases. According to the oversimplified structural model shown in Figure 9.1a, this indicates average main chain to main chain distances $d_{nps}$ which are between 16Å for P3HT and 24.5Å for P3DDT. The $d_{nps}$ values are seemingly comparable to that for many other side chain polymers with similar architecture (Figure 9.2a). A sketch visualizing main aspects of the situation in regio-random P3ATs is shown in Figure 9.1b. Based on the average increase $\Delta d_{nps}$ of about 1.4Å per additional $CH_2$ unit and a comparison with the length of fully crystalline $CH_2$ sequences in alkanes (Figure 9.2a) one may conclude that the disordered alkyl groups are basically interdigitated and not too far from an extended conformation. However, the linear increase of $d_{nps}$ with C can also be
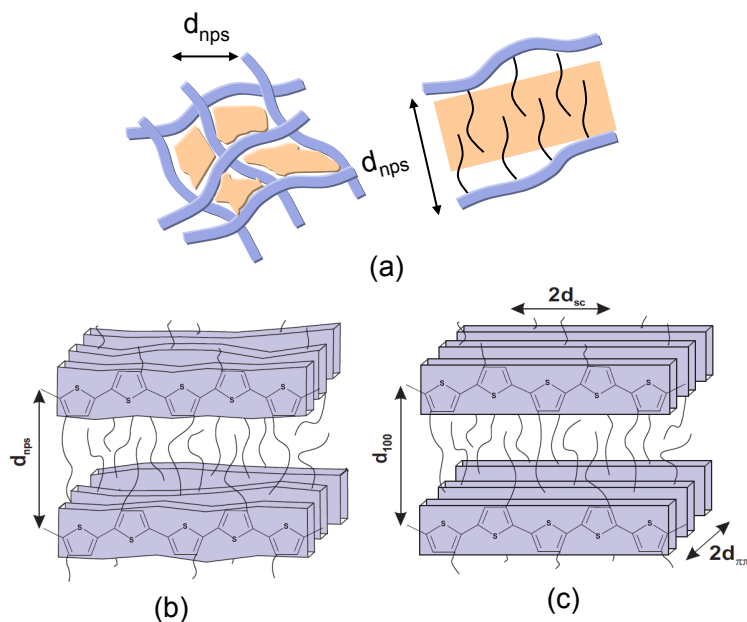
**Figure 9.1:** Sketches showing nanophase separated side-chain polymers. (a) General features of nanophase separated systems seen from a more global (left) and a local perspective (right). Alkyl nanodomains are shown in orange. The main chain to main distances are indicated by $d_{nps}$. More detailed sketches showing the situation in regio-random and regio-regular P3ATs are presented in parts (b) and (c) respectively.
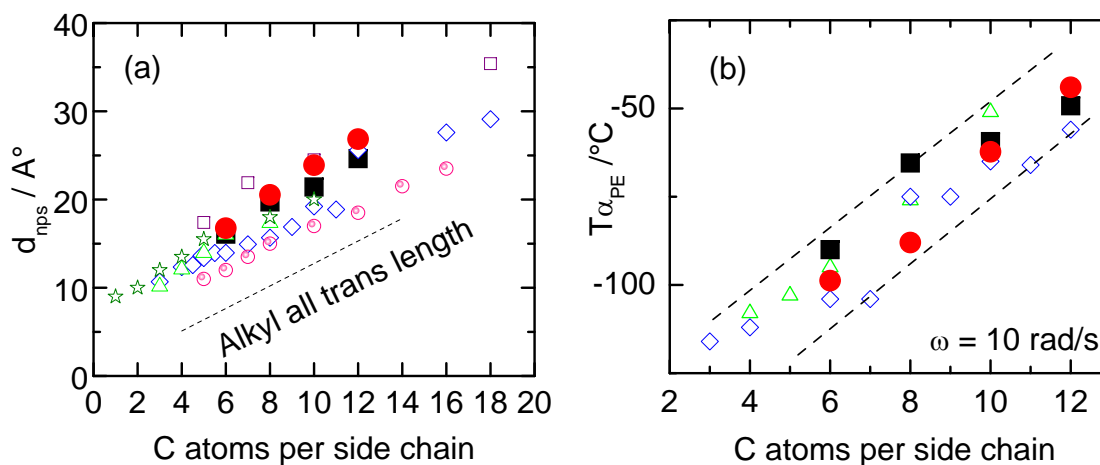


**Figure 9.2:** (a) Equivalent bragg's spacing $d_{nps}$ and (b) relaxation temperatures of the $\alpha_{PE}$ process at $\omega = 10 rad/s$ in the alkyl nanodomains $vs$. $C$ number for regio-regular P3ATs (red spheres) and regio-random P3ATs (squares). Data for poly(n-alkyl methacrylates) (blue diamonds) [18], poly(n-alkyl acrylates) (green triangles) [18], poly (di-n-alkyl itaconates) (hollow dark green stars) [33], poly-1-olefins (hollow spheres) [174] and poly(2-alkylbenzimidazol-alt-thiophene) (purple squares) [175] are shown for comparison.

explained based on simple volume arguments and preserved main chain packing as discussed later in this chapter (section 9.3). For melt quenched regio-random P3ATs, the pre-peak is

relatively broad and the absence of higher orders in these amorphous samples show that the underlying nanostructures are far away from being perfect. The estimated coherence length is small ($d_S \approx 50 - 80$Å) indicating that the structure is in no case a simple arrangement of perfect lamellar stacks. One can also conclude that the phase boundaries are not perfectly defined in regio-random P3ATs. Despite of these facts, there is a strong tendency of the methylene units to form alkyl nanodomains resulting in a periodicity in the range of 10-30Å indicated by pre-peaks in the intermediate range. The situation in regio-regular P3ATs is much more well defined since the thiophene main chains are highly crystalline. Hence, the interfaces are sharper and long range order exists. General features of the packing of main and side chain domains on the mesoscale are quite comparable to those in amorphous nanophase separated systems (cf. Figure 9.1b and c). Even the main chain to main chain distances $d_{100}$ (Figure 9.2a) are comparable to the $d_{nps}$ values observed for regio-random P3ATs with identical side chain length.

From the dynamic point of view, the existence of an independent dynamics in the alkyl nanodomains seen as $\alpha_{PE}$ process in P3ATs which is comparable to that in other side chain polymers with comb-like microstructure is another proof for the existence of nanophase separation (Figure 9.2b). An important finding of this work is that the $\alpha_{PE}$ process is observed for regio-regular P3ATs with highly crystalline main chains at the same frequency-temperature position and with the similar intensity like in fully amorphous regio-random P3ATs. This suggests that the alkyl groups in lower regio-regular P3ATs ($C \leq 12$) are disordered and that their dynamics is basically independent on the state of the main chains. This finding is in accordance with the $V_{CH2}$ values shown in section 5.2 indicating a high degree of amorphicity. Obviously, the crystallization of methylene sequences close to the backbone is prevented in systems with highly crystalline as well as glass like disordered thiophene rings. Frustration effects seem to occur in both cases. In regio-regular P3ATs, this seems to be a consequence of the fact that the native lattice of the main chains does not fit to that of the methylene sequences. The surprising observation is that the $\alpha_{PE}$ process in regio-random and regio-regular P3ATs are similar indicating a high degree of independence of the alkyl nanodomains. [1]

Summarizing this part, one can conclude that the results in this work clearly support a separation of main and side chains in amorphous regio-random as well as semi-crystalline regio-

---

[1]Note that our results contradict somehow the definition of nanophases given by Wunderlich [176] stating that nanophases are characterized by certain influence of the surfaces on its properties; whereas our findings show that the dynamics in alkyl nanodomains remain unaffected by the state of confining thiophene rings as well as the microstructure of main chains in general.(Figure 9.2a and b)

regular P3ATs. This is well in line with the nanophase separation picture developed previously. [18] Further support for this model came recently from detailed neutron scattering experiments [19] on selectively deuterated PnAMAs as well as from solid state NMR studies [177] on PnAMAs. The results of both studies nicely confirm the existence of alkyl nanodomains with well defined dimensions in the range 10-30Å depending on side chain length and an independent dynamics therein which will be the focus of next section.

## 9.2   Dynamics under confinement

Dynamic shear measurements on the series of regio-random and regio-regular P3ATs in this work show that two independent relaxation processes with a typical features of dynamic glass transition appear in both series. The high temperature $\alpha$ process corresponding to cooperative motions incorporating the thiophene main chains shifts to low temperatures primarily due to internal plasticization of backbones by highly mobile $CH_2$ units in their environment. This is well known phenomenon and found for many series of side chain polymers containing alkyl group since Heijboer discovered this effect for PnAMAs in the 1960s. [161] More interesting and focus of this work is the low temperature process $\alpha_{PE}$ corresponding to the motions within alkyl nanodomains with different size. The $\alpha_{PE}$ process, which is found interestingly in regio-random and regio-regular P3ATs, shows very systematic trends regarding relaxation temperature $T_{\alpha_{PE}}$ and fragility $m_{\alpha_{PE}}$ if side chain length $C$ and alkyl nanodomain size $d_{nps}$ are varied. This is seemingly an extremely interesting situation to study the dependence of cooperative motions on domain size and early stages of cooperativity. A special advantage here is that the $\alpha_{PE}$ process in regio-regular P3ATs appears in alkyl nanodomains with well defined crystalline interfaces which allows a density estimation for the alkyl nanodomains. The relaxation temperature of the $\alpha_{PE}$ process (Figure 9.2b) systematically shifts to higher temperatures with the systematic increase in the domain size (Figure 9.2a). The shifts are of the order of 40K. The $\alpha_{PE}$ process for P3HT appears at $-90°C$ and is shifted to $-49°C$ for P3DDT member.

Steepness or fragility index for the $\alpha_{PE}$ process $m_{\alpha PE}$ increases systematically with increasing number of carbons per side chain $C$ and alkyl nanodomain size $d_{nps}$ or $d_{100}$ like for other series of nanophase-separated side chain polymers (Figure 9.3). [18] This corresponds to a transition from Arrhenius to non-Arrhenius behavior. Large $m_{\alpha PE}$ values for P3ATs with long alkyl groups can be understood as a clear hint for a cooperative nature of the underlying $\alpha_{PE}$ motions in the alkyl nanodomains. Arrhenius-like behavior with $m_{\alpha PE} \approx m_{\beta PE} \approx 13$ corresponding to more localized Johari-Goldstein like motions, i.e.,
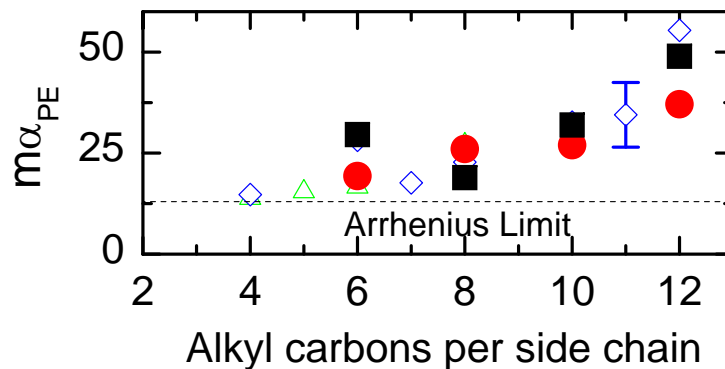
**Figure 9.3:** Steepness index $m_{\omega,\alpha PE}$ *vs.* $C$ number for regio-regular P3ATs (spheres) and regio-random P3ATs (squares). Data for poly(n-alkyl methacrylates) (diamonds) and poly(n-alkyl acrylates) (triangles) are taken from [18] are shown for comparison.

a $\beta_{PE}$ process as discussed recently for poly(n-alkyl methacrylates) with short side chains (C=4 and 5) [108, 164, 178] is approached for P3HT. In this sense, fragility index $m_{\alpha_{PE}}$ confirms the cooperativity of the motions within the alkyl nanodomains of higher P3ATs ($C \geq 6$) reflected by an $\alpha_{PE}$ process with typical feature of dynamic glass transition.

As discussed previously in chapter 2, there are different factors influencing the cooperative dynamics under nanoscopic confinement. Main routes of explanation are (i) purely geometrical confinement due to finite size, (ii) density changes in small domains and (iii) effects of constraints produced by interfaces. The discussion in this section is focused on the first two points (i) and (ii) since the interfaces of the alkyl nanodomains are practically identical as indicated by nearly identical lattice parameters for the crystalline main chains in regio-regular P3ATs. The hindered glass transition picture describing finite size effects on the cooperative dynamics, possible effects of density and predictions of the coupling model describing interrelations between local $\beta_{PE}$ and cooperative $\alpha_{PE}$ processes will be discussed below.

***Hindered glass transition approach***: The systematic shifts in $\alpha_{PE}$ relaxation temperature $T_{\alpha_{PE}}$ and fragility $m_{\alpha_{PE}}$ discussed above can be qualitatively explained with the help of the hindered glass transition picture as proposed by Donth. [65] According to this picture, changes in the cooperative dynamics are expected when the size of the confinement is comparable to that of the cooperatively rearranging regions $\xi_\alpha$ which is the characteristic length scale for the cooperative dynamics in the corresponding bulk system, i.e. when $d_a \approx \xi_\alpha$. Deviations from the bulk dynamics should appear for small domain sizes at higher temperatures since CRRs cannot grow further with reducing the temperature as shown in Figure 9.4. [7,75]
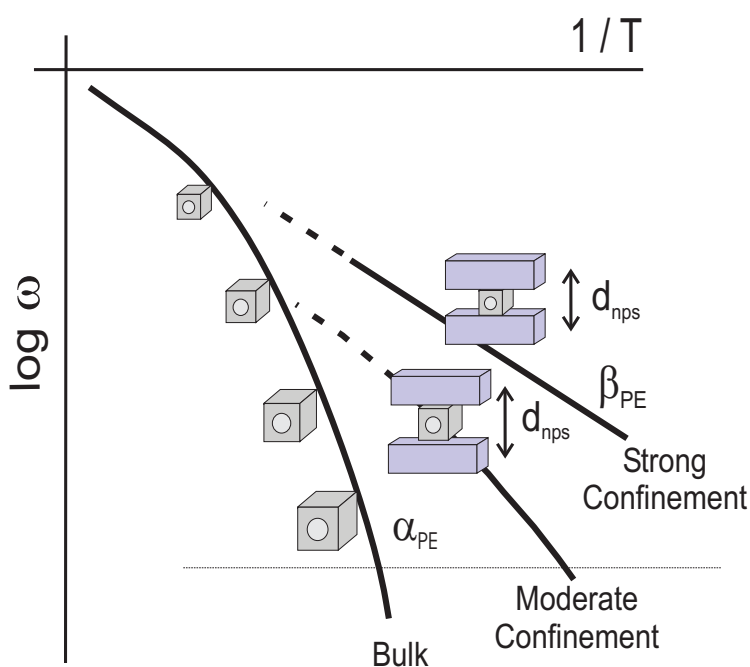
**Figure 9.4:** Scheme showing the predictions of the hindered glass transition picture for the cooperative dynamics of confined systems.

A point which should be highlighted here is that the dynamics is always faster under confinement as compared to the bulk according to this approach. Further, it is predicted that the reduction of the relaxation temperature is accompanied by a non-Arrhenius to Arrhenius transition with decreasing domain size. This corresponds quite well to the findings for the $\alpha_{PE}$ process in alkyl nanodomain with different size. For small confinements corresponding to P3HT with alkyl nanodomain size $d_a \approx 10$Å, a faster $\alpha_{PE}$ dynamics is observed which has similar features like the Johari-Goldstein $\beta_{PE}$ process, while for P3DDTs with $d_a \approx 21$Å, a truly cooperative $\alpha_{PE}$ process with non-Arrhenius like temperature-dependence occurs. This shows that the geometrical confinement effects in domains with typical dimensions of 10-30 Å are a suitable explanation for the systematic changes of the $\alpha_{PE}$ in P3ATs with different side chain lengths. Similar effects are also seen for glass forming liquids confined in the nanoporous host systems with pore diameters less than 100Å (cf. section 2.2).

***Density Effects***: Another parameter which strongly affects the cooperative dynamics is density. For confined systems, it is usually difficult to decide whether or not changes in the density are responsible for changes in the cooperative dynamics as it is often impossible to measure the densities of confined glass formers. An advantage of P3ATs chosen as model system in this work is that average density of the alkyl nanodomains can be estimated based on crys-

tallographic information for regio-regular samples with highly crystalline main chains.
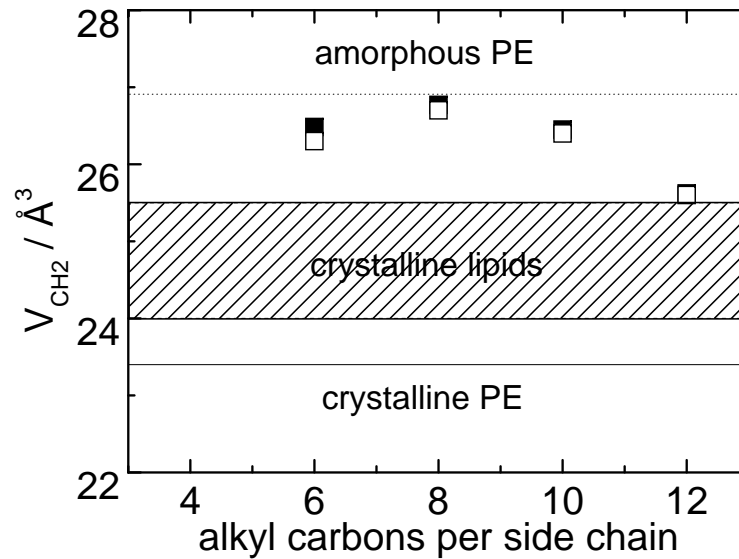


**Figure 9.5:** Average volume per methylene unit $V_{CH2}$ *vs.* number of alkyl carbons per side chain $C$ for regio-regular P3ATs. Full symbols are the results from calculations based on our data given in Table 5.2 of section 5.2. Open symbols corresponds to calculations based on data reported in Ref. [146]. $V_{CH2}$ values for crystalline polyethylene (solid line), [118] amorphous polyethylene (dotted line) [179] and crystalline methylene units in lipids (shadowed area) [163] are given for comparison. All values are for ambient conditions.

Volumina per $CH_2$ unit $V_{CH2}$ estimated using the lattice parameters from x-ray scattering experiments (section 5.2) are plotted for different side chain lengths in Figure 9.5. Main finding is that $V_{CH2}$ is basically independent on side chain length. A certain reduction for P3DDT (C=12) might be related to a tiny fraction of crystalline $CH_2$ units as discussed in section 9.3. As the volume $V_{CH2}$ is basically constant, it is unlikely that density effects are responsible for the 40K shift of the $\alpha_{PE}$ process with the increasing side chain lengths accompanied by a systematic transition from Arrhenius like to non-Arrhenius behavior. The results strongly indicate that the finite size effects dominate and that a conflict between CRRs and alkyl nanodomain size is the most appropriate explanation for the observed changes in the $\alpha_{PE}$ process with side chain lengths.

***Coupling Model predictions.*** K.L Ngai proposed an approach called (extended) Coupling Model which is connecting the degree of cooperativity of the $\alpha$ process (intermolecular coupling) with the ratio of $\alpha$ and $\beta$ relaxation times and makes a correlation of it to the steepness or fragility index $m_\alpha$. [9, 164, 181] The idea introduced is that the relaxation is initiated by
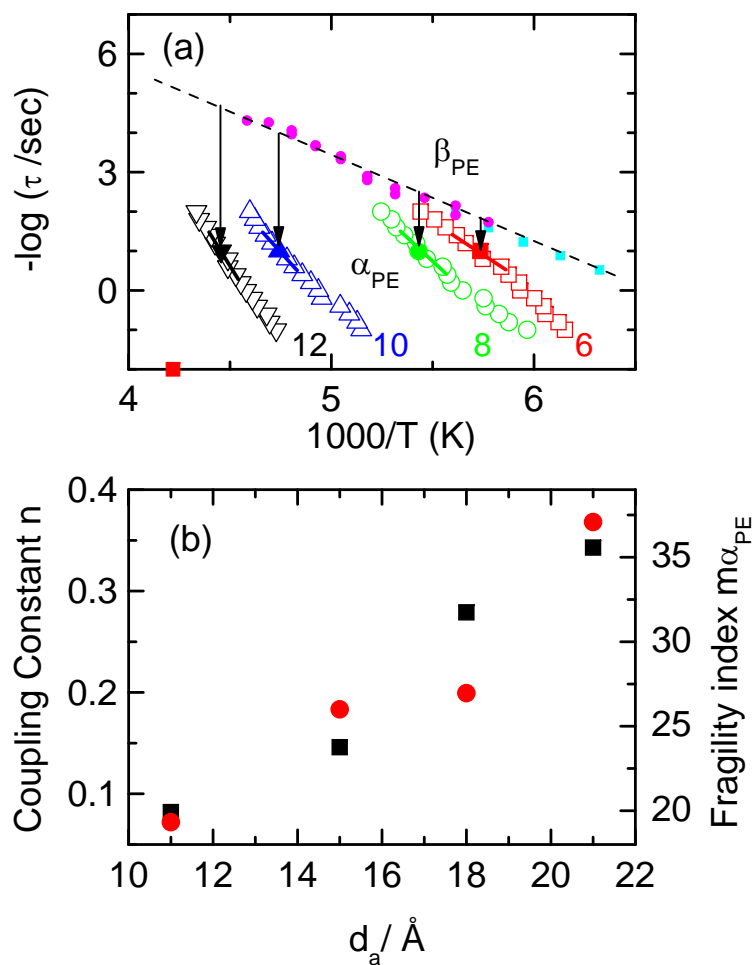
**Figure 9.6:** (a) Arrhenius plot for the relaxation times $\tau_{\alpha_{PE}}$ for regio-regular samples for C= 6, 8, 10 and 12. Vertical lines connects $\alpha_{PE}$ relaxation time at 1/10s to the corresponding $\beta_{PE}$. $\beta_{PE}$ are taken from [18] Red point corresponds to bulk glass transition for bulk polyethylene taken from [180]. (b) Coupling parameter n (squares) and fragility index $m_{\alpha_{PE}}$ (circles) $vs.$ $d_a$ for regio-regular systems at relaxation time of 1/10s. $d_a$ was calculated by $d_a = d_{100} - 6$Å.

a local primitive process (JG $\beta$ process) which over the passage of time evolves as a cooperative $\alpha$ process which is many molecule in nature and dynamically heterogeneous. The cooperative $\alpha$ process which shows intrinsic broadening can be modeled by a Kohlrausch-Williams-Watts (KWW) function (equation 2.1) where the exponent $\beta_{KWW}$ is related to coupling constant n as $\beta_{KWW} = 1 - n$. The equation of coupling model relating the $\alpha$ and $\beta$ relaxation times is

$$\tau_\alpha = (t_c^{-n}\tau_\beta)^{1/(1-n)} \tag{9.1}$$

where $\tau_\alpha$, $t_c$,$\tau_\beta$ and n are alpha relaxation time, crossover time which is approximated to be

around $2 \times 10^{-12} s$ for conventional glass forming liquids, primitive relaxation time equivalent to the $\beta$ relaxation time and the coupling constant. For a conventional $\beta$ relaxator, value of $n$ is assumed equal to 0 since localized motions are non cooperative in nature. Developing cooperativity leads to an increase of the value of $n$. For conventional bulk-like glass forming materials like different small molecular liquids as well as polymer at thermal glass transition $n$ is often $\approx 0.5$. [165, 181]

In figure 9.6a, the coupling model is applied to the $\alpha_{PE}$ processes for regio-regular P3ATs studied in this work. Coupling parameter $n$ as a measure of cooperativity can be calculated knowing the average $\alpha_{PE}$ relaxation time $\tau_{\alpha_{PE}}$ and the relaxation time of corresponding JG process $\tau_{\beta_{PE}}$ at the same temperature. In our case, $n$ values for $\tau_{\alpha_{PE}} = 0.1s$ are estimated. The $\tau_{\beta_{PE}}$ values are estimated based on the data for poly(n-alkyl acrylates) with short side chains (C=4 and 5) assuming that the dynamics within the alkyl nanodomains is similar for all series of nanophase separated side chain polymers. Vertical lines in Figure 9.6a connect the $\tau_{\alpha_{PE}}$ with the corresponding $\tau_{\beta_{PE}}$ value which were used to calculate $n$. The coupling parameter $n$ are plotted against alkyl nanodomain size $d_a = d_{100} - 6\text{Å}$ in figure 9.6b. Smaller $n$ values correspond to more localized motions while large $n$ values correspond to highly cooperative motions. Figure 9.6b shows clearly that the coupling parameter $n$ increases systematically with the increase in alkyl nanodomain size $d_a$. In the framework of the coupling model, this implies that the cooperativity of the $\alpha_{PE}$ process is larger in larger nanodomains. The cooperativity $n$ of the $\alpha_{PE}$ process in P3DDT (C=12) is comparable to that of classical glass former at $T_g$ in the bulk since a large number of particles ($CH_2$ units) are accessible in the alkyl nanodomains. On contrary for P3HT (C=6), the small coupling parameter indicates weak cooperativity due to the fact that less particles are accessible in smaller alkyl nanodomains. In that sense, the coupling model predicts, like the hindered glass transition picture, decreasing cooperativity with decreasing alkyl nanodomain size $d_a$ and gives an explanation for the observed changes in $T_{\alpha_{PE}}$ and $m_{\alpha_{PE}}$ with side chain length. Fragility which is somehow another measure of determining cooperativity also points to the same trend (Figure 9.6b).

Note that it is hard to get detailed information about the Kohlrausch exponent $\beta_{KWW}$ from isothermal shear data due to a strong overlap of $\alpha$ and $\alpha_{PE}$ relaxation processes. A deconvolution of both processes would be required to crosscheck the predictions of coupling model for $\beta_{KWW}$. Values between 0.92 and 0.66 would be expected in the temperature range where $\tau_{\alpha_{PE}} = 0.1s$ for P3HT and P3DDT respectively. The $\alpha_{PE}$ process appears to be broad in all samples. Apart from intermolecular coupling, density gradients in the samples and the

distribution of the domain sizes may have an influence.

Summarizing this section, one can conclude that geometrical confinement effects due to the conflict of CRR and alkyl nanodomain size is seemingly the most appropriate explanation for the observed changes in relaxation temperature $T_{\alpha_{PE}}$ and fragility $m_{\alpha_{PE}}$ of the $\alpha_{PE}$ process with side chain lengths in P3ATs. Changes of the average density of the alkyl nanodomains seem to be of minor importance. The results indicate the existence of CRRs and typical CRR sizes in the range 10-30Å. This seems to be an interesting and important finding in the light of recent discussions where CRR sizes between a few angstroms to few tens of nanometers have been reported. Other approaches like the coupling model also predict that the inter-molecular cooperativity of the $\alpha_{PE}$ process is increasing with increasing alkyl nanodomain size. In a way, intermolecular cooperativity seems to be the key to understand systematic changes in $T_g$ and fragility under confinement.

## 9.3   Side chain crystallization and polymorphism in alkyl nanodomains

### *Requirements for side chain crystallization*

From a comparison of shear, DSC and x-ray scattering data for regio-regular and regio-random P3ATs in our study, one can conclude that the alkyl nanodomains in melt quenched samples with $6 \leq C \leq 10$ and high molecular weight are basically amorphous. There are no significant melting peaks in DSC scans at low temperatures and the polyethylene-like glass transitions $\alpha_{PE}$ for regio-regular and regio-random P3ATs with identical side chain length have comparable intensity and shape. A comparison of $V_{CH2}$ values for alkyl side chains of thiophenes with that of crystalline polyethylene and crystalline lipids shows that the density of the latter is much larger indicating amorphicity of the alkyl side chains. Amorphicity of the alkyl nanodomains in regio-regular and regio-random P3ATs with $6 \leq C \leq 10$ can be explained by the fact that the alkyl groups in both series are frustrated by immobile thio-phene rings in their environment. The thiophene domains are highly immobile at suitable crystallization temperatures for the alkyl nanodomains leading to constraints. The thiophene domains in regio-random P3ATs are in a glassy or at least in a highly viscous state due to freezing-in at the glass temperature $T_g$, while they are crystalline in regio-regular P3ATs. Thus, the attachment points of the alkyl groups to the main chains do not sit on a crystalline lattice in the first case while they are fixed to the lattice formed by the thiophene rings in the

latter case. Consequently, the methylene units close to the thiophene nanodomains can not pack easily on their own native lattice.

Corresponding to this picture, side chain crystallization is usually only observed if the alkyl groups are long and flexible enough to compensate frustration effects introduced by the main chains. [51] Crystallization of methylene sequences in the middle of the alkyl nanodomains is indicated by a nearly linear increase of crystallinity with side chain length above a certain minimum number of $CH_2$ units for PnAMAs and other side chain polymer series. [53] Similar behavior is indicated for regio-random and regio-regular P3ATs where side chain crystallization is only seen for $C \geq 10$ alkyl carbons per side chain. Melting peaks in DSC heating scans are only observed for P3DDT (C=12) samples and to a minor extent for P3DT (C=10) after extremely long annealing time. However, the melting enthalpy $\Delta H_{CH2}$ is always small indicating that only a tiny fraction of the methylene units is crystalline. This corresponds to the findings for other nanophase-separated side chain polymers where crystallization of alkyl groups starts to appear at comparable length ($C \approx 12$). [53] Crystallization of methylene sequences close to the backbone driven by that of the thiophene rings is unlikely from that perspective. Moreover, the intensities of the $\alpha_{PE}$ processes in regio-random and regio-regular P3ATs are quite comparable showing that main chain induced crystallization is not appearing. Thiophene and alkyl nanocrystals in higher regio-regular P3ATs (e.g. P3DDT) are obviously decoupled by a short amorphous methylene spacer required to compensate their lattice mismatch. A similar spacer should exist between alkyl crystals and glassy main chain domains in higher regio-random P3ATs like in many other semi-crystalline side chain polymers.

### Polymorphism in alkyl nanodomains

*Regio-random P3DDT.* As discussed above, alkyl groups in higher poly(3-alkyl thiophenes) can crystallize within self assembled alkyl nanodomains. The methylene units can crystallize hereby interestingly in different polymorphic forms which can even exist in parallel like seen for regio-random P3DDT and P3DT. Such a behavior has not been reported to our knowledge for other side chain polymers containing alkyl groups with similar length. Transitions between two polymorphs with hexagonally and orthorhombically packed alkyl groups have been only reported for a few side chain polymers like eicosylated polyethyleneimine etc containing 18 or more alkyl carbons per monomeric unit. [128]

The results of isothermal crystallization experiments on regio-random P3DDT and P3DT

indicate that the crystallization mechanism is strongly influenced by the crystallization tem-
perature (Figure 7.2 and 7.7). The similarity of melting and crystallization temperatures to
those reported for alkanes [168, 182] and other side chain polymers containing alkyl groups
with comparable length [53, 128] implies that side chain crystallization occurs in P3ATs near
room temperature and below. A crystallization mechanism incorporating main chains like in
regio-regular P3ATs seems to be unlikely since the melting temperatures of such crystals are
usually much higher ($150°C \leq T_m \leq 250°C$). Apart from the $T_m$ argument, the proposed
side chain crystallization picture is supported by indirect arguments coming from x-ray scat-
tering measurements. These experiments show clearly that regio-random P3DDT behaves
like other polymers undergoing side chain crystallization (Figure 7.2-7.5). A straightfor-
ward interpretation of the three distinct melting peaks observed for P3DDT is therefore to
assume that three different forms of side chain crystals exist. It would be very interesting if
methylene sequences in the hexagonal, orthorhombic and triclinic form (known from differ-
ent alkanes [125, 168, 183]) would appear in alkyl nanodomains of regio-random P3DDT. A
crystallographic analysis is unfortunately impossible since the degree of crystallinity is too
small for the investigated samples ($C \leq 12$). The observed differences in $T_m$ are of the right
order of magnitude. An alternative interpretation based on different crystal sizes seems not
really reasonable, since one has to explain then why three distinct crystal thicknesses should
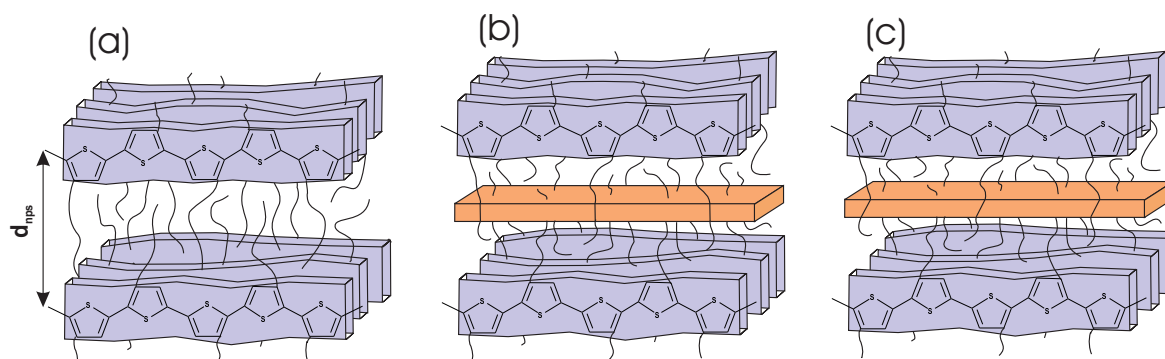appear, which can even coexist under certain conditions.



**Figure 9.7:** Schematic picture showing the possible packing of thiophene main chains and alkyl groups (bold
lines) in regio-random P3DDT (a) in the non-crystalline state, (b) after low temperature crystallization at -25°C
(= form III) and (c) high temperature crystallization at room temperature (= form I).

As already mentioned, it is not possible to get substantial information about the packing of
the side chain crystals from x-ray diffraction experiments in the wide angle range since the
number of crystalline $CH_2$ units is small compared to those in the disordered state. Hence,
the scattering pattern is dominated by an amorphous halo. However, appearance of struc-

tural changes can be concluded from the observation that the average main chain to main chain distances $d_{nps}$ for the three phases are different. Low temperature crystallization ($T_c$=-25°C) leads to an increase of $d_{nps}$ compared to a disordered state while $d_{nps}$ decreases if regio-random P3DDT is crystallized at high temperatures ($T_c$=26°C) (Figure 7.5). In a hypothetical picture as shown in Figure 9.7, this can be explained based on differently packed side chains. Idea is that packing of the alkyl stems in the crystalline layers might be responsible for changes in $d_{nps}$. The increase of $d_{nps}$ in case of form III of P3DDT growing at -25°C might be due to an increasing all trans content in the alkyl groups during crystallization pushing the main chains to separate (Figure 9.7b). The same trend occurs in higher poly(n-alkyl methacrylates) like PODMA containing hexagonally packed methylene sequences. [51] Although, $d_{nps}$ increases during crystallization, the average mass density $\rho$ can increase since the distance between the alkyl stems in the lateral direction decreases. The opposite trend in $d_{nps}$ found for form I of regio-random P3DDT growing at 26°C might be related to a certain tilt of the crystalline (all-trans) sequences in the crystalline alkyl layers (Figure 9.7c). Whether the tilt occurs in-plane like shown in Figure 9.7c or out-of-plane or in both directions can not be decided based on our experimental data. Speculatively, this question plays a certain role for the appearance of a third polymorphic state (form II) in regio-random P3DDT. In general, the finding that $d_{nps}$ changes due to crystallization is compatible with the interpretation that differently packed alkyl groups are responsible for the occurrence of three polymorphic states for regio-random P3DDT. Whether or not the existence of sequences with different regio-regularities along the main chain is important for this peculiar phenomenon is not finally clear yet.

A common observation for all investigated crystallization conditions and crystal forms is that the melting temperature increases slightly but systematically with increasing heat of fusion $\Delta H_m$ (Figure 7.2). Similar behavior has been found for the secondary crystallization in many other side chain polymers containing long alkyl sequences (e.g. poly(n-octadecyl methacrylate [53]) and attributed to crystal thickening according to Gibbs-Thomson equation which predicts $T_m \propto d^{-1}$. In most of these cases, a pronounced step in the $D_c$ vs. $\log t_c$ curves appears for shorter times which has been interpreted as primary crystallization step. This step is practically absent in the data for P3DDT shown in Figure 7.3. A possible scenario to explain this behavior might be to assume that (i) an extremely thin crystalline layer is growing laterally in the alkyl nanodomains of regio-random P3DDT and that (ii) this crystalline layer starts immediately to thicken. The ratio of the time constants for both processes determines then the curve shape in a $D_c$ vs. $\log t_c$ plot.

*Regio-regular P3DDT.* For differently treated regio-regular P3DDT samples, prominent melting peaks in the DSC scans are observed at around $40°$C and at around $55°$C (Figure 7.8). Over long period of time at room temperature, the intensity of the peak at $40°$C grows showing a slight increase in degree of crystallinity while the peak at $55°$C remains unaffected. This may indicate the existence of different polymorphic forms regarding the side chain crystals in regio-regular P3DDT similar to the findings for regio-random P3DDT. The peak at $40°$C appears at a position where form I is seen in regio-random P3DDT also confirming side chain crystallization. Along with the low temperature melting peaks, high temperature melting peaks at around $150°$C are observed corresponding to main chain melting. This finding indicates the coexistence of two crystallizable phases. In some sense, the crystallization of the side chains appears independently from that of the thiophene main chains and vice-versa. One point which should be noted is that changes in the crystalline state of the side chains seemingly affects the main chain crystals as indicated by changes in the trimodal peak in the temperature range 140-170°C due to side chain crystallization near $25°C$. This indicates that their is certain competition of main and side chain crystallization which could be important for the appearance of different polymorphs in P3ATs. Whether the main chains show polymorphism by themselves or the trimodal melting peak at high temperatures is related to other effects is not yet clear. Further measurements should be performed clarifying the details of the complex structure formation process in such systems with two crystalline subunits. Experiments on P3ATs with long alkyl groups (C $>>$ 12) would surely be interesting in this context. Considering the thermodynamic situation, two crystallization tendencies seem to compete in regio-regular P3ATs (C > 10) leading to non-equilibrium effects which are driving force for long term equilibration processes near room temperature as discussed in the next section 9.4.

### *General aspects and classification scheme*

Considering the mesoscopic structure of regio-random and regio-regular P3ATs studied in this work, there are common aspects as well as differences resulting from the fact that the crystallization tendency of thiophene and methylene subunits is strongly depending on the microstructure of polymer chain and monomers. A common observation is that in all investigated P3ATs separation of thiophene main chains and alkyl side chains occurs on the mesoscale (section 9.1). Depending on the microstructure of polymer chain and monomers, four different cases as shown in Figure 9.8 have been observed which can be understood as a classification scheme rationalizing the situation in nanophase-separated side chain polymers with crystallizable main and/or side chain parts. There are systems where (i) side chains as

well as mains are amorphous **(mAsA)** like in melt-quenched regio-random P3ATs with short alkyl groups ($6 \leq C \leq 10$), (ii) the side chains are partly crystalline but the main chains are amorphous **(mAsC)** like in regio-random P3DDT ($C = 12$), (iii) crystalline main chains are combined with amorphous side chains **(mCsA)** like present in lower regio-regular P3ATs with $6 \leq C \leq 10$, or (iv) crystalline main chains combined with partly crystalline side chains **(mCsC)** like observed for regio-regular P3DDT ($C = 12$). Expectedly, the long range order of the superstructure on the mesoscale is pronounced in case **(mCsC)** and suppressed in case **(mAsA)**. Interestingly, long range order is also found for the cases **(mCsA)** and **(mAsC)**, where only one of the two subunits is (partly) crystalline. The occurrence of an ideal crystal, where both subunits are packed on one and the same lattice is not observed and seems to be unlikely for nanophase-separated polymers with comb-like architecture since this requires an optimal microstructure without lattice mismatch of the subunits or a full compensation of the lattice mismatch. Whether or not this case of fully crystalline main and side chains is really existing seems to be open. Such an ideal crystal would avoid the competition of two crystallization tendencies being a main reason for pronounced long term effects which seems to be characteristic for **(mCsC)** systems. Contributions from both parts of the monomeric units will determine the final structure which must not be a priori an equilibrium state but might be also influenced by kinetic aspects as discussed for other semi-crystalline polymers. [184] The situation in block copolymers composed of two crystallizable components is characterized by similar effects. [185]

An important question which is often discussed in the literature about regio-regular P3ATs is how the methylene sequences in the alkyl nanodomains are packed and how this influences their properties. It is still controversially debated whether the side chains are 'partly interdigitated' or 'non-interdigitated and tilted' and whether they are ordered (all trans) or in 'disordered' state. [38, 157, 186] An interesting result in this context is that the volume per $CH_2$ unit is independent on side chain length C. Another well known fact is that the thiophene main chains ($d_{\pi\pi}$) is only slightly affected by the side chain length (section 5.2). Both findings together can explain the linear dependence of $d_{100}$ on C despite of any discussion about interdigitation and conformation (trans content) of the side chains. If the main chain packing is preserved, each additional $CH_2$ unit in the side chain having a volume $V_{CH2}$ will linearly increase the main chain to main chain distance $d_{100}$. The explanation based on the simple volume argument is quite useful in case of amorphous side chains and also explains why statistical copolymers made of 3-alkyl thiophene comonomers with different side chain lengths show intermediate $d_{100}$ values. [160] The main chain to main chain distance $d_{100}$ will grow with the average side chain length since the number of $CH_2$ units will determine $d_{100}$ as
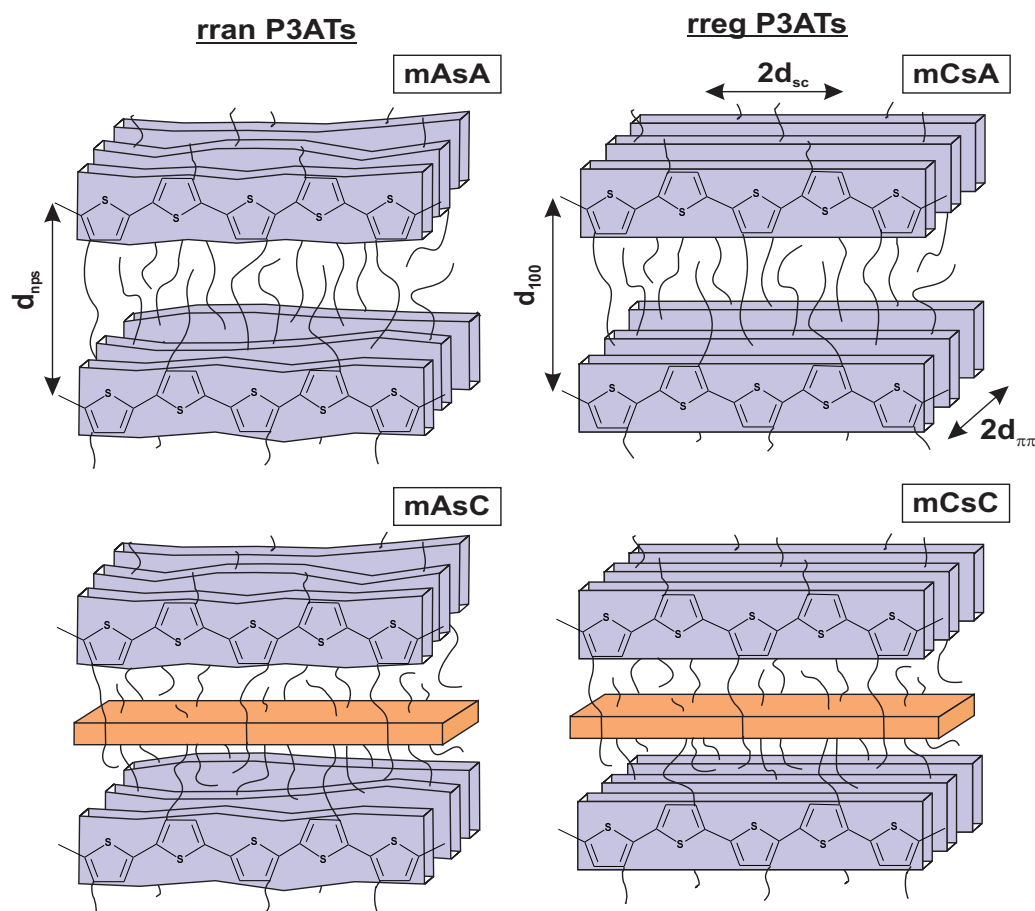
**Figure 9.8:** Classification scheme for nanophase-separated side chain polymers with main (**m**) and side (**s**) chains which can appear in the amorphous (**A**) or the crystalline (**C**) state.

long as $V_{CH2}$ and packing of thiophene rings are unaffected. Nevertheless, the competition of main and side chain packing may weakly influence $d_{\pi\pi}$ and conductivity.

Summarizing the main points of this chapter, one can conclude that only long side chains ($C \geq 10$) in regio-random as well as regio-regular P3ATs can crystallize within self assembled alkyl nanodomains. Shorter side chains ($C < 10$) remain fully disordered. This corresponds to the behavior of many other side chain polymers containing alkyl groups. A peculiar finding for P3ATs is that the methylene units can crystallize in different polymorphic forms like in alkanes. A competition of main and side chain crystallization seemingly appears in regio-regular P3DDT (C=12). A classification scheme is proposed (Figure 9.8) which should be applicable to all kinds of nanophase separated side chain polymers and allow to predict main features of their structure and dynamics depending strongly on the state (crystalline or disordered) of main and side chain domains.

# 9.4 Long term behavior of poly(3-alkyl thiophenes)

So far the discussion has been focused on relaxation dynamics (section 9.2) and structure (section 9.1 and 9.3) of nanophase separated P3ATs without taking seriously into account non-equilibrium effects. However, there are atleast two driving forces which can cause equilibration processes in such systems: (i) side chain crystallization which appears over logarithmic time scales in P3ATs with long alkyl groups (chapter 7). This tendency is only hindered by immobile side chains which are either glassy or highly viscous in regio-random P3ATs and highly crystalline in regio-regular P3ATs at temperatures where side chains can crystallize. In regio-regular systems, frustration may appear due to lattice mismatch of native lattices of main and side chains. Hence, the crystallization tendency of the methylene sequences can drive long term changes below the equilibrium melting temperatures of the side chains. (ii) Physical aging-like densification processes over long times should appear below $T_g$ even if one assumes that crystallization of alkyl groups is completely prevented in P3ATs with $C < 10$ due to their microstructure like in many other non-crystallizable polymers. Note, that densification effects in nanophase separated side chain polymers will occur under special conditions since alkyl nanodomains are surrounded by rigid main chains. Hence, densification in alkyl nanodomains should be accompanied by a redistribution of free volume. It seems to be interesting to understand how the described densification processes on long time scales change the relaxation processes and other properties of P3ATs.

*Changes due to side chain crystallization.* The results of isothermal shear experiments on regio-random and regio-regular P3DDT show clearly that the crystallization of long alkyl groups drives changes in the relaxation dynamics on logarithmic time scales (section 8.1). Three main effects have been observed: (1) The relaxation strength of the $\alpha_{PE}$ process decreases. (2) The conventional $\alpha$ relaxation shifts significantly to lower frequencies and broadens. (3) A significant increase of the storage modulus $G'$ in the rubber plateau region appears. All these findings are compatible with the idea that side chain crystallization starts in already existing alkyl nanodomains. The first effect (1) is easily understandable since methylene units in the crystalline state can not contribute to the $\alpha_{PE}$ process. The other effects (2,3) might be an indirect consequence of side chain crystallization. The existence of a crystalline layer in the alkyl nanodomains can cause significant constraints for the cooperative motions incorporating non-crystalline thiophene rings reflected by the conventional $\alpha$ relaxation. It seems to be natural to assume that the dynamics of thiophene rings slows down if the attached alkyl groups are incorporated in a crystalline layer. This explains the increasing average $\alpha$ relaxation time during side chain crystallization. Similar effects have

been observed for the $\alpha$ relaxation in poly(n-octadecyl methacrylate) [49] and other semi-crystalline polymers where amorphous material is constrained between folded crystalline lamellae. [187] The pronounced broadening of the $\alpha$ relaxation peak may also indicate a spatially heterogeneous distribution of the crystalline material, e.g. crystalline layers with different thickness due to different HT sequences of the attached main chains. The changes in the plateau modulus (3) are understandable as the crystalline alkyl layers should act like physical cross-links connecting different chains in semi-crystalline P3ATs. The effect on the storage modulus is expectedly quite pronounced since the average distance between the crystalline layers is of the order of $d_{nps}$ and significantly smaller than typical average distances between crosslinks in elastomers. Additional effects may occur since the crystalline alkyl layers will also cause reinforcement effects like nanosized filler particles in composites. The combination of both nanoscale effects should be the reason for the great sensitivity of the plateau modulus to side chain crystallization.

*Changes due to physical aging-like processes.* Main trends observed in the dynamic shear modulus $G^*$ during annealing of regio-random P3OT slightly below $T_g$ are similar to those observed during isothermal crystallization of P3DDT although the effects are less pronounced (section 8.1). It is hard to decide whether side chain crystallization appears in P3OT to a very small extent slightly below $T_g$ or physical aging leads to something like a rigid amorphous mesophase in the alkyl nanodomains. Speculatively, more densely packed regions in the alkyl nanodomains produced below $T_g$ influence the relaxation dynamics of the methylene units without being crystalline. Clear indications for a melting peak are not seen in DSC scans performed after long-term annealing experiments. However, an extremely small fraction of crystalline material having a melting point slightly above $T_g$ is hard to exclude since it might be hidden by a strong structural relaxation peak. Regio-regular P3OT show conventional physical aging behavior at $-23°C$ which is below the conventional $T_g$ of the sample (Figure 8.12). Systematic shift of the high frequency wing of the $\alpha$ process to lower frequencies indicates conventional densification behavior in that regions of the semi-crystalline regio-regular P3OT sample where the thiophene rings are amorphous. The decrease in the $\alpha_{PE}$ intensity due to physical aging is very small showing that the density of the alkyl nanodomains changes only slightly in regio-regular P3OT during isothermal annealing slightly below $T_g$.

Generalizing the observations, one can conclude that significant long-term changes occur in the relaxation behavior of regio-random and regio-regular P3ATs. These changes are accompanied by changes in the mechanical and calorimetric properties at room temperature.

Common reason for these effects is a strong tendency of the alkyl groups to densify. Whether or not this densification leads to side chain crystallization depends on side chain length. For long alkyl groups (C=12), side chain crystallization occurs and the $\alpha_{PE}$ process is significantly influenced; while for short side chains (C<10), clear evidence for side chain crystallization is absent and the $\alpha_{PE}$ process is only weakly affected. Time dependent changes regarding the $\alpha$ relaxation are quite similar to those found during physical aging in homogeneous glasses. The results of this work show clearly that detailed knowledge about long-term effects driven by the densification tendency of the alkyl groups is very important for the application of P3ATs as organic semiconductors. The performance of devices designed based on such materials will be influenced if the side chains change their packing state at application relevant temperatures over long times. In the future, it would be interesting to study and understand peculiarities in physical aging behavior of nanostructured polymers where densification appears under special constraints more extensively.

# Chapter 10

# Conclusions and Outlook

In this work, two series of regio-random and regio-regular poly(3-alkyl thiophenes) [P3ATs] with varying side chain lengths from C=4 to 12 carbon atoms per side chain are studied with dynamic shear methods, differential scanning calorimetry and x-ray scattering in order to understand confined dynamics, side chain crystallization and long term behavior of this class of conjugated polymers.

Nanophase separation, i.e. a demixing of main and side chains to form nanodomains of the size 10-30Å is shown for both investigated P3AT series. This is indicated by broad pre-peaks in scattering data in the intermediate $q$ range in regio-random P3ATs and (100) reflections for regio-regular P3ATs as well as by an independent $\alpha_{PE}$ relaxation corresponding to co-operative motions of $CH_2$ units within the alkyl nanodomains. The frequency-temperature position of this $\alpha_{PE}$ relaxation process is depending on side chain lengths and quite similar to that observed for other side chain polymers with comb-like architecture such as poly(n-alkyl methacrylates) and poly(n-alkyl acrylates). A new and surprising finding of this work is that the $\alpha_{PE}$ process in the alkyl nanodomains is independent on the packing of the thiophene main chains, i.e., nearly identical for $CH_2$ units surrounded by glassy and crystalline thiophene rings for regio-random and regio-regular P3ATs respectively. These results strongly support the view that nanophase separation is a general phenomenon for side chain polymers containing long alkyl groups.

Main target of this work was to study the confined dynamics of $CH_2$ units in alkyl nanodomains with dimensions in the range 10-30Å. A systematic shift of the $\alpha_{PE}$ process to higher temperatures and a transition from Arrhenius to non-Arrhenius like behavior with increasing side chain lengths are observed. The physical reason responsible for these trends are discussed. It is shown based on the crystallographic information for regio-regular P3ATs

that the volume per $CH_2$ unit $V_{CH2}$ is quite similar for different side chain lengths. Hence, it is unlikely that density changes are responsible for changes in the $\alpha_{PE}$ dynamics with side chain length. These changes in the dynamics are obviously to a major extent due to geometrical confinement effects. According to the hindered glass transition picture, the cooperative dynamics $\alpha_{PE}$ will change as soon as the alkyl nanodomain size ($d_{nps}$ or $d_{100}$) approaches the size of cooperatively rearranging regions ($\xi_\alpha$). From that perspective, the experimental observations of this work support the existence of cooperatively rearranging regions (CRRs) in glass forming materials having typical dimensions of about $\xi_\alpha$ =10-30Å at the thermal glass transition. This finding is in qualitative agreement with values for the CRR size obtained from studies on glass forming liquids in nanoporous host systems and is compatible with the softening behavior of many complex polymeric systems where an interference of structural and dynamic heterogeneities is relevant.

The results of this work clearly indicate that the alkyl side chains are amorphous for regio-random and regio-regular P3ATs with high molecular weight and C < 10 alkyl carbons per side chain in accordance with findings for other polymer series with similar architecture. This is confirmed by the absence of a melting peak in DSC, comparable intensity of the $\alpha_{PE}$ process in shear data for regio-regular and regio-random samples and constant values for the volume per $CH_2$ in the alkyl nanodomains $V_{CH2}$ which are close to that reported for amorphous polyethylene. Small fractions of crystalline methylene units in the alkyl nanodomains are only observed for regio-random poly(3-decyl thiophene) and poly(3-dodecyl thiophene) as well as regio-regular poly(3-dodecyl thiophene) ($C = 10, 12$). Interestingly, three distinct melting peaks between $-5$ and $50°$C appear for regio-random poly(3-decyl thiophene) and poly(3-dodecyl thiophene) depending on the crystallization conditions. This indicates the occurrence of different polymorphs in the semi-crystalline alkyl nanodomains being a unique finding for comb-like polymers with relatively short crystallizable alkyl side chains. For regio-regular P3DDT, an interrelation between main and side chain crystallization is indicated. The existence of three polymorphs which differ regarding their side chain packing is supported by changes in the average interlayer distance $d_{nps}$. A competition of different packing mechanisms could be also important for understanding polymorphism in such nanophase separated systems.

Detailed shear measurements before and after as well as during isothermal annealing at suitable temperatures for long times show that the $\alpha_{PE}$ process is strongly influenced by side chain crystallization in regio-random and regio-regular poly(3-dodecyl thiophene). The intensity of the $\alpha_{PE}$ process reduces significantly. This effect is accompanied by a significant

increase of the plateau modulus and slowing down the conventional $\alpha$ relaxation incorporating the thiophene rings. These findings are consistent with the assumption that side chain crystallization in P3ATs starts in already existing alkyl nanodomains and appears far away from immobile main chains. Similar effects appear to a minor extent for regio-random P3OT during annealing below $T_g$. In this seemingly amorphous sample, densification is expected driven by physical aging-like equilibration processes below $T_g$. However, it is hard to rule out a tiny fraction of crystalline $CH_2$ units. In regio-regular poly(3-octyl thiophene), side chains are too short to compensate for the hindrance due to crystalline main chains. Hence, no significant changes are observed for the $\alpha_{PE}$ during isothermal annealing over long times and the state of the methylene units within the alkyl nanodomains remains basically unchanged. General conclusion of this part of the work is that different types of equilibration processes will influence the packing state of the side chains near ambient temperature. Over long time scales, side chain crystallization as well as physical aging-like densification processes can be relevant. The influence of long term annealing on the $\alpha$ relaxation shows that main chain packing is also affected. This has to be considered if P3ATs are studied and used as organic semiconductors.

Based on the results of this thesis, one may isolate three main topics which seem to be suitable directions for deeper investigations in the future.

(i) The observation that cooperative $\alpha_{PE}$ process within the alkyl nanodomains depends strongly on their size seems to be important for understanding of the dynamics of complex polymeric systems and can contribute to the ongoing discussion about the nature of the glass transition phenomenon. [1, 3, 75, 188] This result strongly indicates that dynamic heterogeneities connected with CRRs exist and that they have typical dimensions in the range $\xi_\alpha = $ 10-30Å at $T_g$. Much larger CRR sizes seem to be unlikely considering the presented results and what is known about the softening behavior of nanostructured and nanoheterogeneous polymeric bulk systems in general. We think that detailed knowledge about the CRR size is important to predict the softening behavior of multicomponent systems containing different comonomers. Two distinguishable glass transitions will only appear in nanostructured systems with domain sizes larger than $\xi_\alpha$ and narrow interfaces like in microphase separated block copolymers. One single, conventional glass transition appears only if concentration profiles are averaged out within the CRR volume $V_\alpha = \xi_\alpha^3$ as commonly observed for multicomponent systems which are homogeneously mixed on the nanoscale like random copolymers. Broad smeared out glass transitions appear for nanoheterogeneous systems where broad interfacial regions exist causing concentration gradients on scales significantly larger

than $\xi_\alpha$. Consequence is that the CRRs have different chemical compositions resulting in multiple $T_g$s and a smeared out softening process as observed for gradient copolymers. [189] This concept shows that the knowledge about the chemical composition of volumes of few cubic nanometers is important in order to understand peculiarities in the softening behavior of complex polymeric systems like miscible polymer blends showing two separated glass transitions [190] or protiens. [191]

(ii) The finding that side chain crystallization appears in alkyl nanodomains as small as 15-30Å quasi independent on the packing state of the thiophene main chains can be putted in a more general context. This may help to study early stages of crystallization where nanosized crystals also appear. Of special interest in this context is the recent finding that metastable polymorphic states can be stabilized by confining crystallizable materials in nanopores. [192] The situation in case of side chains within the alkyl nanodomains as studied in this work might be in agreement with this finding. Structural models presented by Strobl G. [123, 124], predict a similar situation at the growth front of polyethylene crystals. According to recent versions of this picture, a metastable mesophase appears at the growth front since the polyethylene crystal is thin in this region. Advanced studies on nanophase separated side chain polymers where crystal thickening is avoided due to confinement could help to understand the thermodynamics of the mesophase and the situation at the growth front which is hard to study since it is transient in bulk systems. [129]

(iii) The findings regarding the long term behavior of P3ATs are interesting for their application as well as from the view point of basic research. P3ATs are conjugated polymers which are widely used as organic conductors and as optoelectronic materials. An important aspect which is discussed in the recent literature for conjugated polymers is the influence of side chain packing on the main chain packing. Of particular interest are changes in the $\pi - \pi$ stacking resulting in changes of conductivity and other application relevant properties. [150, 157, 160, 193–195] The fact that the side chains are highly disordered must be always considered if new structural models for P3ATs are developed. Long term effects should be taken into account if materials are optimized for special applications. The systematic selection of suitable polymorphs in the processing step and possible transformations during usage might be important aspects that should be considered if conducting polymers with favorable properties have to be engineered.

# Bibliography

[1] Debenedetti, P. G. and Stillinger, F. H. *Nature* **410**(6825), 259–267 (2001).

[2] Angell, C. A., Poole, P. H., and Shao, J. *Nuovo Cimento Della Societa Italiana Di Fisica D-condensed Matter Atomic Molecular and Chemical Physics Fluids Plasmas Biophysics* **16**(8), 993–1025 (1994).

[3] Angell, C. *Science* **267**, 1924–1935 (1995).

[4] Cohen, M. and Turnbull, D. *Journal of Chemical Physics* **31**(5), 1164–1169 (1959).

[5] Turnbull, D. and Cohen, M. *Journal of Chemical Physics* **34**(1), 120–125 (1961).

[6] Gibbs, J. H. and DiMarzio, E. A. *Journal of Chemical Physics* **28**(3), 373–383 (1958).

[7] Adam, G. and Gibbs, J. H. *Journal of Chemical Physics* **43**(1), 139–146 (1965).

[8] Götze, W. and Sjögren, L. *Reports On Progress In Physics* **55**(3), 241–376 (1992).

[9] Ngai, K. L. and Tsang, K. Y. *Physical Review E* **60**(4), 4511–4517 (1999).

[10] Anderson, P. W. *Science* **267**(5204), 1609–1618 (1995).

[11] Lok, C. *Nature* **467**(7311), 18–21 (2010).

[12] Ramsden, J. *Applied Nanotechnology*. Elsevier Sci Ltd, (2010).

[13] McKenna, G. *European Physical Journal-Special Topics* **141**, 291–301 (2007).

[14] Jackson, C. L. and McKenna, G. B. *Journal of Non-crystalline Solids* **131**, 221–224 (1991).

[15] Pissis, P., Kyritsis, A., Daoukaki, D., Barut, G., Pelster, R., and Nimtz, G. *Journal of Physics-condensed Matter* **10**(28), 6205–6227 (1998).

[16] Rittig, F., Huwe, A., Fleischer, G., Karger, J., and Kremer, F. *Physical Chemistry Chemical Physics* **1**(4), 519–523 (1999).

[17] Alba-Simionesco, C., Dosseh, G., Dumont, E., Frick, B., Geil, B., Morineau, D., Teboul, V., and Xia, Y. *European Physical Journal E* **12**(1), 19–28 (2003).

[18] Beiner, M. and Huth, H. *Nature Materials* **2**(9), 595–599 (2003).

[19] Arbe, A., Genix, A. C., Colmenero, J., Richter, D., and Fouquet, P. *Soft Matter* **4**(9), 1792–1795 (2008).

[20] Donth, E. *Glasübergang*. Akademie-Verlag, (1980).

[21] Forrest, J. A. and Dalnoki-Veress, K. *Advances In Colloid and Interface Science* **94**(1-3), 167–196 (2001).

[22] Ellison, C. J. and Torkelson, J. M. *Nature Materials* **2**(10), 695–700 (2003).

[23] Keddie, J. L., Jones, R. A. L., and Cory, R. A. *Europhysics Letters* **27**(1), 59–64 (1994).

[24] Hamley, I. *The physics of block copolymers*. Oxford Science Publications, (1998).

[25] Beiner, M., Schröter, K., Hempel, E., Reissig, S., and Donth, E. *Macromolecules* **32**(19), 6278–6282 (1999).

[26] Muthukumar, M., Ober, C. K., and Thomas, E. L. *Science* **277**(5330), 1225–1232 (1997).

[27] Ikkala, O. and ten Brinke, G. *Science* **295**(5564), 2407–2409 (2002).

[28] Plate, N. and Shibaev, V. *Journal of Polymer Science: Macromolecular Reviews D* **8**, 117–253 (1974).

[29] Cowie, J. M. G., Haq, Z., McEwen, I. J., and Velickovic, J. *Polymer* **22**(3), 327–332 (1981).

[30] Ringsdorf, H., Tschirner, P., Hermann-Schönherr, O., and Wendorff, J. *Makromolekulare Chemie-Macromolecular Chemistry and Physics* **188**(6), 1431–1445 (1987).

[31] Clauss, J., Schmidt-Rohr, K., Adam, A., Boeffel, C., and Spiess, H. *Macromolecules* **25**(20), 5208–5214 (1992).

[32] Chen, W. and Wunderlich, B. *Macromolecular Chemistry and Physics* **200**(2), 283–311 (1999).

[33] Arrighi, V., Triolo, A., McEwen, I., Holmes, P., Triolo, R., and Amenitsch, H. *Macromolecules* **33**(14), 4989–4991 (2000).

[34] McCullough, R. *Advanced Materials* **10**(2), 93–116 (1998).

[35] Yazawa, K., Inoue, Y., Yamamoto, T., and Asakawa, N. *Physical Review B* **74**(9), 0942041–12 (2006).

[36] Prosa, T. J., Winokur, M. J., and McCullough, R. D. *Macromolecules* **29**(10), 3654–3656 (1996).

[37] Heeger, A. J. *Journal of Physical Chemistry B* **105**(36), 8475–8491 (2001).

[38] Winokur, M. In *Handbook of Conducting Polymers,* Skotheim, T., Elsenbaumer, R., and Reynolds, J., editors, volume 2, 707–726. Marcel Dekker, New York (1998).

[39] Yamamoto, T., Komarudin, D., Arai, M., Lee, B., Suganuma, H., Asakawa, N., Inoue, Y., Kubota, K., Sasaki, S., Fukuda, T., and Matsuda, H. *Journal of the American Chemical Society* **120**(9), 2047–2058 (1998).

[40] Schopf, G. and Kossmehl, G. *Advances in Polymer Science* **129**, 3–145 (1997).

[41] Reddinger, J. L. and Reynolds, J. R. *Advances in polymer science* **145**, 57–122 (1999).

[42] Inganas, O., Salaneck, W. R., Osterholm, J. E., and Laakso, J. *Synthetic Metals* **22**(4), 395–406 (1988).

[43] Rughooputh, S. D. D. V., Hotta, S., Heeger, A. J., and Wudl, F. *Journal of Polymer Science Part B-polymer Physics* **25**(5), 1071–1078 (1987).

[44] Bao, Z., Dodabalapur, A., and Lovinger, A. *Applied Physics Letters* **69**(26), 4108–4110 (1996).

[45] Sirringhaus, H., Brown, P., Friend, R., Nielsen, M., Bechgaard, K., Langeveld-Voss, B., Spiering, A., Janssen, R., Meijer, E., Herwig, P., and de Leeuw, D. *Nature* **401**(6754), 685–688 (1999).

[46] Curtis, M. D., Nanos, J. I., Moon, H., and Jahng, W. S. *Journal of the American Chemical Society* **129**(48), 15072–15084 December (2007).

[47] Prosa, T. J., Moulton, J., Heeger, A. J., and Winokur, M. J. *Macromolecules* **32**(12), 4000–4009 (1999).

[48] Jordan, E. F., Feldeise, D. W., and Wrigley, A. N. *Journal of Polymer Science Part A1* **9**(7), 1835–1851 (1971).

[49] Hempel, E., Huth, H., and Beiner, M. *Thermochimica Acta* **403**(1), 105–114 (2003).

[50] Mierzwa, M., Floudas, G., Stepanek, P., and Wegner, G. *Physical Review B* **62**(21), 14012–14019 (2000).

[51] Hempel, E., Budde, H., Höring, S., and Beiner, M. *Lecture Notes In Physics* **714**, 201–228 (2007).

[52] Shi, H. F., Zhao, Y., Zhang, X. Q., Jiang, S. C., Wang, D. J., Han, C. C., and Xu, D. F. *Macromolecules* **37**(26), 9933–9940 (2004).

[53] Hempel, E., Budde, H., Höring, S., and Beiner, M. *Journal of Non-Crystalline Solids* **352**(42-49, Sp. Iss. SI), 5013–5020 (2006).

[54] Mark, J., Ngai, K., Graessley, W., Mandelkern, L., Samulski, E., Koenig, J., and Wignall, G. *Physical properties of polymers*. Cambridge university press, UK, 3 edition, (2004).

[55] Ferry, J. D. *Viscoelastic Properties of Polymers*. John Wiley and sons, USA, 3 edition, (1980).

[56] Goldstein, M. In *Relaxations in complex systems,* Ngai, K. L. and Wright, G. B., editors, 13–15. National Technical Information Service; U.S. Department of Commerce, (1984). Workshop on Relaxations in disordered systems , Blacksburg, Virginia, 1983.

[57] Ediger, M. D. *Annual Review of Physical Chemistry* **51**, 99–128 (2000).

[58] Angell, C. A., Ngai, K. L., McKenna, G. B., McMillan, P. F., and Martin, S. W. *Journal of Applied Physics* **88**(6), 3113–3157 (2000).

[59] Struik, L. *Physical aging in amorphous polymers and other materials*. Elsevier Sci Ltd, (1978).

[60] Kauzmann, W. *Chemical Reviews* **43**(2), 219–256 (1948).

[61] Mathot, V. *Calorimetry and thermal analysis of polymers*. Carl Hanser Verlag, Munich, (1994).

[62] Johari, G. In *Relaxations in complex systems,* Ngai, K. L. and Wright, G. B., editors, 17–41. National Technical Information Service; U.S. Department of Commerce, (1984). Workshop on Relaxations in disordered systems , Blacksburg, Virginia, 1983.

[63] Nyquist, H. *Physical Review* **32**, 110–113 (1928).

[64] Callen, H. and Greene, R. *Physical Review* **86**(5), 702–710 (1952).

[65] Donth, E. *The Glass Transition: relaxation dynamics in liquids and disordered materials*. Springer, Berlin, (2001).

[66] Richert, R. *Journal of Physical Chemistry B* **101**(33), 6323–6326 (1997).

[67] Richert, R. *Journal of Non-crystalline Solids* **235**, 41–47 (1998).

[68] Johari, G. and Goldstein, M. *Journal of Chemical Physics* **53**(6), 2372–2388 (1970).

[69] Doolittle, A. K. *Journal of Applied Physics* **22**(8), 1031–1035 (1951).

[70] Doolittle, A. K. and Doolittle, D. B. *Journal of Applied Physics* **28**(8), 901–905 (1957).

[71] Donth, E. *Journal of Non-Crystalline Solids* **53**, 325–330 (1982).

[72] Hempel, E., Hempel, G., Hensel, A., Schick, C., and Donth, E. *Journal of Physical Chemistry B* **104**(11), 2460–2466 (2000).

[73] Beiner, M., Kahle, S., Hempel, E., Schroter, K., and Donth, E. *Macromolecules* **31**(25), 8973–8980 (1998).

[74] Kahle, S., Korus, J., Hempel, E., Unger, R., Horing, S., Schroter, K., and Donth, E. *Macromolecules* **30**(23), 7214–7223 (1997).

[75] Huth, H., Beiner, M., and Donth, E. *Physical Review B* **61**(22), 15092–15101 (2000).

[76] Matsuoka, S. *Relaxation phenomenon in polymers*. Hanser, Munich, (1992).

[77] Yamamuro, O., Tsukushi, I., Lindqvist, A., Takahara, S., Ishikawa, M., and Matsuo, T. *Journal of Physical Chemistry B* **102**(9), 1605–1609 (1998).

[78] Moynihan, C. T. and Schroeder, J. *Journal of Non-crystalline Solids* **160**(1-2), 52–59 (1993).

[79] Sillescu, H. *Acta Polymerica* **45**(1), 2–2 (1994).

[80] Donth, E., Hempel, E., and Schick, C. *Journal of Physics-condensed Matter* **12**(16), L281–L286 (2000).

[81] Alcoutlabi, M. and McKenna, G. B. *Journal of Physics-condensed Matter* **17**(15), R461–R524 April (2005).

[82] Alba-Simionesco, C., Coasne, B., Dosseh, G., Dudziak, G., Gubbins, K. E., Radhakrishnan, R., and Sliwinska-Bartkowiak, M. *Journal of Physics-condensed Matter* **18**(6), R15–R68 (2006).

[83] Zheng, W. and Simon, S. L. *Journal of Chemical Physics* **127**(19), 1945011–11 (2007).

[84] Arndt, M., Stannarius, R., Groothues, H., Hempel, E., and Kremer, F. *Physical Review Letters* **79**(11), 2077–2080 (1997).

[85] Zorn, R., Hartmann, L., Frick, B., Richter, D., and Kremer, F. *Journal of Non-crystalline Solids* **307**, 547–554 (2002).

[86] Schönhals, A., Goering, H., Schick, C., Frick, B., and Zorn, R. *Colloid and Polymer Science* **282**(8), 882–891 (2004).

[87] Schönhals, A., Goering, H., Schick, C., Frick, B., and Zorn, R. *Journal of Non-crystalline Solids* **351**(33-36), 2668–2677 (2005).

[88] Li, Q. X. and Simon, S. L. *Macromolecules* **42**(10), 3573–3579 (2009).

[89] Schönhals, A., Goering, H., and Schick, C. *Journal of Non-crystalline Solids* **305**(1-3), 140–149 (2002).

[90] Kremer, F., Huwe, A., Arndt, M., Behrens, P., and Schwieger, W. *Journal of Physics-condensed Matter* **11**(10A), A175–A188 (1999).

[91] Forrest, J. A., DalnokiVeress, K., Stevens, J. R., and Dutcher, J. R. *Physical Review Letters* **77**(19), 4108–4108 (1996).

[92] Forrest, J. A., Dalnoki-Veress, K., and Dutcher, J. R. *Physical Review E* **58**(5), 6109–6114 (1998).

[93] Serghei, A., Huth, H., Schick, C., and Kremer, F. *Macromolecules* **41**(10), 3636–3639 (2008).

[94] Erber, M., Tress, M., Mapesa, E. U., Serghei, A., Eichhorn, K. J., Voit, B., and Kremer, F. *Macromolecules* **43**(18), 7729–7733 (2010).

[95] Serghei, A. *Macromolecular Chemistry and Physics* **209**(14), 1415–1423 (2008).

[96] Fukao, K., Uno, S., Miyamoto, Y., Hoshino, A., and Miyaji, H. *Physical Review E* **64**(5), 051807 (2001).

[97] Mapesa, E. U., Erber, M., Tress, M., Eichhorn, K. J., Serghei, A., Voit, B., and Kremer, F. *European Physical Journal-special Topics* **189**(1), 173–180 (2010).

[98] Serghei, A., Tress, M., and Kremer, F. *Journal of Chemical Physics* **131**(15), 1549041–10 (2009).

[99] McCoy, J. D. and Curro, J. G. *Journal of Chemical Physics* **116**(21), 9154–9157 (2002).

[100] Morineau, D., Xia, Y. D., and Alba-Simionesco, C. *Journal of Chemical Physics* **117**(19), 8966–8972 (2002).

[101] Patkowski, A., Ruths, T., and Fischer, E. W. *Physical Review E* **67**(2), 0215011–8 (2003).

[102] Daoukaki, D., Barut, G., Pelster, R., Nimtz, G., Kyritsis, A., and Pissis, P. *Physical Review B* **58**(9), 5336–5345 (1998).

[103] Pissis, P., Kyritsis, A., Barut, G., Pelster, R., and Nimtz, G. *Journal of Non-crystalline Solids* **235**, 444–449 (1998).

[104] Schonhals, A., Goering, H., Schick, C., Frick, B., and Zorn, R. *European Physical Journal E* **12**(1), 173–178 (2003).

[105] Melnichenko, Y. B., Schuller, J., Richert, R., Ewen, B., and Loong, C. K. *Journal of Chemical Physics* **103**(6), 2016–2024 (1995).

[106] Richert, R. and Yang, M. *Journal of Physical Chemistry B* **107**(4), 895–898 (2003).

[107] Ellison, C. J., Mundra, M. K., and Torkelson, J. M. *Macromolecules* **38**(5), 1767–1778 (2005).

[108] Arbe, A., Genix, A.-C., Arrese-Igor, S., Colmenero, J., and Richter, D. *Macromolecules* **43**(6), 3107–3119 (2010).

[109] McCreight, K., Ge, J., Guo, M., Mann, I., Li, F., Shen, Z., Jin, X., Harris, F., and Cheng, S. *Journal of Polymer Science Part B* **37**(14), 1633–1646 (1999).

[110] Hodge, I. M. *Journal of Non-crystalline Solids* **169**(3), 211–266 (1994).

[111] Hutchinson, J. M. *Progress In Polymer Science* **20**(4), 703–760 (1995).

[112] Kovacs, A. J., Stratton, R. A., and Ferry, J. D. *Journal of Physical Chemistry* **67**(1), 152–161 (1963).

[113] Mijovic, J., Nicolais, L., Damore, A., and Kenny, J. M. *Polymer Engineering and Science* **34**(5), 381–389 (1994).

[114] Hodge, I. M. *Science* **267**(5206), 1945–1947 (1995).

[115] Simon, S. L., Plazek, D. J., Sobieski, J. W., and McGregor, E. T. *Journal of Polymer Science Part B-polymer Physics* **35**(6), 929–936 (1997).

[116] Greiner, R. and Schwarzl, F. R. *Rheologica Acta* **23**(4), 378–395 (1984).

[117] Ngai, K. L. and Paluch, M. *Journal of Chemical Physics* **120**(2), 857–873 (2004).

[118] Strobl, G. *The Physics of Polymers*. Springer, Berlin, (1997).

[119] Wunderlich, B. *Thermal Analysis*. Academic Press, Inc., (1990).

[120] Wunderlich, B. *Macromolecular Physics*. Academic Press, Inc., (1976).

[121] Lauritzen, J. I. and Hoffman, J. D. *Journal of Research of the National Bureau of Standards Section A-Physics and Chemistry* **64**(1), 73–102 (1960).

[122] Hoffman, J. D., Miller, R. L., Marand, H., and Roitman, D. B. *Macromolecules* **25**(8), 2221–2229 (1992).

[123] Strobl, G. *European Physical Journal E* **3**(2), 165–183 (2000).

[124] Strobl, G. *European Physical Journal E* **18**(3), 295–309 (2005).

[125] Sirota, E. B. *Macromolecules* **40**(4), 1043–1048 (2007).

[126] Rastogi, S., Hikosaka, M., Kawabata, H., and Keller, A. *Macromolecules* **24**(24), 6384–6391 (1991).

[127] Keller, A. and Cheng, S. Z. D. *Polymer* **39**(19), 4461–4487 (1998).

[128] Shi, H. F., Zhao, Y., Jiang, S. C., Xin, J. H., Rottstegge, J., Xu, D. F., and Wang, D. J. *Polymer* **48**(9), 2762–2767 (2007).

[129] Beiner, M. *Journal of Polymer Science Part B* **46**(15), 1556–1561 (2008).

[130] Schawe, J. E. K. *Thermochimica Acta* **261**, 183–194 (1995).

[131] Weyer, S., Hensel, A., and Schick, C. *Thermochimica Acta* **305**, 267–275 (1997).

[132] Menard, K. *Characterization and analysis of polymers*. John Wiley & Sons Inc, (2008).

[133] Ward, I. and Sweeney, J. *An introduction to the mechanical properties of the solid polymers*. John Wiley & Sons Inc, 2 edition, (2004).

[134] Kittel, C. *Introduction to state physics*. John Wiley & Sons Inc, 6 edition, (1986).

[135] Roe, R. *Methods of x-ray and neutron scattering in polymer science*. Oxford University Press, Inc., (2000).

[136] Jenkins, R. and Snyder, R. L. *Introduction to x-ray powder diffractometry*. Wiley-VCH, Inc., 1 edition, (1996).

[137] Kobayashi, M., Chen, J., Chung, T. C., Moraes, F., Heeger, A. J., and Wudl, F. *Synthetic Metals* **9**(1), 77–86 (1984).

[138] Jen, K. Y., Miller, G. G., and Elsenbaumer, R. L. *Journal of the Chemical Society-chemical Communications* (17), 1346–1347 (1986).

[139] Elsenbaumer, R. L., Jen, K. Y., and Oboodi, R. *Synthetic Metals* **15**(2-3), 169–174 (1986).

[140] Leclerc, M., Diaz, F. M., and Wegner, G. *Makromolekulare Chemie-Macromolecular Chemistry and Physics* **190**(12), 3105–3116 (1989).

[141] McCullough, R. D. and Lowe, R. D. *Journal of the Chemical Society-chemical Communications* (1), 70–72 (1992).

[142] Chen, T., Wu, X., and Rieke, R. *Journal of the American Chemical Society* **117**(1), 233–244 (1995).

[143] Liu, J. S., Loewe, R. S., and McCullough, R. D. *Macromolecules* **32**(18), 5777–5785 (1999).

[144] Yue, S., Berry, G. C., and McCullough, R. D. *Macromolecules* **29**(3), 933–939 (1996).

[145] Bruckner, S. and Porzio, W. *Makromolekulare Chemie-macromolecular Chemistry and Physics* **189**(4), 961–967 (1988).

[146] Kawai, T., Nakazono, M., Sugimoto, R., and Yoshino, K. *Journal of the Physical Society of Japan* **61**(9), 3400–3406 (1992).

[147] Prosa, T. J., Winokur, M. J., Moulton, J., Smith, P., and Heeger, A. J. *Macromolecules* **25**(17), 4364–4372 (1992).

[148] Tashiro, K., Ono, K., Minagawa, Y., Kobayashi, M., Kawai, T., and Yoshino, K. *Journal of Polymer Science Part B-polymer Physics* **29**(10), 1223–1233 (1991).

[149] Mena-Osteritz, E., Meyer, A., Langeveld-Voss, B. M. W., Janssen, R. A. J., Meijer, E. W., and Bauerle, P. *Angewandte Chemie-international Edition* **39**(15), 2680–2684 (2000).

[150] Brinkmann, M. and Rannou, P. *Macromolecules* **42**(4), 1125–1130 (2009).

[151] Lan, Y. K. and Huang, C. I. *Journal of Physical Chemistry B* **113**(44), 14555–14564 (2009).

[152] Wu, Z. Y., Petzold, A., Henze, T., Thurn-Albrecht, T., Lohwasser, R. H., Sommer, M., and Thelakkat, M. *Macromolecules* **43**(10), 4646–4653 (2010).

[153] Pascui, O. F., Lohwasser, R., Sommer, M., Thelakkat, M., Thurn-Albrecht, T., and Saalwachter, K. *Macromolecules* **43**(22), 9401–9410 (2010).

[154] Park, K. C. and Levon, K. *Macromolecules* **30**(11), 3175–3183 (1997).

[155] Malik, S. and Nandi, A. K. *Journal of Polymer Science Part B* **40**(18), 2073–2085 (2002).

[156] Prosa, T. J., Winokur, M. J., Moulton, J., Smith, P., and Heeger, A. J. *Physical Review B* **51**(1), 159–168 (1995).

[157] Kline, R. J., DeLongchamp, D. M., Fischer, D. A., Lin, E. K., Richter, L. J., Chabinyc, M. L., Toney, M. F., Heeney, M., and McCulloch, I. *Macromolecules* **40**(22), 7960–7965 (2007).

[158] Meille, S. V., Romita, V., Caronna, T., Lovinger, A. J., Catellani, M., and Belobrzeckaja, L. *Macromolecules* **30**(25), 7898–7905 (1997).

[159] Tashiro, K., Kobayashi, M., Kawai, T., and Yoshino, K. *Polymer* **38**(12), 2867–2879 (1997).

[160] Wu, P. T., Ren, G. Q., and Jenekhe, S. A. *Macromolecules* **43**(7), 3306–3313 (2010).

[161] Heijboer, J. *Physics of Non-Crystalline Solids; Prins, J. A., Ed.; North Holland: Amsterdam* , 231 (1965).

[162] Hempel, E., Beiner, M., Huth, H., and Donth, E. *Thermochimica Acta* **391**(1-2), 219–225 (2002).

[163] Small, D. M. *Journal of Lipid Research* **25**(13), 1490–1500 (1984).

[164] Ngai, K. and Beiner, M. *Macromolecules* **37**(21), 8123–8127 (2004).

[165] Böhmer, R., Ngai, K. L., Angell, C. A., and Plazek, D. J. *Journal of Chemical Physics* **99**(5), 4201–4209 (1993).

[166] Plazek, D. *Polymer Journal* **12**(1), 43–53 (1980).

[167] Beiner, M., Reissig, S., Schröter, K., and Donth, E. *Rheologica Acta* **36**(2), 187–196 (1997).

[168] Höhne, G. *Polymer* **42**, 4689–4698 (2002).

[169] Broadhurst, M. G. *Journal of Research of the National Bureau of Standards Section A-physics and Chemistry* **66**(3), 241–249 (1962).

[170] Zerbi, G., Magni, R., Gussoni, M., Moritz, K. H., Bigotto, A., and Dirlikov, S. *Journal of Chemical Physics* **75**(7), 3175–3194 (1981).

[171] Zheng, W. Y., Levon, K., Laakso, J., and Osterholm, J. E. *Macromolecules* **27**(26), 7754–7768 (1994).

[172] Tashiro, K., Sasaki, S., and Kobayashi, M. *Macromolecules* **29**(23), 7460–7469 (1996).

[173] Hempel, E., Beiner, M., Horing, S., and Donth, E. *Colloid and Polymer Science* **273**(12), 1151–1155 (1995).

[174] Jones, A. T. *Makromolekulare Chemie* **71**, 1–32 (1964).

[175] Nurulla, I., Morikita, T., Fukumoto, H., and Yamamoto, T. *Macromolecular Chemistry and Physics* **202**(11), 2335–2340 (2001).

[176] Wunderlich, B. *Thermochimica Acta* **492**(1-2, Sp. Iss. SI), 2–15 (2009).

[177] Gaborieau, M., Graf, R., and Spiess, H. W. *Macromolecular Chemistry and Physics* **209**(20), 2078–2086 (2008).

[178] Gopalakrishnan, T. R. and Beiner, M. volume 40 of *Journal of Physics: Conference Series*, 67–75, (2006).

[179] Ungar, G., Zeng, X. B., Brooke, G. M., and Mohammed, S. *Macromolecules* **31**(6), 1875–1879 (1998).

[180] Gaur, U. and Wunderlich, B. *Macromolecules* **13**(2), 445–446 (1980).

[181] Ngai, K., Gopalakrishnan, T., and Beiner, M. *Polymer* **47**(20), 7222–7230 (2006).

[182] Sirota, E. and Herhold, A. *Science* **283**(5401), 529–532 (1999).

[183] Herhold, A., King, H., and Sirota, E. *Journal of Chemical Physics* **116**(20), 9036–9050 (2002).

[184] Sommer, J. *Lecture Notes in Physics* **714**, 19–46 (2007).

[185] Nojima, S., Ono, M., and Ashida, T. *Polymer Journal* **24**(11), 1271–1280 (1992).

[186] Prosa, T. J., Winokur, M. J., Moulton, J., Smith, P., and Heeger, A. J. *Macromolecules* **25**(17), 4364–4372 (1992).

[187] Schick, C. and Donth, E. *Physica Scripta* **43**(4), 423–429 (1991).

[188] Berthier, L., Biroli, G., Bouchaud, J., Cipelletti, L., El Masri, D., L'Hote, D., Ladieu, F., and Pierno, M. *Science* **310**(5755), 1797–1800 (2005).

[189] Mok, M. M., Kim, J., and Torkelson, J. M. *Journal of Polymer Science Part B-polymer Physics* **46**(1), 48–58 (2008).

[190] He, Y. Y., Lutz, T. R., Ediger, M. D., Pitsikalis, M., Hadjichristidis, N., and von Meerwall, E. A. *Macromolecules* **38**(14), 6216–6226 (2005).

[191] Beiner, M. *Soft Matter* **3**(4), 391–393 (2007).

[192] Beiner, M., Rengarajan, G. T., Pankaj, S., Enke, D., and Steinhart, M. *Nano Letters* **7**(5), 1381–1385 (2007).

[193] Ahmed, E., Kim, F. S., Xin, H., and Jenekhe, S. A. *Macromolecules* **42**(22), 8615–8618 (2009).

[194] Ong, B. S., Wu, Y. L., Liu, P., and Gardner, S. *Journal of the American Chemical Society* **126**(11), 3378–3379 (2004).

[195] Osaka, I., Zhang, R., Sauve, G., Smilgies, D. M., Kowalewski, T., and McCullough, R. D. *Journal of the American Chemical Society* **131**(7), 2521–2529 (2009).

# Publications and Patent Applications

## Publications

- Pulmagatta, B., **Pankaj, S.**, Beiner, M. and Binder, W. "Hierarchical nanostructures in semi-fluorinated norbornene block copolymer", *Macromolecules*, 2011, in press (DOI: 10.1021/ma102195y).

- **Pankaj, S.** and Beiner, M. "Confined dynamics and crystallization in self assembled alkyl nanodomains", *J. Phys. Chem. B*, vol. **114**, pp. 15459, 2010.

- **Pankaj, S.** and Beiner, M. "Side chain crystallization and non-equilibrium phenomena in nanophase separated poly(3-alkyl thiophenes)", *AIP Conference Proceedings*, vol. **1255**, pp. 107, 2010.

- **Pankaj, S.** and Beiner, M. "Long-term behavior and side chain crystallization of poly(3-alkyl thiophenes)", *Soft Matter*, vol. **6**, pp. 3506, 2010.

- **Pankaj, S.**, Hempel, E. and Beiner, M. "Side-chain dynamics and crystallization in a series of regio-random poly(3-alkylthiophenes), *Macromolecules*, vol. **42**, pp. 716, 2009.

- Beiner, M., Rengarajan, G.T., **Pankaj, S.**, Enke, D. and Steinhart, M. "Manipulating the crystalline ctate of pharmaceuticals by nanoconfinement", *Nanoletters*, vol. **7**, pp. 1381, 2007.

## Patent Applications

- Beiner, M., Rengarajan, G.T., **Pankaj, S.**, and Steinhart, M. "Verfahren zur Herstellung langzeitstabiler amorpher Arzneimittel", *DE 10 2006 044 199 A1*, 2006.

# Acknowledgments

angle x-ray diffraction and analyzing the data without which this thesis would not have been completed.

I was fortunate to have Mr. Yogesh Bhatnagar as my Physics teacher in high school who taught me the basics of physics. I could have never started all these research without his teachings which opened unknown areas to me.

My deepest gratitude to my parents and my wife for their immense emotional support, love, dedication and constant encouragement at every point in my life. I wish to extend my sincere thanks to my parents-in law for believing in me. I am thankful to almighty for blessing me with such a caring and loving family who are my true fortune.

I thank all my friends and colleagues in Halle and worldwide for support, help and encouragements. I also express my apologies that I could not convey my thanks personally to all of them.

Last but not the least, I thank state Sachsen Anhalt for the financial support during this work.

# Curriculum Vitae

| | |
|---|---|
| First Name | Shireesh |
| Family Name | Pankaj |
| Date of Birth | January 20, 1982 (Jaipur, India) |
| Nationality | Indian |
| E-mail | *shireesh.pankaj@physik.uni-halle.de* |

---

### EDUCATION

*Apr. 2007 - present*        Martin-Luther-University Halle Wittenberg (Halle, Germany)
Ph.D. candidate (Supervisor: PD Dr. Mario Beiner)

*Oct. 2004 - Nov. 2006*        Martin-Luther-University Halle Wittenberg (Halle, Germany)
Master of Science (Applied Polymer Science)

*May. 1999 - May. 2003*        North Maharastra university (Jalgaon, India)
Bachelor of Engineering (Mechanical Engineering)

---

### PROFESSIONAL EXPERIENCE

*Jul. 2003 - Oct. 2004*        Remsons Industries Ltd ( Gurgaon, India)
Design Engineer

# Eidesstattliche Erklärung

Ich erkläre hiermit, dass ich keine anderen als die von mir angegebenen Quellen und Hilfsmittel zur Erstellung meiner Dissertation verwendet habe. Den benutzen Werken wörtlich oder inhaltlich entnommene Stellen sind als solche gekennzeichnet.

Shireesh Pankaj

Halle(Saale), Januar 2011